

---

**Theses and Dissertations**

---

Spring 2019

## **URANS V&V for KCS free running course keeping and maneuvering simulations in calm water and regular head/oblique waves**

Dong-Hwan Kim  
*University of Iowa*

Follow this and additional works at: <https://ir.uiowa.edu/etd>



Part of the [Mechanical Engineering Commons](#)

Copyright © 2019 Dong-Hwan Kim

This dissertation is available at Iowa Research Online: <https://ir.uiowa.edu/etd/6780>

---

### **Recommended Citation**

Kim, Dong-Hwan. "URANS V&V for KCS free running course keeping and maneuvering simulations in calm water and regular head/oblique waves." PhD (Doctor of Philosophy) thesis, University of Iowa, 2019.  
<https://doi.org/10.17077/etd.s3n9-tjlo>

---

Follow this and additional works at: <https://ir.uiowa.edu/etd>



Part of the [Mechanical Engineering Commons](#)

URANS V&V FOR KCS FREE RUNNING COURSE KEEPING AND  
MANEUVERING SIMULATIONS IN CALM WATER AND  
REGULAR HEAD/OBLIQUE WAVES

by

Dong-Hwan Kim

A thesis submitted in partial fulfillment  
of the requirements for the Doctor of Philosophy  
degree in Mechanical Engineering in the  
Graduate College of  
The University of Iowa

May 2019

Thesis Supervisors: Professor Frederick Stern  
Associate Research Scientist Yugo Sanada

## ABSTRACT

The capability of CFD is assessed by utilizing CFDShip-Iowa V4.5 for the prediction of the 6DOF motion responses, forces, moments and the local flow field of the 2.7m KCS model in various weather/operating conditions. The discretized propeller is preferred and the rudder is designed to be active up to  $\pm 35$  degrees. Grid triplets are generated with the refinement ratio  $\sqrt{2}$  and verification is achieved for the resistance and propeller open water tests while for the other tests is only partially fulfilled. The verification shows unsmooth convergence, however, the errors from grid triplets are small. The propeller open water test validates the performance of the discretized propeller successfully. The free decay tests could predict reasonable heave/pitch/roll natural frequencies. The resistance test verifies the nominal wake distribution. The self-propulsion test using discretized propeller shows 18% higher propeller inflow and 0.1 thrust deduction factor compared to resistance test. A propeller blade that sweeps the starboard experienced higher thrust inducing non-axisymmetric propeller wake and thus affecting the angle of attack of the rudder. Neutral rudder angle diminishes effective angle of attack and keeps the course straight. Maneuvering simulations could predict qualitatively good agreement for validation variables while the trajectory needs more improvement. Using the discretized propeller for the head/oblique wave course-keeping simulations achieved validation successfully. The RAO of added thrust, torque and propeller rotational speed resembles the RAO of added-resistance except showing larger values during long waves. The mean propeller efficiency is at the minimum when the ship experiences a resonance. The first harmonic amplitude of the propeller efficiency increases followed by the increase of the wavelength.

## PUBLIC ABSTRACT

Due to worldwide interest in energy saving/efficient ship, predicting the propeller efficiency accurately has become more important nowadays. The current study aims to simulate the self-propelled ship in calm water and waves by using a discretized propeller and a rudder as well as the ship hull. The averaged resistance of the ship in wave is always larger than the one from still water when the ship operates at the same speed. Therefore, the hydrodynamic performances of the propeller also must increase to overcome this increased resistance. The ratio of the thrust with respect to the input torque from the engine, which is the propeller efficiency, will change, too, and estimating/evaluating the propeller efficiency in waves accurately is by far becoming of great importance. The current numerical simulation is strictly validated against the experimental data and adds physical explanations by taking advantage of the current numerical tool. From this study, the averaged propeller efficiency is found to be minimized when the frequency of the ship becomes near to the natural frequency of the ship. Also, the propeller efficiency is found to oscillate with respect to the average value and the amount is found non-negligible.

## TABLE OF CONTENTS

LIST OF TABLES.....	vii
LIST OF FIGURES .....	ix
1. INTRODUCTION .....	1
1.1.    Motivation .....	1
1.2.    Background.....	1
1.3.    Objective.....	4
1.4.    Approach .....	5
2. BENCHMARK DATA, CFD TEST MATRIX AND COORDINATE SYSTEM .....	6
2.1.    Hull, Propeller and Rudder Geometry.....	6
2.2.    Available Benchmark Experimental Data and CFD Test Matrix.....	7
2.3.    Coordinate System.....	11
3. COMPUTATIONAL & ANALYSIS METHODS .....	18
3.1.    CFDShip-Iowa V4.5, Modelling and HPC.....	18
3.2.    Grids .....	19
3.3.    Domain size .....	22
3.4.    Boundary Conditions.....	23
3.5.    Numerical Schemes and Case Setup .....	23
4. PROPELLER OPEN WATER TEST.....	32
4.1.    Verification.....	32
4.2.    Validation .....	32
4.3.    Surface Pressure .....	33
4.4.    Vortex Core .....	33
5. HYDROSTATIC SETUP AND DECAY TESTS.....	40
5.1.    Hydrostatic Setup .....	40

5.2.	Free Heave Decay.....	40
5.3.	Free Pitch Decay.....	41
5.4.	Free Roll Decay .....	41
6.	RESISTANCE TEST .....	49
6.1.	Verification.....	49
6.2.	Validation .....	50
6.3.	Longitudinal Distribution of the Resistance.....	51
6.4.	Local Flow.....	52
7.	CALM WATER SELF-PROPULSION TEST .....	58
7.1.	Validation .....	58
7.2.	Propeller-Hull-Rudder Interaction.....	61
	7.2.1. Effect of the Propeller.....	61
	7.2.2. Effect of the Rudder.....	64
7.3.	Neutral Rudder Angle.....	66
7.4.	Local Flow .....	67
8.	CALM WATER MANEUVERING.....	82
8.1.	Turning-circle Test .....	82
8.2.	Zig-zag Test .....	83
9.	COURSE KEEPING IN REGULAR HEAD WAVES .....	95
9.1.	Self-propulsion Test .....	95
	9.1.1. 2DOF Captive Self-propulsion Test .....	95
	9.1.2. 6DOF Free-running Self-propulsion Test.....	96
9.2.	Course Keeping in Regular Head Wave.....	97
	9.2.1. Time-history.....	97
	9.2.2. Validation of the Zeroth Harmonic Amplitude.....	98

9.2.3. Validation of the First Harmonic Amplitude .....	99
9.2.4. Validation of the First Harmonic Phase.....	100
9.2.5. Added Powering Variables .....	101
9.2.6. Self-propulsion Factors.....	101
9.2.7. Relative Motions.....	103
9.2.8. Location of the Added-resistance .....	103
9.2.9. Local Flow .....	104
10. COURSE KEEPING IN REGULAR OBLIQUE WAVES .....	126
10.1. Self-propulsion Test .....	126
10.2. Course-keeping.....	127
10.2.1. Time-history .....	127
10.2.2. Validation of the Zeroth Harmonic Amplitude .....	127
10.2.3. Validation of the First Harmonic Amplitude.....	129
10.2.4. Validation of First Harmonic Phase .....	130
10.2.5. Added Powering Variables.....	131
10.2.6. Self-Propulsion Factors .....	132
10.2.7. Relative Motions.....	132
10.2.8. Location of the Added-resistance .....	133
11. CONCLUSIONS.....	151
12. FUTURE WORKS.....	155
REFERENCES .....	156

## LIST OF TABLES

Table 2-1. Main particular and appendage information.....	13
Table 2-2. CFD test matrix .....	14
Table 3-1. Sizes of grid systems .....	26
Table 3-2. Detail of grid size .....	27
Table 3-3. Detail of boundary conditions .....	28
Table 4-1. Verification results for the POT .....	34
Table 4-2. Validation results for the POT.....	35
Table 5-1. Validation results for the hydrostatic setup.....	45
Table 5-2. Validation results for the heave decay test.....	45
Table 5-3. Validation results for the pitch decay test .....	45
Table 5-4. Validation results for the roll decay test.....	46
Table 6-1. Verification results for the resistance test .....	53
Table 6-2. Validation results for the resistance test.....	53
Table 7-1. Validation results for the SP tests.....	68
Table 7-2. Breakdown of total F&M for the resistance/SP test.....	69
Table 7-3. Breakdown of z-force for the SP test .....	69
Table 7-4. AoAs calculated at different vertical locations .....	70
Table 8-1. Validation on IMO criteria for $\pm 35^\circ$ turning-circle tests.....	85
Table 8-2. Validation on IMO criteria for $\pm 10^\circ/10^\circ$ zig-zag test.....	86
Table 8-3. Validation on IMO criteria for $\pm 20^\circ/20^\circ$ zig-zag tests .....	87
Table 9-1. Validation of propeller rotational speed for the SP tests in head waves .....	105
Table 9-2. Validation of 0th harm. amp. for CK tests in head waves.....	106
Table 9-3. Validation of 1st harm. amp. for CK tests in head waves .....	107
Table 9-4. Validation of 1st harm. phases for CK tests in head waves .....	108

Table 9-5. Validation of added-powering var. for CK tests in head waves.....	109
Table 9-6. Validation of SP factors for CK tests in head waves.....	110
Table 9-7. AoAs for the different z-positions.....	110
Table 10-1. Validation of propeller rotational speed for SP tests in oblique waves.....	134
Table 10-2. Validation of 0th harm. amp. for CK tests in oblique waves .....	135
Table 10-3. Validation of 1st harm. amp. for CK tests in oblique waves.....	136
Table 10-4. Validation of 1st harm. phases for CK tests in oblique waves.....	137
Table 10-5. Validation of added-powering var. for CK tests in oblique waves .....	138
Table 10-6. Validation of SP factors for CK tests in oblique waves .....	139

## LIST OF FIGURES

Figure 2-1. KCS hull appended with the propeller and the rudder .....	15
Figure 2-2. Coordinate system.....	16
Figure 2-3. Natural/encounter frequencies and points of interest.....	17
Figure 3-1. Domain sizes .....	29
Figure 3-2. Surface grids of the bare-hull.....	30
Figure 3-3. Surface grids of KP505 and rudder.....	31
Figure 4-1. Time-histories from POT simulations.....	36
Figure 4-2. Validation results for the POT .....	37
Figure 4-3. Dynamic pressure distributions on the propeller suction/pressure sides .....	38
Figure 4-4. Dynamic pressure distributions and $Q = 300$ .....	39
Figure 5-1. Time-histories from the heave decay tests.....	47
Figure 5-2. Time-history from the pitch decay test .....	47
Figure 5-3. Time histories from the roll decay test.....	48
Figure 5-4. Roll extinction curve .....	48
Figure 6-1. Time-histories from the resistance test .....	54
Figure 6-2. Longitudinal distribution of the hydrodynamic x-force on the hull.....	55
Figure 6-3. Distribution of the hydrodynamic pressure near the stern region .....	55
Figure 6-4. x-vel. contours and y,z-vel. vectors at vertical sections (G1) .....	56
Figure 6-5. x-vel. contours and y,z-vel. vectors at vertical sections (G2) .....	56
Figure 6-6. x-vel. contours and y,z-vel. vectors at V&H sections (G3) .....	57
Figure 7-1. Time-histories from the SP test.....	71
Figure 7-2. Long. distribution of mean hydrodynamic F&M .....	72
Figure 7-3. Dist. of mean hydrodynamic pressure near the stern .....	73
Figure 7-4. Dist. of SD of hydrodynamic pressure near the stern .....	73

Figure 7-5. Wake-contour/streamlines on V&H sections for the SP test .....	74
Figure 7-6. Time-histories of forces of a single blade and a propeller from the SP test .....	75
Figure 7-7. Wake-contour/streamlines on V&H sections for the SP test (w/o rudder) .....	76
Figure 7-8. Wake-contour/streamlines on V&H sections: Perturbation.....	77
Figure 7-9. Dynamic pressure distribution on the rudder .....	78
Figure 7-10. Dynamic pressure distribution on the rudder: Perturbation .....	78
Figure 7-11. AoA on the rudder vs. vertical locations.....	79
Figure 7-12. Local flow validation at V5.....	80
Figure 7-13. Pressure on hull and blades and $Q = 1000$ at wake for SP test .....	81
Figure 8-1. Time-histories from the $+35^\circ$ turning-circle test.....	88
Figure 8-2. Time-histories from the $-35^\circ$ turning-circle test .....	89
Figure 8-3. Time-histories from the $+10^\circ/10^\circ$ zig-zag test.....	90
Figure 8-4. Time-histories from the $-10^\circ/10^\circ$ zig-zag test.....	91
Figure 8-5. Time-histories from the $+20^\circ/20^\circ$ zig-zag test.....	92
Figure 8-6. Time-histories from the $-20^\circ/20^\circ$ zig-zag test.....	93
Figure 8-7. Effective wake field from the $+35^\circ$ turning test.....	94
Figure 9-1. Validation results for SP tests in head waves.....	111
Figure 9-2. Time-histories from the CK test in head wave ( $\lambda/L=0.65$ ).....	112
Figure 9-3. Time-histories from the CK test in head wave ( $\lambda/L=0.85$ ).....	113
Figure 9-4. Time-histories from the CK test in head wave ( $\lambda/L=1.00$ ).....	114
Figure 9-5. Time-histories from the CK test in head wave ( $\lambda/L=1.15$ ).....	115
Figure 9-6. Time-histories from the CK test in head wave ( $\lambda/L=1.37$ ).....	116
Figure 9-7. Time-histories from the CK test in head wave ( $\lambda/L=1.95$ ).....	117
Figure 9-8. RAOs of 0th harm. amp. of heave/pitch in head waves.....	118
Figure 9-9. RAOs of 0th harm. amp. of thrust/torque coefficients in head waves .....	118

Figure 9-10. RAOs of 1st harm. amp. of heave/pitch in head waves .....	118
Figure 9-11. RAOs of 1st harm. amp. of thrust/torque coeff. in head waves .....	119
Figure 9-12. RAOs of 1st harm. phase of heave/pitch in head waves .....	119
Figure 9-13. RAOs of 1st harm. phase of thrust/torque coeff. in head waves.....	119
Figure 9-14. RAOs of added-powering var. in head waves.....	120
Figure 9-15. RAOs of 0th/1st harm. amp. of SP factors in head waves .....	121
Figure 9-16. RAOs of 1st harm. phases of SP factors in head waves.....	122
Figure 9-17. RAOs of 2nd harm. amp. of SP factors in head wave.....	122
Figure 9-18. RAOs of amp. and phase of relative motions in head waves.....	123
Figure 9-19. Longitudinal dist. of mean hydrodynamic x-force on the hull in head waves.....	124
Figure 9-20. Longitudinal dist. of mean hydrodynamic x-force on the prop. in head waves....	124
Figure 9-21. Validation of local flow in head wave .....	125
Figure 10-1. Time-histories from the CK test in oblique wave ( $\chi = 45^\circ$ ).....	140
Figure 10-2. Time-histories from the CK test in oblique wave ( $\chi = 90^\circ$ ).....	141
Figure 10-3. Time-histories from the CK test in oblique wave ( $\chi = 135^\circ$ ).....	142
Figure 10-4. Time-histories from the CK test in oblique wave ( $\chi = 180^\circ$ ).....	143
Figure 10-5. RAOs of 0th harm. amp. of heave/pitch in oblique waves .....	144
Figure 10-6. RAOs of 0th harm. amp. of roll in oblique waves .....	144
Figure 10-7. RAOs of 0th harm. amp. of yaw/rudder angle in oblique waves .....	144
Figure 10-8. RAOs of 0th harm. amp. of thrust/torque coeff. in oblique waves .....	145
Figure 10-9. RAOs of 1st harm. amp. of heave/pitch in oblique waves.....	145
Figure 10-10. RAOs of 1st harm. amp. of roll in oblique waves.....	145
Figure 10-11. RAOs of 1st harm. amp. of yaw/rudder angle in oblique waves .....	146
Figure 10-12. RAOs of 1st harm. amp. of thrust/torque coeff. in oblique waves.....	146
Figure 10-13. RAOs of 1st harm. phase of heave/pitch in oblique waves.....	146

Figure 10-14. RAOs of 1st harm. phase of roll in oblique waves .....	147
Figure 10-15. RAOs of 1st harm. phase of yaw/rudder angle in oblique waves .....	147
Figure 10-16. RAOs of 1st harm. phase of thrust/torque coeff. in oblique waves .....	147
Figure 10-17. RAOs of added-powering var. in oblique waves .....	148
Figure 10-18. RAOs of 0th harm. amp. of SP factors in oblique waves .....	149
Figure 10-19. RAOs of amp. and phase of relative motions in oblique waves .....	149
Figure 10-20. Longitudinal dist. of mean hydrodynamic x-force on the hull in oblique waves	150
Figure 10-21. Longitudinal dist. of mean hydrodynamic x-force on the prop.in oblique waves	150

## 1. INTRODUCTION

### 1.1. Motivation

An accurate estimation on the propulsion efficiency and the fuel consumption is becoming essential in a seaway as the demand for the energy efficient ship operation is increasing. The added-powering related to the fuel consumption is affected by the added-resistance and the decreased propulsion efficiency in waves. Being more specific, the main factors for estimating the added powering are: ship motions in waves; hull-propeller-rudder interactions; variations of propeller inflow velocity; and the propeller load fluctuations. Clarifying characteristics of these factors and knowing the co-relation through local/global flow measurements and simulations is becoming more necessary for designing a more energy efficient ship.

### 1.2. Background

#### **Added-resistance**

It is well known that a large portion of the added-powering is caused by the added-resistance. During the last decade, studies using computational fluid dynamics (CFD) have been assessing the added-resistance for various ship hulls: Carrica et al. (2007, 2011), Sadat-Hosseini et al. (2013, 2015), Simonsen et al. (2013), Wu et al. (2016), Kim et al. (2017), Seo et al. (2017), Sigmund and Moctar (2018).

Carrica et al. (2007) performed verification and validation (V&V) for the 2 degree of freedom (DOF) added-resistance test using David Taylor Model Basin (DTMB) 5512 frigate. Later on, Carrica et al. (2011) validated the added-resistance for Korea Research Institute of Ships and Ocean Engineering (KRISO) Container Ship (KCS) against 2010 Gothenburg CFD workshop (G2010) data and showed good agreements for motions. The agreement for the zeroth harmonic amplitude of resistance was close to the experiment data.

Sadat-Hosseini et al. (2013) investigated the motions and added resistance of KRISO Very Large Crude Carrier (KVLCC) 2 tanker advancing at Froude number ( $F_n$ ) 0.142 under surge fixed and surge free condition in head waves with a wide range of wave length conditions including very short waves using CFDShip-Iowa and Osaka University (OU) towing tank data. Added-resistance was the largest when the bow relative motion has largest amplitude and is about 180 degrees out of phase with the waves. Maximum responses occur near the resonance condition and near the maximum wave excitation force which is at  $\lambda/L = 1.33$  and long waves for surge/pitch and heave, respectively. Wu et al. (2014) performed extensions for the ballast condition.

Simonsen et al. (2013) investigated heave and pitch motions of KCS in regular head waves by towing tank data and CFD including CFDShip-Iowa, Star-CCM+ and AEGIR. Ship responded strongly when resonance and maximum excitation conditions are met. Data was used as the test case for G2010 (Larsson et al. 2014). Simonsen et al. (2014) investigated KCS added-resistance in regular head waves by towing tank data and CFD using Star-CCM+ including regular oblique waves. Added-resistance was maximum when resonance and maximum excitation/bow relative motion condition. Oblique wave response correlated with frequency of encounter resonance condition for heave/pitch, roll and parametric roll, but only qualitative validation was performed using available experimental data for another container ship.

Sadat-Hosseini et al. (2015) assessed CFD and linear potential flow (PF) methods using Iowa Institute of Hydraulic Research (IIHR) wave basin and FORCE technology (FORCE) towing tank data for the added-resistance test in regular head/oblique waves (surge free) and head waves (surge fixed), respectively. The oblique wave response trends were confirmed. The results showed a significant fluctuation in the wake field which can affect the propeller/engine performance. Additionally, it was found that the average propeller inflow nominal wake is significantly higher

in waves. The data was used as a test case for the Tokyo 2015 A Workshop on CFD in Ship Hydrodynamics (T2015) and NATO AVT-216 (Stern and Toxopeus, 2018).

Wu et al. (2016) performed V&V for the added-resistance test using KVLCC2 and investigated the source of the nominal wake fluctuation using local flow analysis. Kim et al (2017) also conducted added-resistance tests for KVLCC2 by using STAR-CCM+ commercial code and studied the effect of speed and wave steepness on the added-resistance by comparing the results with a 3D PF code. Seo et al. (2017) used OpenFOAM utilizing a mesh deforming method and performed V&V for KCS at various wave lengths. Sigmund and Moctar (2018) used OpenFOAM for various ship hulls (cruise ship, container ship, tanker, Wigley hull) for various wave lengths, validated the results and explained the difference in trends of added-resistance respect to hull form.

### **Speed-loss**

Shen et al. (2014) used OpenFOAM coupled with SUGGAR for the Hamburg Ship Model Basin (HSVA) KCS model and performed V&V. The mean values of the thrust and torque were close to the experiment, but the first harmonic phase of torque was out of phase.

Wang et al. (2017) used Unsteady Reynolds-averaged Navier–Stokes equations (URANS) for the free-running ONR Tumblehome frigate (ONRT) in both head and oblique waves and validated their results against IIHR experimental data submitted for the T2015 CFD workshop: ONRT test cases 3.12 and 3.13 (bow quartering and beam waves). The in-house OpenFOAM solver could handle the overset grids by being coupled with the SUGGAR and the ship had discretized propellers and rudders. The amount of speed loss was 17% for head waves, 9% for bow quartering waves and 2% for beam waves. The motions results except for roll angle and ship speed at certain conditions were in good agreement with the experiment in waves: The first harmonic amplitude of roll angle was under-predicted during the beam waves and the first harmonic

amplitude of the advance speed was under-predicted for the head and bow quartering waves, and the author pointed out that the variance of propeller rotational speed during the experiment could be the source of error for the advance speed. The mean rudder angle was found to stay at 3.2 degree for bow quartering waves and showed good agreement with the experiments. The author could detect that both thrust and torque coefficients become maximum during the bow heading up and vice versa due to the actual ship speed's increase/decrease at the same moment.

### **Added-powering**

Otzen et al. (2018) performed 2DOF URANS simulations for the 6.1m length KCS by using StarCCM+. A body force (BF) propeller model based on blade element theory was implemented. Propeller open-water test (POT), self-propulsion (SP) in calm water, self-propulsion in wave tests are conducted prior to the added-powering test like the current study. The results were close to the experimental data for motions and propeller characteristics during the added-powering tests, however, the prediction was less accurate than calm water cases due to the correction made on the body-force model which was set during the calm water tests.

Wu et al. (2018) performed 3DOF (surge-free) URANS simulations using CFDShip-Iowa V4.5. A BF model based on blade element theory is used. The results including the local flow validation showed good agreement compared to the experiment data for both calm and wave conditions.

### **1.3. Objective**

The studies for added-powering tests are limited due to the complicated test conditions and setup for both experiment and CFD. In the current study, the objective is to perform URANS V&V for free-running course-keeping and maneuvering simulations in calm water and free-running course-keeping (CK) in regular head/oblique waves by targeting the same Froude number,

including a wide range of test conditions and using both BF and actual propeller (AP) models with an active rudder for the 2.7m KCS model (Figure 1-1). The self-propulsion factors in wave conditions will be obtained to estimate the variance of the propeller efficiency and the propeller-hull interaction in wave condition. Integral values such as motions, forces and moments will be first analyzed and then the values will be investigated more locally to get more detailed information. The validation focusing on local flow analysis will be also performed for the resistance, self-propulsion and course-keeping tests.

#### **1.4. Approach**

CFDShip-Iowa V4.5 is used for the entire simulations. The V&V follows Stern et al. (2011) and Xing and Stern (2010). The simulation results are validated against free-running experimental data from the IIHR Wave basin. Sanada et al. (2017) provided integrated contemporaneous experimental studies. The research is in collaboration ONRG NICOP projects at FORCE, Denmark and Osaka University, Japan. OU and FORCE conducted added-powering measurements in regular head waves under surge-free and surge fixed conditions with different sizes of KCS model respectively to enable us to investigate the model size effect as well. Particle Image Velocimetry (PIV) data for the local flow validation is from OU. Some of the conditions are also the part of the test cases at the forthcoming Workshop on Verification and Validation of Ship Maneuvering Simulation Methods 2020 (SIMMAN 20) and Workshop on CFD in Ship Hydrodynamics: Wageningen 2021 (W2021).

## 2. BENCHMARK DATA, CFD TEST MATRIX AND COORDINATE SYSTEM

### 2.1. Hull, Propeller and Rudder Geometry

#### Bare-hull

KCS is a benchmark geometry that has been used for CFD validation at international CFD workshops, e.g. A Workshop on CFD in Ship Hydrodynamics: Gothenburg 2000 (G2000); Tokyo 2005 (T2005); G2010; T2015, and the SIMMAN 2008 and 2014 as shown in Figure 2-1.

Table 2-1 provides the particulars of the KCS including full scale, Maritime Research Institute Netherlands (MARIN), FORCE, OU, IIHR and CFD models. The main particular sub-section includes geometrical parameters that are used for generating the ship models. The non-dimensional values should be very close to each other to meet the similarity conditions. As for the model scale, MARIN and FORCE have the smallest scale ratio ( $\lambda_s$ ) and IIHR has the largest. The characteristic length ( $L$ ) for the non-dimensionalization is set to be the length between perpendiculars ( $L_{PP}$ ), not the length between waterline ( $L_{WL}$ ), and  $L = 2.7$  m is used for the current studies, i.e. the CFD model.

The particulars in the test condition sub-section can vary upon the setup from each facility while the same conditions are still desirable. For the current study, the variables are close to each other.

The  $Fn$  is targeting 0.26 for the entire simulations and the corresponding Reynolds number ( $Rn$ ) is listed in the table. The current CFD model will have 3.61M for  $Rn$  and is equipped with the studs at the bow to stimulate the turbulence (Sanada et al, 2017).

#### Propeller

The propeller is KP505 provided from KRISO and is meeting the geometrical similarity. The number of blade is 5 and the propeller center is located at  $x/L = 0.9825$  (from the forward

perpendicular) and  $z/L = 0.02913$  (below the waterline). The propeller always rotates clockwise when seen from the stern. The propeller hub cap is not included in the simulations.

## Rudder

The rudder is the horn type and the rotation axis is located at  $x/L = 1.00$  from the forward perpendicular (FP), which is the aft perpendicular. The part of the rudder is fixed to the bare-hull (BH) and does not move. Meanwhile, the moving part of the rudder is free to rotate along its vertical axis. The rudder wetted area and the lateral area values should meet the geometrically similarity. The deviation of the rudder angle and maximum rudder rate are limited to 35 degree and 21.5 deg/s for IIHR model, respectively.

## 2.2. Available Benchmark Experimental Data and CFD Test Matrix

Table 2-2 lists the CFD simulation cases and conditions. The cases cover: (1) propeller open water test; (2) free heave/pitch/roll decay; (3) resistance; (4) self-propulsion; (5) maneuvering in calm water; (6) self-propulsion and course-keeping for head waves; and (7) self-propulsion and course-keeping for oblique waves. The head/oblique wave course-keeping test is also called added-powering tests in the current study. Sanada et al. (2017) provides a detailed description of the experimental methods and results, including comparison with other facilities and assessment of facility biases.

### Case 1

Case 1 is performed for a wide advance coefficient ( $J$ ) range as listed in the table by assessing grid triplets: fine grid (G1); medium grid (G2) and coarse grid (G3). The propeller rotational speed ( $n$ ) is fixed to 20 revolution per second (rps) and the magnitude of incoming uniform flow is varied for each advance coefficient. The whole domain rotates at the same speed

with the propeller to compute the overset boundaries just once at the beginning of the simulation. The actual propeller is used and the propeller is non-dimensionalized with  $L$ , therefore, the corresponding  $Rn$  is also based on  $L$ . Thrust coefficient ( $K_T$ ), torque coefficient ( $K_Q$ ) and open water propeller efficiency ( $\eta_0$ ) are provided from IIHR, FORCE, OU and a few more facilities (Sanada et al. 2017), but the current CFD validates only against IIHR.

## Case 2

Heave and pitch decay tests inside Case 2 are conducted only for CFD. For heave ( $z$ ) and pitch ( $\theta$ ) decay tests, the initial conditions are:  $z/L = 0.0469 = T/L$  and  $\theta = 5^\circ$ , respectively and G3 is used. The values are set to exert high restoring force, and thus, to overcome the large damping. After the model stays a short time at the initial condition, the constraint is lifted and the model moves with 6DOF. When the model's certain motion is imposed with the initial value, the rest of the motions are free to move. However, the staying time is so short during the simulation that the other motion's effects on the result are negligible. Analytical data is used for the validation of the heave and pitch natural frequencies.

For the free roll ( $\phi$ ) decay test, CFD mimics the initial conditions of IIHR (Sanada et el. 2017) and both  $\phi = 8.9^\circ$  and  $20.1^\circ$  are used for both G2 and G3, however, the  $\phi = 8.9^\circ$  condition is not preferred than  $\phi = 20.1^\circ$  due to the insufficient restoring force. The process of simulation is the same as free heave/pitch decay tests. Initial roll angle will be imposed for a very short time, and then the model will be freed. IIHR provides time-history of roll. During the entire free decay tests, the ship does not equip the propeller and the absence of it can reduce the damping especially in the free roll decay test, however, the amount is not considered.

### **Case 3**

Case 3 is performed in the ship fixed coordinate with the incoming flow. The BH is equipped with the rudder. 2DOF simulation is performed. Resistance ( $X$ ), sinkage ( $\sigma$ ) and trim ( $\tau$ ) are provided from 2DOF IIHR and FORCE experiments. Grid triplets are assessed for the verification of sinkage, trim, resistance and nominal wake.

### **Case 4**

Case 4 consists of: without rudder, fixed rudder and proportional-integral-derivative (PID) controlled rudder cases. Simulation is conducted in 6DOF free-running conditions with both body force and actual propeller conditions. Grid triplets are used for the AP condition and only G2, G3 for the BF conditions. The model is put at target  $Fn$  for a short time at the beginning of the simulation to reduce the time required to reach to the steady state. The condition w/o the rudder is performed to check the effect of the presence of the rudder during the self-propulsion test. In the later chapter, the propeller mean wake is qualitatively compared for w/o rudder and fixed rudder conditions by comparing the streamlines. Also, the difference of the total resistance is also noted. When the rudder is at presence, the effect of the neutral rudder angle ( $\delta_N$ ), which keeps the ship's course straight, is discussed by comparing the fixed rudder and PID controlled rudder conditions. The proportional gain ( $K_P$ ) of 80, integral gain ( $K_I$ ) of 120 and derivative gain ( $K_D$ ) of 0 are used for both propeller rotational speed and rudder angle, which is different from IIHR, but the values do not need to be identical since the model reaches to the steady state. IIHR provides the trajectory and time histories of heave, roll, pitch, yaw ( $\psi$ ), x-velocity ( $u$ ), propeller rotational speed, thrust coefficient, torque coefficient and rudder angle when the ship is at free-running condition. OU performed surge-free 2DOF experiments and provided PIV data which is measured after the flow passes the rudder.

## **Case 5**

Case 5 consists of:  $\pm 35^\circ$  turning-circle,  $\pm 10^\circ/10$  zig-zag and  $\pm 20^\circ/20$  zig-zag tests. The tests start once the calm water SP is fully converged with two different conditions for both BF and AP: fixed rudder and PID controlled rudder, to check the sensitivity of the initial conditions. The propeller rotational speed that is obtained from the calm water self-propulsion test is fixed during the whole simulation. MARIN and IIHR also performed free-running tests and provided trajectory and time histories of roll, yaw, x-velocity, y-velocity ( $v$ ), yaw rate ( $r$ ) and rudder angle. G3 is preferred initially, however, G2 is also tested to check if G3 worked properly.

## **Case 6 – 7**

Since the added-powering tests for case 6 and 7 are performed with the fixed propeller rotational speed, finding the propeller rotational speed that puts the ship at the target  $F_n$  is needed for each wave length ( $\lambda$ ) and heading angle ( $\chi$ ) ahead of running actual added-powering tests. The propeller rotational speed in wave is always higher than the one obtained from the calm water self-propulsion test. Due to the high cost of computational time, only G3 is used. Self-propulsion tests in wave is done with both 2DOF and 6DOF for the head wave and with 6DOF for the oblique wave. In the 2DOF test, the model is constrained and the propeller rotated with three different propeller rotational speed. The final propeller rotational speed should give the total resistance near to zero and is determined by the linear interpolation. The 6DOF test setup is not necessarily different from the actual added-powering test but it refers to the intermediate stage that seeks for the propeller rotational speed that gives the  $F_n$  very close to the target value. 6DOF self-propulsion test in waves is performed when the propeller rotational speed determined from the 2DOF self-propulsion test in waves often fails to predict the target  $F_n$ . IIHR finds the propeller rotational

speed by trial and error seeking the target  $Fn$ , and the 6DOF SP test procedure is the same as the IIHR.

Added-powering tests for case 6 and 7 are performed with free-running conditions, self-propelled, with the active rudder the same as the calm water self-propulsion test with active rudder. The model has a sudden speed at the beginning of the simulation just like the calm water self-propulsion test. The PID gains for the active rudder are  $K_P=1.00$ ,  $K_I=0.05$  and  $K_D=4.00$ , and the values should be identical to IIHR since the model undergoes the unsteady environment. The wave steepness ( $H/\lambda$ ) is always 1/60 and the wave length ( $\lambda/L$ ) ranges from 0.65 to 1.95 for head wave conditions. Among wave length range,  $\lambda/L = 1.15$  condition is very close to the heave natural frequency ( $f_z$ ) and the pitch natural frequency ( $f_\theta$ ) as shown in Figure 2-3 and resonance occurs. For the oblique wave conditions, the wave steepness is also 1/60 and the wave length is 1.00 for five different heading angles:  $\chi = 0^\circ, 45^\circ, 90^\circ, 135^\circ$  and  $180^\circ$ . 6DOF free-running IIHR could provide the trajectory and time histories of heave, roll, pitch, yaw, x-velocity, propeller rotational speed, thrust coefficient, torque coefficient and rudder angle for both head and oblique waves. 2DOF FORCE and surge-free 2DOF OU could provide response amplitude operators (RAO) of heave, pitch, propeller rotational speed, thrust coefficient and torque coefficient for only head waves since the experiments are performed in towing tanks. OU also provided PIV data for  $\lambda/L = 0.65, 1.15$  and  $1.37$  conditions. The measurement location is identical to the location measured in the calm water self-propulsion test case.

### 2.3. Coordinate System

#### Bare-hull

Figure 2-2(a) presents the ship (black) and carriage-fixed (red) coordinate systems. Both CFD and experiment data are described in ship-fixed coordinate system by default. The only data

uses the carriage-fixed coordinate system is the OU PIV data. The carriage-fixed coordinate, whose origin is located at  $x=0$  (from FP),  $y=0$  and  $z=0$  (waterline), does not move with the ship motions. For the ship fixed coordinate system: the  $x$ -coordinate directs head-ward, so the total resistance is negative and the thrust coefficient is positive, always; roll is positive when the ship is inclined to the starboard, therefore, the ship has always negative roll for +35 turning-circle test; the  $y$ -coordinate directs starboard, which gives positive pitch angle when the bow heads up; the  $z$ -coordinate directs downward, so the yaw is positive when the ship heads to starboard; The generated wave elevation ( $\zeta$ ) in the CFD, whose crest starts at time ( $t$ ) equals zero, also follows the ship coordinate system.

### **Propeller and rudder**

Figure 2-2 (b) presents the propeller (blue), rudder (green) the local coordinates and the location of the slices obtained in the ship coordinate system (V1-4) and the carriage-fixed coordinate (V5). The propeller local coordinate system is sharing the same sign of the  $x$ -coordinate with the ship (head-ward positive), and therefore, the thrust and torque coefficients are always positive since the propeller rotates clockwise. The  $z$ -coordinate of the rudder is positive upward, so the rudder angle and the angle of attack (AoA) of the rudder are positive when the rudder tail is located at the starboard. Four vertical slices (V1-4) and five horizontal slices (H1-5) are located during the post-process stage for the analysis of the local flow. V1, located right before the propeller ( $x/L = 0.975$  from FP), is used for the calculation of the nominal wake fraction coefficient ( $\omega$ ) and the effective wake fraction coefficient ( $\omega_e$ ). V5, located after the rudder ( $x/L = 1.025$  from FP), is used for the PIV comparison. H1-5 are used for the calculation of the AoA on the leading edge of the rudder as well as for the mean flow in the  $x$ - $y$  plane.

Table 2-1. Main particular and appendage information

Symbol	Description	Full scale	MARIN	FORCE	OU	IIHR	CFD
<b>Main particular</b>							
$\lambda_s$	Scale	1	37.89	37.89	71.88	85.19	85.19
$L_{PP} (= L)$	Length between perpendiculars [m]	230	6.0702	6.0702	3.2	2.7	2.7
$L_{wl}$	Length between waterlines [m]	232.5	6.1355	6.1362	3.2348	2.7293	2.7293
$B_{WL} (= B)$	Beam [m]	32.2	0.8498	0.850	0.448	0.378	0.378
$D$	Depth [m]	19	0.5015	0.501	0.264	0.223	0.223
$C_B$	Block coefficient ( $\nabla/LBT$ )	0.651	0.651	0.651	0.651	0.651	
$C_M$	Midship section coefficient	0.985	0.985	0.9849	0.9849	0.9849	
<b>Test condition</b>							
$T/L$	Draft	0.046957	0.046951	0.046951	0.046969	0.046963	0.046956
$\nabla/L^3$	Displacement volume	0.00428	0.00428	0.00428	0.00427	0.00427	0.00428
$A_w/L^2$	Wetted area (w/o rudder)	0.1802	0.1802	0.1796	0.1802	0.1802	0.1805
$LCG/L$	LCG (w/o rudder, from AP)	0.4852	0.4852	0.4852	0.4853	0.4852	0.4848
$KG/L$	VCG (from keel)					0.0622	0.0622 <sup>(1)</sup>
$T_z/(L/U)$	Natural heave period (freq)			<sup>(3)</sup> 0.453 (2.21)		<sup>(3)</sup> 0.455 (2.20)	<sup>(4)</sup> 0.463 (2.16)
$T_\theta/(L/U)$	Natural pitch period (freq)			<sup>(3)</sup> 0.453 (2.21)		<sup>(3)</sup> 0.455 (2.20)	<sup>(4)</sup> 0.450 (2.22)
$T_\phi/(L/U)$	Natural roll period (freq)			<sup>(3)</sup> 2.204 (0.45)		<sup>(4)</sup> 1.958 (0.51)	<sup>(4)</sup> 1.946 (0.51)
$GM/L$	Metacentric height	0.00261	0.00264	0.00260	0.00250	0.00259	0.00253
$K_{xx}/B$	x-dir. Moment of Inertia	0.4	0.4	0.4	0.4	0.39	0.447 <sup>(2)</sup>
$K_{yy}/L$	y-dir. Moment of Inertia	0.25	0.25	0.252	0.25	0.25	0.25 <sup>(1)</sup>
$K_{zz}/L$	z-dir. Moment of Inertia	0.25	0.25	0.252	0.25	0.25	0.25 <sup>(1)</sup>
<b>Rudder</b>							
$A_{w,rud}$	Wetted area of rudder [ $m^2$ ]	115	0.0801	0.0801	0.0223	0.0158	
$A_{wL,rud}$	Lateral area of rudder [ $m^2$ ]	54.45	0.0379	0.0379	0.0105	0.0075	
$r_{rud}$	Max. rate of rudder deflection [deg/s]	2.32	14.3			21.5	21.5 <sup>(1)</sup>
$r_x/L$	x-dir. Rudder axis (from FP)	1.00				1.00	1.00
<b>Propeller</b>							
Type		FP	FP	-	FP	FP	FP
$N_p$	Number of propeller blades	5	5	-	5	5	5
$D_p$	Propeller diameter [m]	7.9	0.208	-	0.110	0.093	0.093
$P/D_p$	Propeller pitch/diameter ratio (at 0.7R)	0.997	0.997	-			
$A_e/A_o$	Blade area ratio	0.8	0.748	-	0.8	0.8	0.8
$D_h/D_p$	Hub ratio	0.18	0.186	-	0.180	0.180	0.18
$p_x/L$	x-dir. Propeller center (from FP)					0.9825	0.9825 <sup>(1)</sup>
$p_z/L$	z-dir. Propeller center (below WL)					-0.02913	-0.02913 <sup>(1)</sup>
<b>Service speed in deep water</b>							
$u$	Speed in x-dir. [m/s]	24 [kn]	2.005	2.017	1.456	1.34	1.34
$F_n$	Froude number (based on $L_{PP}$ )	0.26	0.26	0.26	0.26	0.26	0.26
$R_n$	Reynolds number [ $\times 10^6$ ]	2841	12.18	12.18	4.66	3.61	3.61

<sup>(1)</sup>Experimental data is directly used

<sup>(2)</sup> $K_{xx}/B=0.39, 0.43$  were also tested ahead and were adjusted to current value

<sup>(3)</sup>From hydrostatic calculation <sup>(4)</sup>From decay test

**Table 2-2. CFD test matrix**

Test	DOF	$F_n/J$	$R_n$ [M]	$\delta$ [deg]	$H/\lambda$	$\lambda/L$	$\chi$ [deg]	Grid used
<b>Calm Water</b>								
POT <sup>(3)</sup> (20 RPS)	1 ( $FR_\phi$ )	0.036/0.10 0.072/0.20 0.145/0.40 0.217/0.60 0.253/0.70 0.271/0.75 0.286/0.79 0.289/0.80 0.325/0.90	0.50 1.00 2.01 3.01 3.51 3.77 3.98 4.02 4.52				0	G1, G2, G3
Heave decay Pitch decay Roll decay	6	0		0				G3 G2, G3
Resistance	2 ( $FR_{Z\theta}$ )	0.26	3.61	0			0	G1, G2, G3
Self-propulsion	6	0.26	3.61	w/o Rud 0 PID <sup>(1)</sup>			0 (targeted)	G1, G2, G3
Turning-circle	6	0.26	3.61	35 -35				G2, G3
Zig-zag	6	0.26	3.61	10 -10 20 -20				G2, G3
<b>Head Wave</b>								
Self-propulsion (Captive)	2 ( $FR_{Z\theta}$ )	0.26	3.61	0	1/60	0.65 0.85 1.00 1.15 1.37 1.95	0	G3
Self-propulsion (Free-running)	6	0.26	3.61	0	1/60	0.65 0.85 1.00 1.15 1.37 1.95		G3
Course-keeping (Added Powering)	6	0.26	3.61	PID <sup>(2)</sup>	1/60	0.65 0.85 1.00 1.15 1.37 1.95	0 (targeted)	G3
<b>Oblique Wave</b>								
Self-propulsion	6	0.26	3.61	PID <sup>(2)</sup>	1/60	1.00	45 90 135 180	G3
Course-keeping	6	0.26	3.61	PID <sup>(2)</sup>	1/60	1.00	45 (targeted) 90 (targeted) 135 (targeted) 180 (targeted)	G3

<sup>(1)</sup>  $K_p=80$ ,  $K_I=120$  and  $K_D=0$  are used but the values are subject to any values

<sup>(2)</sup>  $K_p=1.0$ ,  $K_I=0.05$  and  $K_D=4.0$  same as used in the experiment

<sup>(3)</sup>  $R_n$  is based on L and U



Figure 2-1. KCS hull appended with the propeller and the rudder

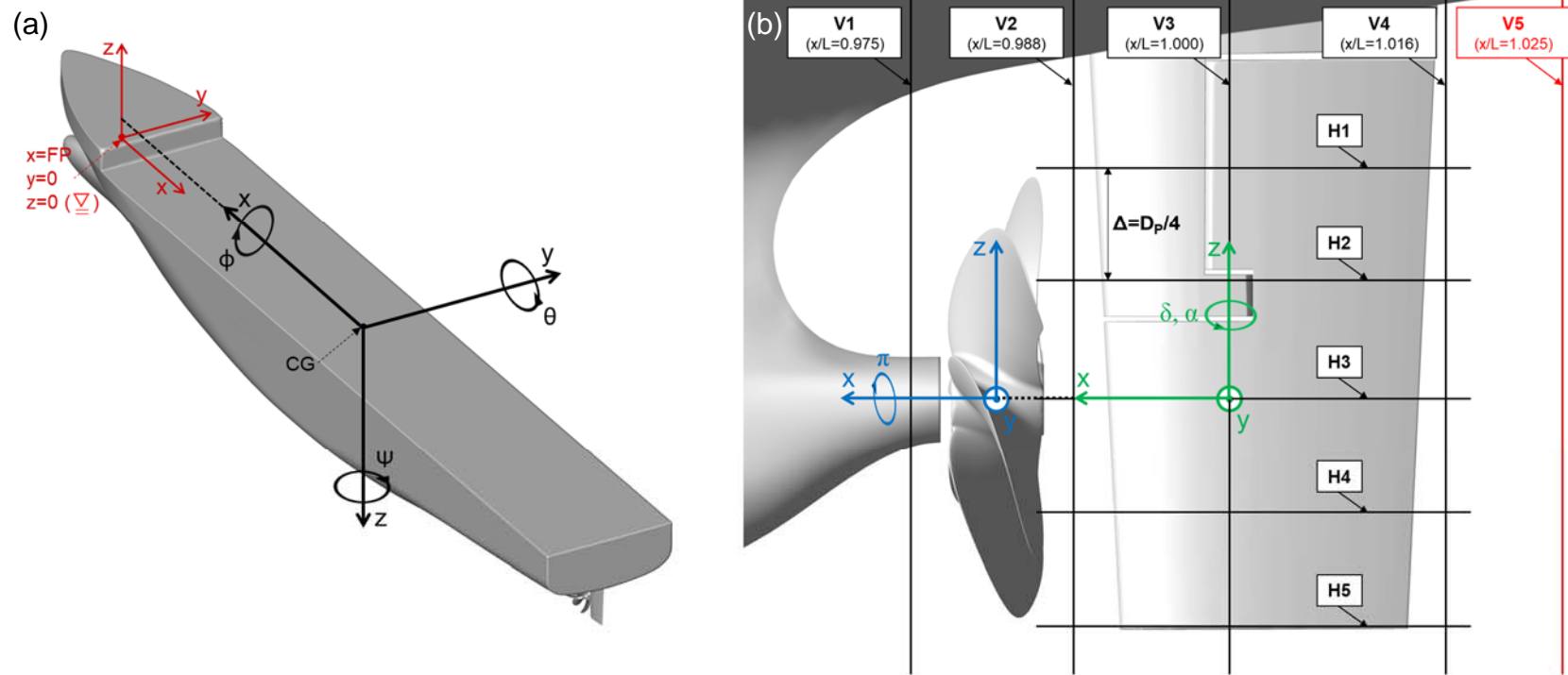


Figure 2-2. Coordinate system: (a) ship (black) and carriage (red); (b) propeller (blue) and rudder (green)

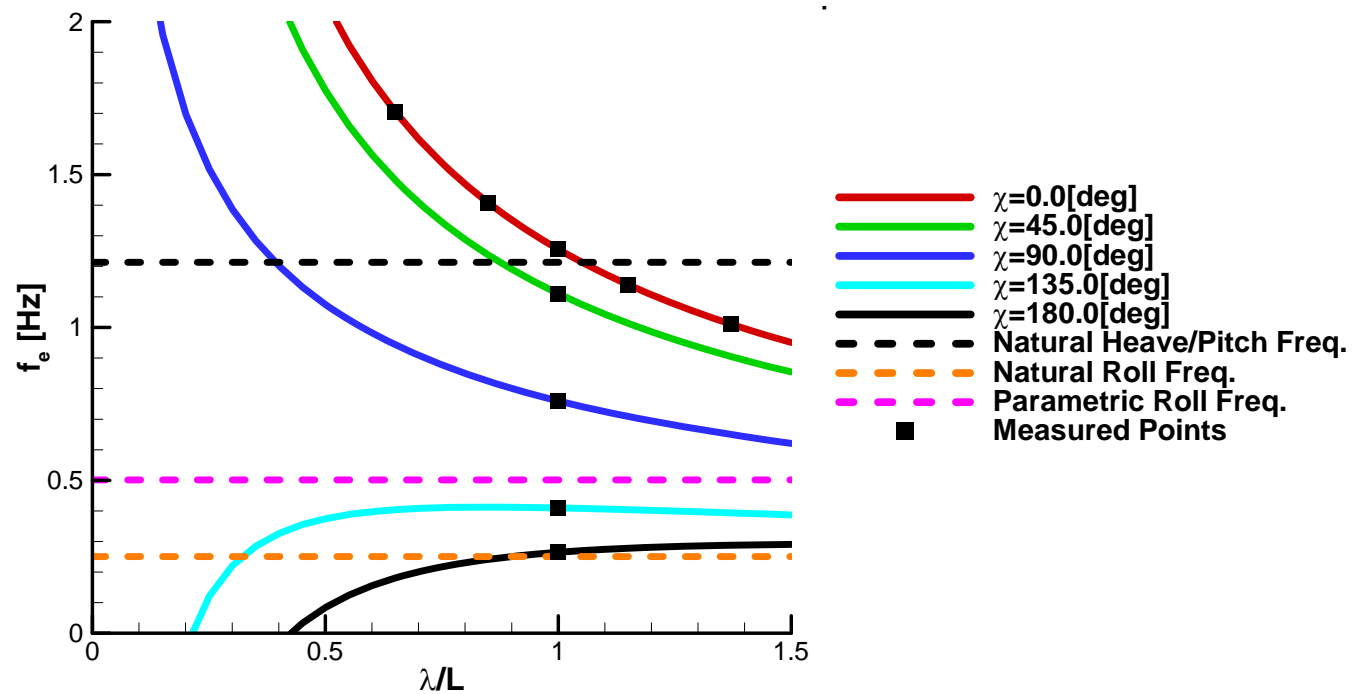


Figure 2-3. Natural/encounter frequencies and points of interest for  $Fn = 0.26$  KCS

### 3. COMPUTATIONAL & ANALYSIS METHODS

#### 3.1. CFDShip-Iowa V4.5, Modelling and HPC

##### **CFDShip-Iowa V4.5**

CFDShip-Iowa, which has been developed since 1980s, is a general-purpose Unsteady Reynolds Averaged Navier-Stokes (URANS) and Detached Eddy Simulation (DES) code that has been utilized and validated for many ship hydrodynamic topics. The version of the code used for the current studies is V4.5 (Carrica et al. 2011) which is the successor of V3 (Paterson et al. 2003). CFDShip-Iowa V4.5 solves the URANS in the non-inertial ship coordinate system. The body-fitted coordinate and the non-orthogonal system can be considered and uses a structural grid composition due to its solid theoretical background, the higher chance of adopting the higher order schemes and the greater scalable ability during the parallel computation compared to the unstructured grid formulation.

##### **Modelling**

Dynamic motions of a solid body are predicted without harming/deforming the quality of the grid with the use of the overset strategy: the SUGGAR library is used. The free-surface is captured with a single-phase level-set method (Carrica et al. 2007). For the turbulence model, the code uses a linear closure model and  $k - \omega/k - \varepsilon$  blended model for the Reynolds stresses and the eddy viscosity, respectively. PETSc is utilized for solving the matrix. The body-force propulsion uses an axisymmetric model and its radial distribution of forces follows the Hough and Ordway circulation.

## **High performance computing**

The test cases are performed in a couple of different HPCs: Gordon & Conrad from NAVY-DSRC, and Neon from the University of Iowa.

### **3.2. Grids**

Tables 3-1 briefly presents the total grid sizes of the grid system used for each test case.

#### **Case 1**

All grid triplets are used. The number of grid points and the number of computing cores used for the fine/medium/coarse grid systems (G1/G2/G3) are 28/10/3.4M and 250/96/28. The propeller model is the discretized AP that is also used for the other AP cases in calm water and waves. The propeller grid is enclosed by the refinement and background grids, which are Cartesian.

#### **Case 2, 3, 4 and 5**

Cases 3 and 4 use all grid triplets. Case 2 and 5 are only performed with G2 and G3 to avoid the excessive use of computational cost. The grid system is comprised of bare-hull, rudder, propeller, refinements and background grids. 102/36/12M grid points and 897/343/116 cores are used for G1/G2/G3 AP conditions. Since BF condition shares the same grids with AP except for the propeller, the amount of grid points/cores accounts for the propeller part is reduced for BF condition.

#### **Case 6**

Case 6 uses the same grids as case 2 to 5 except for the background grid. The number of grid points of the background grid is changed in all three directions for each wave condition to retain the consistent wave resolution in the wave field, e.g. 15 and 60 grid points per wave

amplitude ( $A/L$ ) and wave length (for G3). G2 and G3 is used with BF and AP, respectively, however, G1 is refrained.

### **Case 7**

Lastly, case 7 enlarge the size of the background grid to accommodate the wave coming from the lateral sides, however, the resolution for the wave field remains the same. G2-BF and G3-AP are used like case 6.

### **Grid generation**

Table 3-2 shows the grid sizes of each block comprising the grid systems. The bare-hull is divided into 10 blocks for each portside and starboard, 6 blocks for each sides of the fixed rudder, 7 blocks for each sides of the moving rudder and 11 blocks for the propeller. The grid sets that are y-symmetric such as the bare-hull and the rudder are originally generated on the starboard side of the database and then mirrored respect to  $y=0$  so that the half-domain simulations will also be feasible even though there is no need for the present study due to the free-running condition and the model is single screw propelled. The grid system used for the current study is having limited number of blocks that are generated as double-O type topology like many previous studies did, however, most of blocks are rather overlapped side by side. The purpose of using many overlapped blocks is: to test the extreme condition in grid formulation and verify the capability of the current overlap grid formulation strategy; to have less issues during the domain extrusion stage which has always been regarded as a bottleneck during the grid generation procedure. The extrusion issue especially becomes troublesome and time consuming when the geometry is complicated such as a propeller, a bulbous bow, a stern and a rudder. The users are usually hindered from choosing the right topology intuitively and even if it comes up after a decent amount of time, the quality is not certified for the grid that is having complex topology. By overlapping more simple blocks rather

than using the complicated shaped ones, the extrusion goes much smoother and the process in real tasks does not require the user to put random coefficients in the hyperbolic extrusion functions inside the grid generating tool that is usually done by the trial and error until the completion of the extrusion (sometimes requires excessive number of iterations). Consequently, the high quality of the grid could be generated. The shortcoming of using many blocks like the current study arises, though, when the closed body is detected as an open body by the overset library. When the body is not regarded as closed, the hole cutting procedures often fails and requires users to undergo manual treatments to blank the grids inside the closed body by putting the cutter grids or by just taking out certain grid points manually. This manual work task takes time but once the body is ensured as closed, no further works is required during the computations.

### **Grid composition**

Refinement grids are usually located near the region that requires more resolution or smooth connectivity between the grids. It is conventional to put the large and fine refinement block around the ship, i.e., Ref-Stern and Ref-Ship in Table 3-2, to give high resolution on the free-surface near the ship, and it also helps to gradually decrease the grid resolution between the ship and the background grid: background grid is usually coarser than the refinement grid to avoid excessive use of grids, especially in the far field. The refinement grids for the rudder, i.e. Ref-RF-X and Ref-RM-X in Table 3-2 (X is 1-3), are used to give smoother connectivity inside the rudder gap where the fixed rudder and the moving rudder blocks meet each other. The connectivity issue is also checked when the moving rudder part rotates along its axis to avoid having any orphan grid points, which does not have any connectivity with the near grids, during the active rudder simulations. Propeller refinements, i.e. Ref-POT and Ref-PropDisk in Table 3-2, mainly work to increase the resolution near the propeller and to capture the propeller tip vortices that might affect

the mean rudder angle. Figure 3-2 and Figure 3-3 provides views of the surface grids of the grid triplets for the hull and rudder and propeller, respectively.

### 3.3. Domain size

Figure 3-1 shows the domain sizes and boundary conditions used for the simulations.

#### Case 1

For case 1, the entire grids were submerged into deep water by being translated to  $z/L = 1$  with respect to the free-surface not to be affected by the free-surface. The inlet for the POT located 5 timed propeller diameter ( $D_p$ ) ahead from the propeller and outlet is located  $27D_p$  away from the propeller. The lateral distance from the propeller to the sides are  $5.5D_p$ .

#### Case 2 – 6

For case 2 to 6, the inlet, outlet, bottom and top are  $1.2L$ ,  $2L$ ,  $1.5L$  and  $0.5L$  away from the ship, respectively, and the free-surface is located at  $z/L = 0$ . The steady state solution often showed oscillations with the specified domain size, so an attempt to enlarge the domain size is performed, however, the result did not show much of difference.

#### Case 7

For case 7, the distance between the ship and the inlet, sides are enlarged to  $2L$  from the head wave case to constantly use the same background grid for all the wave headings.

### **3.4. Boundary Conditions**

Table 3-3 shows the boundary condition equations used for the simulations.

#### **Case 1**

The boundary conditions for case 1 consists of inlet (#10), outlet (#11) and sides (#40, zero-gradient). For case 1, the whole grid moves with the same speed of propeller rotation: simulation is ship coordinated, and there could be some pressure residue on the sides of the far-field regions, but its effects are regarded negligible.

#### **Case 2 – 5**

Boundary conditions for the case 2 to 5 consists of inlet (#10), outlet (#11), top (#13), bottom (#12) and sides (#40).

#### **Case 6 – 7**

For both case 6 and 7, the boundary conditions on the sides are changed to wave (#17) condition. Note that it is the exact solutions that are imposed at all 4 sides, not the wave signal from the experiment. More details on the exact solution can be found from the Equation 1 in Chapter 3.5. No special treatments were used to damp the wave reflection.

### **3.5. Numerical Schemes and Case Setup**

This section includes the CFDShip-Iowa V4.5 options that are chosen and used to run the current simulations.

#### **Discretization schemes**

The following numerical schemes/values are used for the entire simulations: fourth order upwind for the convection term in the momentum equation; second order upwind for the level-set

convection term; second order backward for the temporal term in the momentum equation; second order upwind for turbulent convection; 6DOF integration method is the explicit first order with 8-point smoothing for case 3 to 7 and the second-order implicit for the case 2.

### **Tolerances and relaxation factors**

$3.0e^{-4}$  for the wave blanking;  $1.0e^{-7}$  for the artificial level-set diffusion (reinitialization at every non-linear iteration);  $1.0e^{-5}$ ,  $1.0e^{-6}$ ,  $1.0e^{-6}$ ,  $1.0e^{-3}$  for the tolerances of non-dimensionalized velocities, pressure, level-set and non-linear iteration; projection method for pressure solver; 0.8 and 0.9 for the relaxations in momentum and pressure equations.

### **Time step**

The time step is  $5.246e^{-3}$  for BF condition and 12.5 times smaller for AP condition; amount of time step used for case 1 accounts for 1.2 degree per iteration.

### **Inertia reduction and damping coefficient**

10 for surge inertia reduction and 500 damping coefficients for heave, pitch, roll and yaw are applied for case 4, while nothing is treated for the other tests

### **Wave**

The generated wave used for the current study is the Stokes second-order wave:

$$\begin{aligned} \eta(x, y, t) = & a \cos[k(x \cos \chi - y \sin \chi) - \omega_W t] \\ & + \frac{a^2 k}{4} \frac{\cosh(kd)}{\sinh^3(kd)} [2 + \cosh(2kd)] \cos\{2[k(x \cos \chi - y \sin \chi) - \omega_W t]\} \end{aligned} \quad (1)$$

where  $a$  is the wave amplitude,  $k$  is the wave number,  $\omega_W$  is the wave frequency and  $d$  is the water depth. No wave damping model was used near the far field boundaries.

## PID controller

The PID controller equations for the propeller rotational speed and rudder angle are as follow:

$$n(t) = K_P(u - u_{target}) + K_I \int_0^t (u - u_{target}) dt + K_D \frac{d(u - u_{target})}{dt} \quad (2)$$

$$\delta(t) = K_P(\psi - \psi_{target}) + K_I \int_0^t (\psi - \psi_{target}) dt + K_D \frac{d(\psi - \psi_{target})}{dt} \quad (3)$$

The equations are essentially in identical form for both propeller rotational speed and rudder angle. The equations update values based on the linear, integral and derivative errors calculated for every iteration.

Table 3-1. Sizes of grid systems

Case	$\lambda/L$	Number of total grid points [M] (proc.)					
		G1 (fine)		G2 (medium)		G3 (coarse)	
		BF	AP	BF	AP	BF	AP
POT		28 (250)		10 (96)		3.4 (28)	
Calm Water		88 (768)	102 (897)	31 (292)	36 (343)	11 (103)	12 (116)
Head Wave	0.65			64 (590)	69 (641)		
	0.85			49 (454)	54 (505)		
	1.00	121 (1073)	136 (1202)	43 (400)	48 (451)	15 (141)	17 (154)
	1.15			39 (368)	44 (419)		
	1.37			36 (336)	41 (387)		
	1.95			31 (299)	36 (350)		
Oblique Wave	1.00	147 (1302)	161 (1431)	52 (481)	57 (532)	18 (170)	20 (183)

**Table 3-2. Detail of grid size**

Part	Location	Applied Case	G1 (fine)			G2 (medium)			G3 (coarse)			
			Direction		ijk [M]	Direction		ijk [M]	Direction		ijk [M]	
			i	j	k	i	j	k	i	j	k	
<b>Bare-Hull</b>												
Mid	Sb, Pt (x2)		254	95	211	5.09	46	179	67	149	1.8	
Wave Break	Sb, Pt (x2)		196	94	87	1.60	14	138	66	61	0.6	
Bow Upper	Sb, Pt (x2)		73	99	118	0.85	7	51	70	83	0.3	
Bulbous Bow	Sb, Pt (x2)	calm water,	73	95	97	0.67	6	51	67	68	0.2	
Stern	Sb, Pt (x2)	head wave,	83	97	152	1.22	11	58	68	107	0.4	
Stern-Cap	Sb, Pt (x2)	oblique wave	36	99	152	0.54	4	25	70	107	0.2	
Stern-Cap2	Sb, Pt (x2)		53	99	53	0.28	2	37	70	37	0.1	
Near Hub	Sb, Pt (x2)		53	90	104	0.50	4	37	63	73	0.2	
Near Hub-Cap	Sb, Pt (x2)		70	81	124	0.70	6	49	57	87	0.2	
Near Hub-Cap2	Sb, Pt (x2)		33	67	53	0.12	1	23	47	37	0.0	
<b>Rudder Fixed</b>												
RF-Front	Sb, Pt (x2)		75	77	186	1.07	9	53	54	131	0.37	
RF-BackUpper	Sb, Pt (x2)	calm water,	124	70	105	0.91	8	87	49	74	0.32	
RF-Mid	Sb, Pt (x2)	head wave,	71	77	254	1.39	12	50	54	179	0.48	
RF-MidUpper	Sb, Pt (x2)	oblique wave	53	77	61	0.25	2	37	54	43	0.09	
RF-Down	Sb, Pt (x2)		183	77	77	1.09	9	129	54	54	0.38	
RF-DownUpper	Sb, Pt (x2)		83	53	71	0.31	2	58	37	50	0.11	
<b>Rudder Moving</b>												
RM-Upper	Sb, Pt (x2)		163	83	94	1.27	11	115	58	66	0.44	
RM-Upper2	Sb, Pt (x2)	calm water,	163	85	63	0.87	7	115	60	44	0.30	
RM-Down	Sb, Pt (x2)	head wave,	133	81	114	1.23	11	94	57	80	0.43	
RM-Mid	Sb, Pt (x2)	oblique wave	95	87	57	0.47	4	67	61	40	0.16	
RM-MidFront	Sb, Pt (x2)		73	75	80	0.44	3	51	53	56	0.15	
RM-MidFrontUpper	Sb, Pt (x2)		133	61	73	0.59	5	94	43	51	0.21	
RM-MidFrontDown	Sb, Pt (x2)		163	56	73	0.67	6	115	39	51	0.23	
<b>Propeller</b>												
Hub	Center		119	63	433	3.25	29	84	44	306	1.13	
Blade-Bottom	Axisym. (x5)	calm water,	163	67	121	1.32	12	115	47	85	0.46	
Blade-Tip	Axisym. (x5)	head wave, (only for AP), POT	101	67	131	0.89	8	71	47	92	0.31	
<b>Refinement</b>												
Ref-POT	Center	POT	200	200	200	8.00	72	141	141	141	2.8	
Ref-RF-1	Sb, Pt (x2)		143	60	60	0.51	4	101	42	42	0.18	
Ref-RF-2	Sb, Pt (x2)		60	60	143	0.51	4	42	42	101	0.18	
Ref-RF-3	Sb, Pt (x2)		71	60	60	0.26	2	50	42	42	0.09	
Ref-RM-1	Sb, Pt (x2)	calm water,	85	115	115	1.12	10	60	81	81	0.39	
Ref-RM-2	Sb, Pt (x2)	head wave,	85	115	104	1.02	9	60	81	73	0.35	
Ref-RM-3	Sb, Pt (x2)	oblique wave	83	115	115	1.10	9	58	81	81	0.38	
Ref-PropDisk	Center		363	94	63	2.15	19	256	66	44	0.74	
Ref-Stern	Center		258	145	254	9.50	86	182	102	179	3.32	
Ref-Ship	Center		317	133	323	13.62	123	224	94	228	4.8	
<b>Background</b>												
BG-POT	Center	POT	194	168	168	5.48	49	137	119	119	1.94	
BG-Calm	Center	calm water	251	163	227	9.29	84	177	115	160	3.26	
BG-HW065	Center	$\lambda/L=0.65$					549	394	167	36.12	328	
BG-HW085	Center	$\lambda/L=0.85$					422	300	167	21.14	192	
BG-HW100	Center	$\lambda/L=1.00$	504	360	236	42.82	389	357	255	167	15.20	
BG-HW115	Center	$\lambda/L=1.15$					312	224	167	11.67	106	
BG-HW137	Center	$\lambda/L=1.37$					261	187	167	8.15	74	
BG-HW195	Center	$\lambda/L=1.95$					184	133	167	4.09	37	
BG-OW	Center	oblique wave	$\lambda/L=1.0$	601	480	236	68.08	618	425	340	167	24.13
							219	300	240	118	8.50	77

Table 3-3. Detail of boundary conditions (Carrica et al. 2011)

	$\phi$	$p$	$k$	$\omega$	$U$	$V$	$W$
#9 <i>inlet</i>	$\phi = -z$	$\frac{\partial p}{\partial n} = 0$	$k_{fs} = 10^{-7}$	$\omega_{fs} = 9$	$U = ufullspd$	$V = vfullspd$	$W = wfullspd$
#10 <i>Far inlet</i>	$\phi = -z$	$p = 0$	$k_{fs} = 10^{-7}$	$\omega_{fs} = 9$	$U = ufullspd$	$V = vfullspd$	$W = wfullspd$
#11 <i>exit</i>	$\frac{\partial \phi}{\partial n} = 0$	$\frac{\partial p}{\partial n} = 0$	$\frac{\partial k}{\partial n} = 0$	$\frac{\partial \omega}{\partial n} = 0$	$\frac{\partial^2 U}{\partial n^2} = 0$	$\frac{\partial^2 V}{\partial n^2} = 0$	$\frac{\partial^2 W}{\partial n^2} = 0$
#12 <i>Very far-field</i>	$\phi = 0$	$p = 0$	$\frac{\partial k}{\partial n} = 0$	$\frac{\partial \omega}{\partial n} = 0$	$\frac{\partial U}{\partial n} = 0$	$\frac{\partial V}{\partial n} = 0$	$\frac{\partial W}{\partial n} = 0$
#13 <i>far-field</i>	$\frac{\partial \phi}{\partial n} = 0$	$\frac{\partial p}{\partial n} = 0$	$\frac{\partial k}{\partial n} = 0$	$\frac{\partial \omega}{\partial n} = 0$	$\frac{\partial U}{\partial n} = 0$	$\frac{\partial V}{\partial n} = 0$	$\frac{\partial W}{\partial n} = 0$
#17 <i>waves</i>	Exact solution	Exact solution	$k_{fs} = 10^{-7}$	$\omega_{fs} = 9$	Exact solution	Exact solution	Exact solution
#20 <i>no slip (ship wall)</i>	$\frac{\partial \phi}{\partial n} = 0$	Not needed	$k = 0$	$\omega = \frac{60}{Re \beta y^{+2}}$	$U = \frac{\partial x}{\partial t}$	$V = \frac{\partial y}{\partial t}$	$W = \frac{\partial z}{\partial t}$
#40 <i>zero gradient</i>	$\frac{\partial \phi}{\partial n} = 0$	$\frac{\partial p}{\partial n} = 0$	$\frac{\partial k}{\partial n} = 0$	$\frac{\partial \omega}{\partial n} = 0$	$\frac{\partial U}{\partial n} = 0$	$\frac{\partial V}{\partial n} = 0$	$\frac{\partial W}{\partial n} = 0$

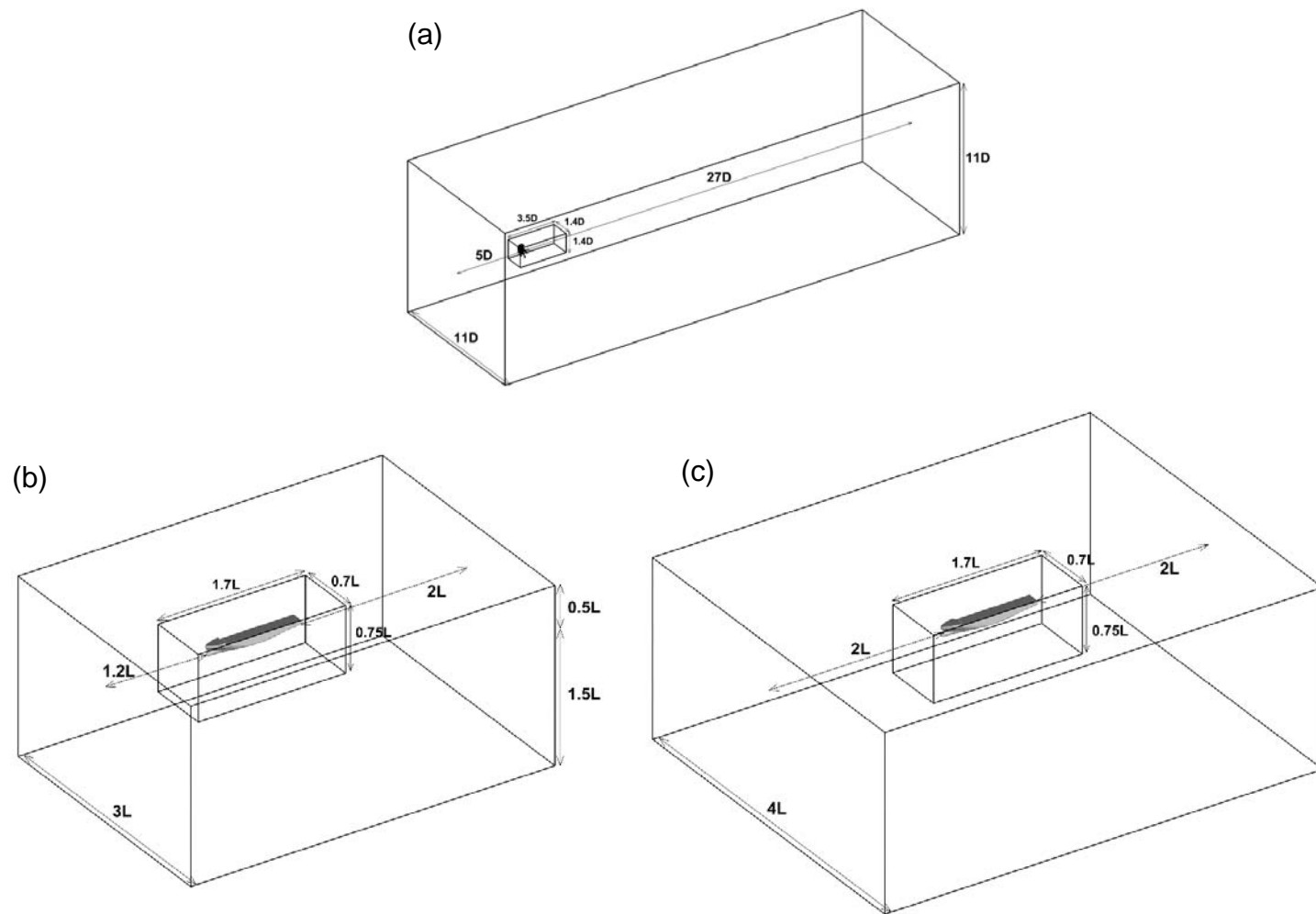


Figure 3-1. Domain sizes: (a) POT; (b) calm water & head wave; (c) oblique wave

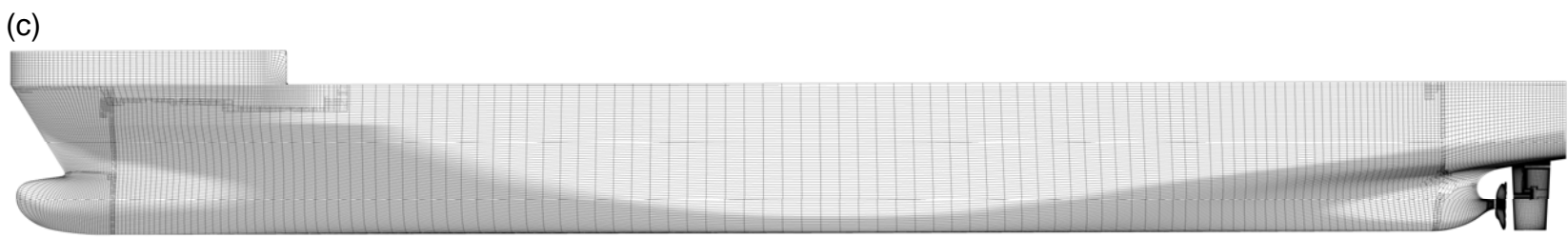
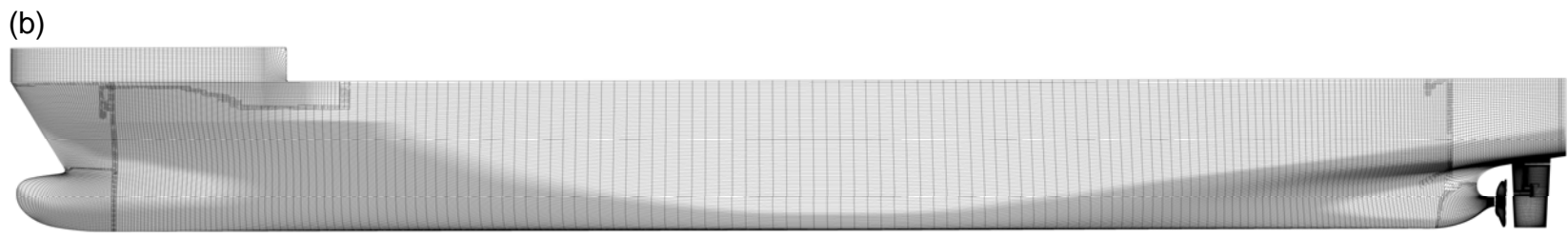
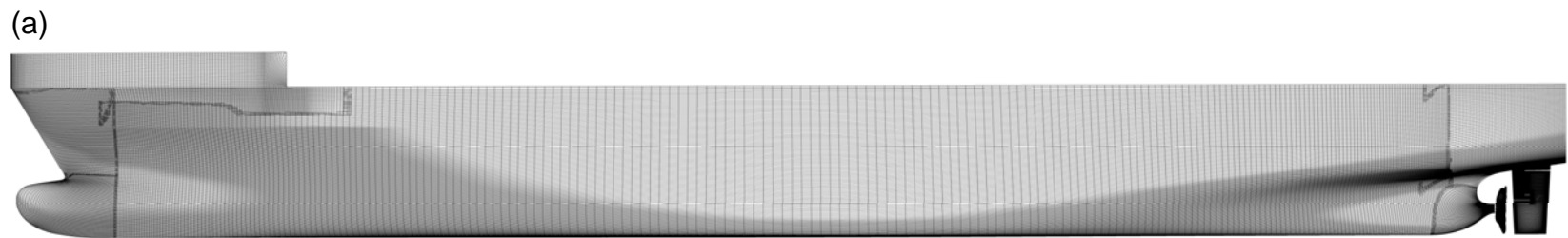


Figure 3-2. Surface grids of the bare-hull: (a) G1; (b) G2; (c) G3

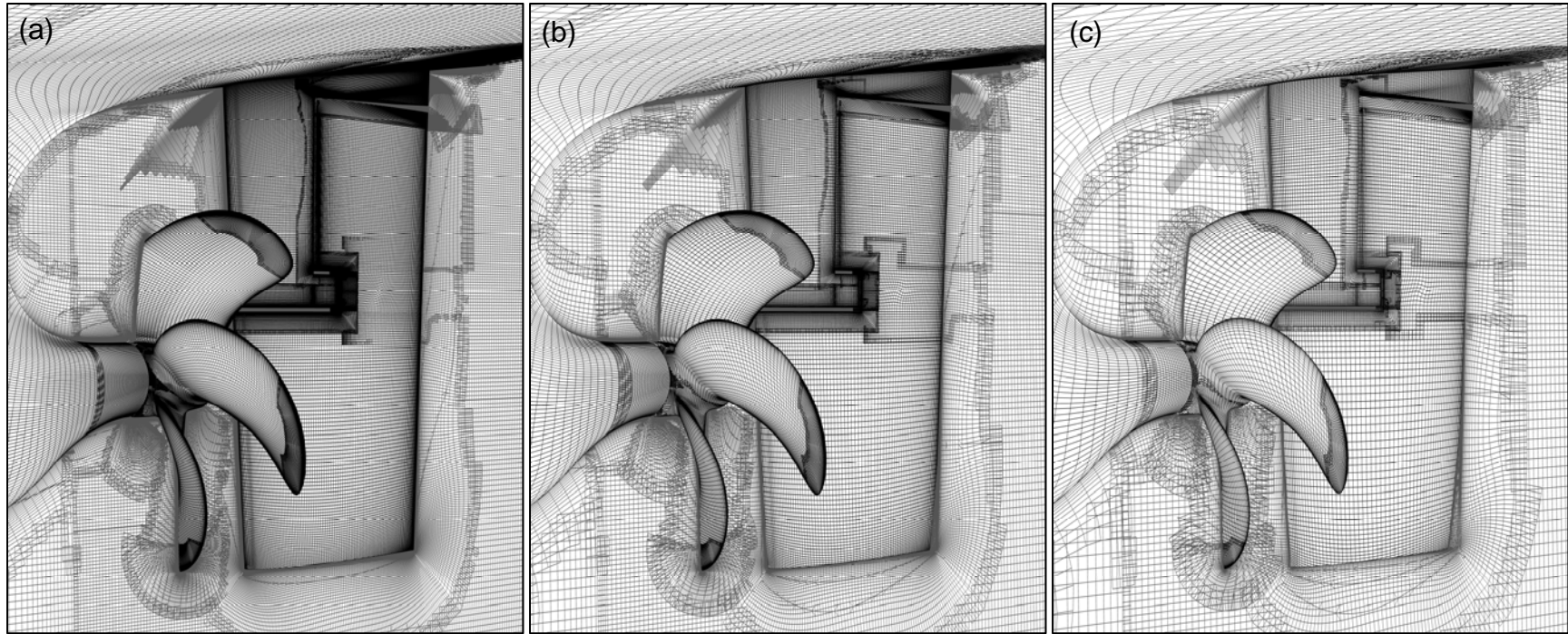


Figure 3-3. Surface grids of KP505 and rudder ( $y=0$  included): (a) G1; (b) G2; (c) G3

## 4. PROPELLER OPEN WATER TEST

### 4.1. Verification

Table 4-1 provides the verification results. The verification includes the grid size study only since the tests using AP uses minuscule time step. Three variables: thrust coefficient, torque coefficient and open water propeller efficiency, are verified for 8 different advance coefficients. Only 1, 4 and 6 of the 8 advance coefficient conditions display the monotonic convergence (MC) or oscillatory convergence (OC) for thrust coefficient, torque coefficient and open water propeller efficiency, respectively. The iterative uncertainties ( $U_I\%S_1$ ) are relatively large in comparison to  $\varepsilon_{21}\%S_1$  for  $J > 0.6$  which makes it difficult to assess grid convergence. Larger grid refinement ratio is needed such that differences between the solutions on the grids triplets are larger than the iterative convergence, which requires coarser or even finer grids. The resultant grid uncertainty ( $U_G$ ) values are large for thrust coefficient, reasonable for torque coefficient and small for open water propeller efficiency, i.e., 28, 7.9 and 1.3% $S_1$  in average, respectively. The experimental uncertainty ( $U_D$ ) is the scattering of the experimental values for the geosyms (Sanada et al. 2017), and it is relatively large for  $J > 0.7$ . Figure 4-1 shows the convergence histories for all advance coefficient conditions.

### 4.2. Validation

Table 4-2 provides the POT validation results. The experiment is done for two different propeller rotational speeds: 15 and 20 rps, and CFD used  $n = 20$  rps since the experiment for the  $n = 15$  rps condition is considered less reliable due to low  $Rn$  effects. Although the overall relative error is fairly small ( $E \leq 4\%D$ ), the errors on average increase with grid resolution, which is undesirable. Still, the errors are much smaller than the validation uncertainties for all three variables. Figure 4-2 graphically compares the simulation and experimental results.

### **4.3. Surface Pressure**

Figure 4-3 shows the instantaneous dynamic pressure distributions on the suction side and the pressure side for the grid triplets' propellers at  $J = 0.79$ , which is the SP point. The amount of difference between grid triplets is not significant and thereby not investigated in the current study.

### **4.4. Vortex Core**

In Figure 4-4, the Q-criterion ( $Q$ ) 300 iso-surfaces are presented to visualize the vortices behind the propeller. The amount of vortices is detected sensitive to the grid resolution when  $Q = 300$  is used.

Table 4-1. Verification results for the POT

$J$	$U_I\%S_I$	$\varepsilon_{2I}\%S_I$	$\varepsilon_{32}\%S_I$	$R$	$Conv.$	$P$	$U_G\%S_I$	$U_{SN}\%D$	$U_D\%D^{(l)}$	$U_V\%D$
$K_T$										
0.10										
0.10	0.1	-1.99	-2.33	0.85	MC	0.11	27.5	27.5	3.5	27.7
0.20	0.03	-0.90	-0.44	2.05	MD			0.03	3.4	3.4
0.40	0.03	-0.91	0.69	-1.32	OD			0.03	3.7	3.7
0.60	0.2	0.43	-0.27	-1.62	OD			0.2	5.7	5.7
0.70	0.4	0.61	0.12	5.08	MD			0.4	9.1	9.1
0.75	0.8	0.85	0.38	2.26	MD			0.8	12.8	12.8
0.80	0.7	1.38	0.73	1.88	MD			0.7	16.2	16.2
0.90	2.3	5.50	2.23	2.46	MD			2.2	41.1	41.2
Ave.	<b>0.6</b>						<b>27.5</b>	<b>4.0</b>	<b>11.9</b>	<b>15.0</b>
$10 * K_Q$										
0.10										
0.10	0.1	-1.27	-0.73	1.73	MD			0.1	2.3	2.3
0.20	0.03	-0.26	0.73	-0.36	OC		0.4	0.4	2.4	2.5
0.40	0.03	0.14	1.55	0.09	MC	1.74	0.2	0.2	2.7	2.7
0.60	0.2	0.79	0.55	1.44	MD			0.2	3.6	3.6
0.70	0.3	1.07	1.32	0.81	MC	0.15	10.5	9.9	5.0	11.1
0.75	0.5	1.44	1.68	0.86	MC	0.11	20.5	19.3	6.6	20.4
0.80	0.4	2.12	1.95	1.09	MD			0.4	7.2	7.2
0.90	0.8	4.47	2.86	1.56	MD			0.8	12.8	12.8
Ave.	<b>0.3</b>						<b>7.9</b>	<b>3.9</b>	<b>5.3</b>	<b>7.8</b>
$\eta_0$										
0.10										
0.10	0.01	-0.73	-1.63	0.45	MC	0.58	1.2	1.2	4.5	4.7
0.20	0.01	-0.64	-1.16	0.55	MC	0.43	1.6	1.7	4.5	4.8
0.40	0.01	-1.05	-0.83	1.26	MD			0.0	5.2	5.2
0.60	0.05	-0.35	-0.80	0.44	MC	0.59	0.5	0.6	6.5	6.5
0.70	0.1	-0.45	-1.17	0.39	MC	0.69	0.5	0.6	8.6	8.6
0.75	0.3	-0.58	-1.25	0.46	MC	0.56	1.0	1.1	10.8	10.8
0.80	0.3	-0.73	-1.15	0.63	MC	0.33	2.7	2.8	13.3	13.5
0.90	1.5	0.99	-0.60	-1.64	OD			1.6	29.8	29.9
Ave.	<b>0.3</b>						<b>1.3</b>	<b>1.2</b>	<b>10.4</b>	<b>10.5</b>

Table 4-2. Validation results for the POT

J	D (IIHR)		S			E%D (D=15 rps)			E%D (D=20 rps)							
	15 rps	20 rps	G1	G2	G3	G1	G2	G3	G1	G2	G3					
			20 rps													
<i>K<sub>T</sub></i>																
0.10	0.445	0.458	0.457	0.448	0.437	-2.7	-0.7	1.7	-0.3	1.4	2.9					
0.20	0.400	0.412	0.414	0.410	0.408	-3.6	-2.6	-2.2	-1.3	-0.4	-0.2					
0.40	0.304	0.316	0.313	0.310	0.312	-3.0	-2.0	-2.7	-0.5	0.6	-0.1					
0.60	0.202	0.213	0.207	0.208	0.207	-2.7	-3.1	-2.9	1.0	1.1	1.4					
0.70	0.148	0.158	0.154	0.155	0.155	-4.0	-4.7	-4.8	1.3	1.3	1.4					
0.75	0.120	0.130	0.127	0.128	0.128	-5.5	-6.4	-6.8	1.5	1.2	1.0					
0.80	0.092	0.102	0.099	0.100	0.101	-7.8	-9.3	-10.0	1.6	0.8	0.2					
0.90	0.034	0.044	0.041	0.044	0.045	-20.0	-26.6	-29.3	6.1	1.4	-0.8					
Ave.						<b>6.2</b>	<b>6.9</b>	<b>7.5</b>	<b>1.7</b>	<b>1.0</b>	<b>0.99</b>					
10 * K <sub>Q</sub>																
0.10	0.711	0.698	0.688	0.679	0.674	3.2	4.4	5.2	1.7	2.7	3.0					
0.20	0.652	0.641	0.623	0.622	0.626	4.5	4.7	4.0	2.3	2.6	1.7					
0.40	0.528	0.518	0.492	0.493	0.500	6.8	6.7	5.2	4.1	4.1	2.7					
0.60	0.392	0.384	0.363	0.366	0.368	7.3	6.6	6.1	4.2	3.9	3.4					
0.70	0.320	0.313	0.295	0.299	0.302	7.8	6.8	5.6	4.4	3.8	2.7					
0.75	0.283	0.276	0.261	0.264	0.269	8.0	6.6	5.1	4.5	3.5	2.1					
0.80	0.246	0.238	0.225	0.230	0.234	8.4	6.5	4.7	4.7	3.0	1.3					
0.90	0.168	0.161	0.148	0.155	0.159	11.7	7.8	5.3	7.3	3.6	0.9					
Ave.						<b>7.2</b>	<b>6.3</b>	<b>5.1</b>	<b>4.2</b>	<b>3.4</b>	<b>2.2</b>					
$\eta_0$																
0.10	0.100	0.104	0.106	0.105	0.103	-6.2	-5.4	-3.6	-2.0	-1.2	-0.1					
0.20	0.195	0.205	0.211	0.210	0.208	-8.4	-7.7	-6.5	-3.7	-3.0	-1.9					
0.40	0.367	0.388	0.405	0.401	0.398	-10.5	-9.3	-8.4	-4.8	-3.7	-2.8					
0.60	0.491	0.528	0.544	0.542	0.538	-10.8	-10.4	-9.5	-3.4	-2.9	-2.0					
0.70	0.514	0.564	0.580	0.577	0.570	-12.8	-12.3	-11.0	-3.2	-2.6	-1.4					
0.75	0.506	0.564	0.580	0.577	0.569	-14.6	-13.9	-12.5	-3.2	-2.4	-1.1					
0.80	0.477	0.545	0.561	0.557	0.551	-17.7	-16.8	-15.5	-3.3	-2.4	-1.2					
0.90	0.293	0.394	0.399	0.403	0.401	-36.0	-37.4	-36.5	-2.0	-2.7	-2.1					
Ave.						<b>14.6</b>	<b>14.2</b>	<b>12.9</b>	<b>3.2</b>	<b>2.6</b>	<b>1.6</b>					

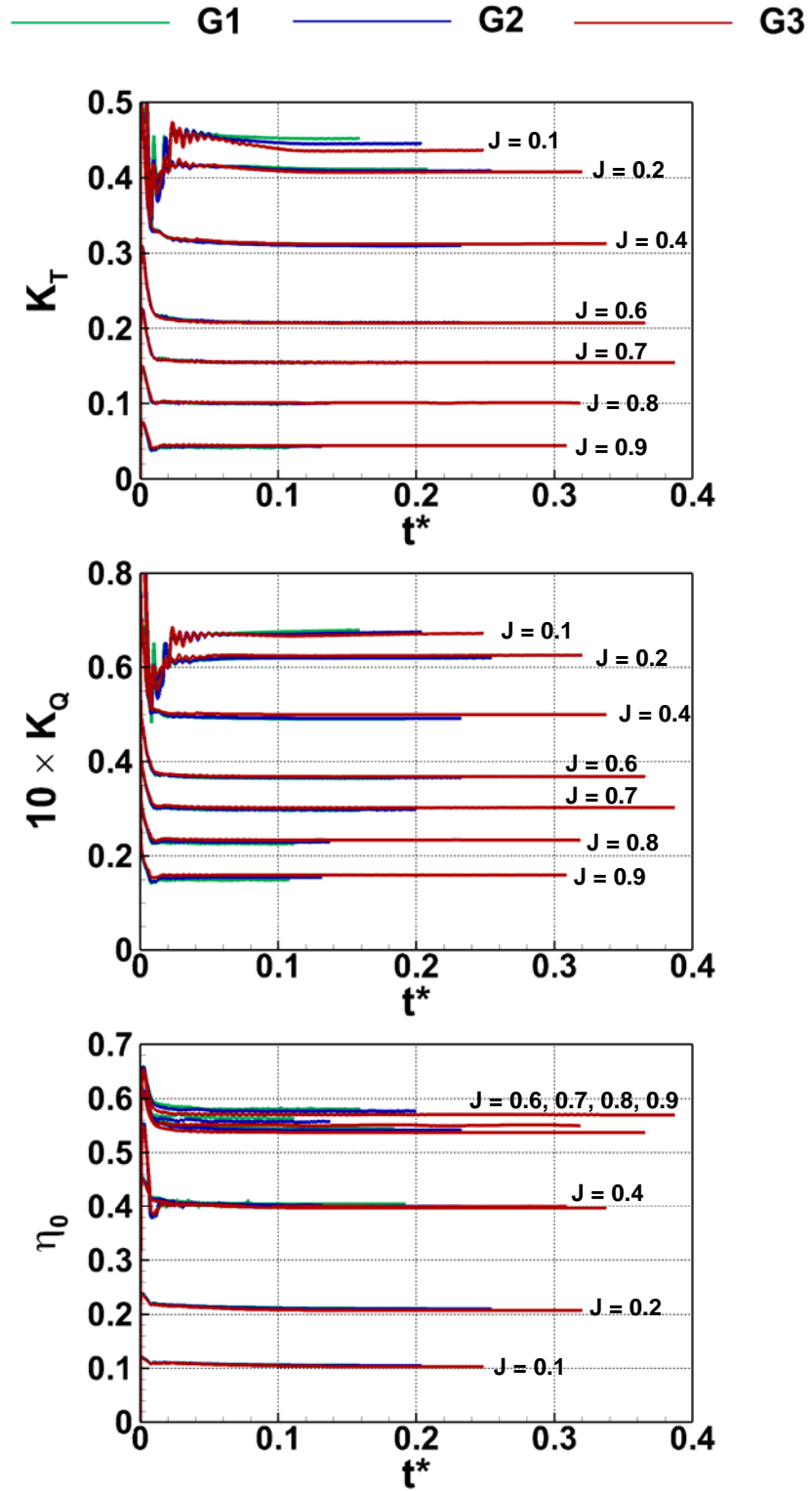


Figure 4-1. Time-histories from POT simulations

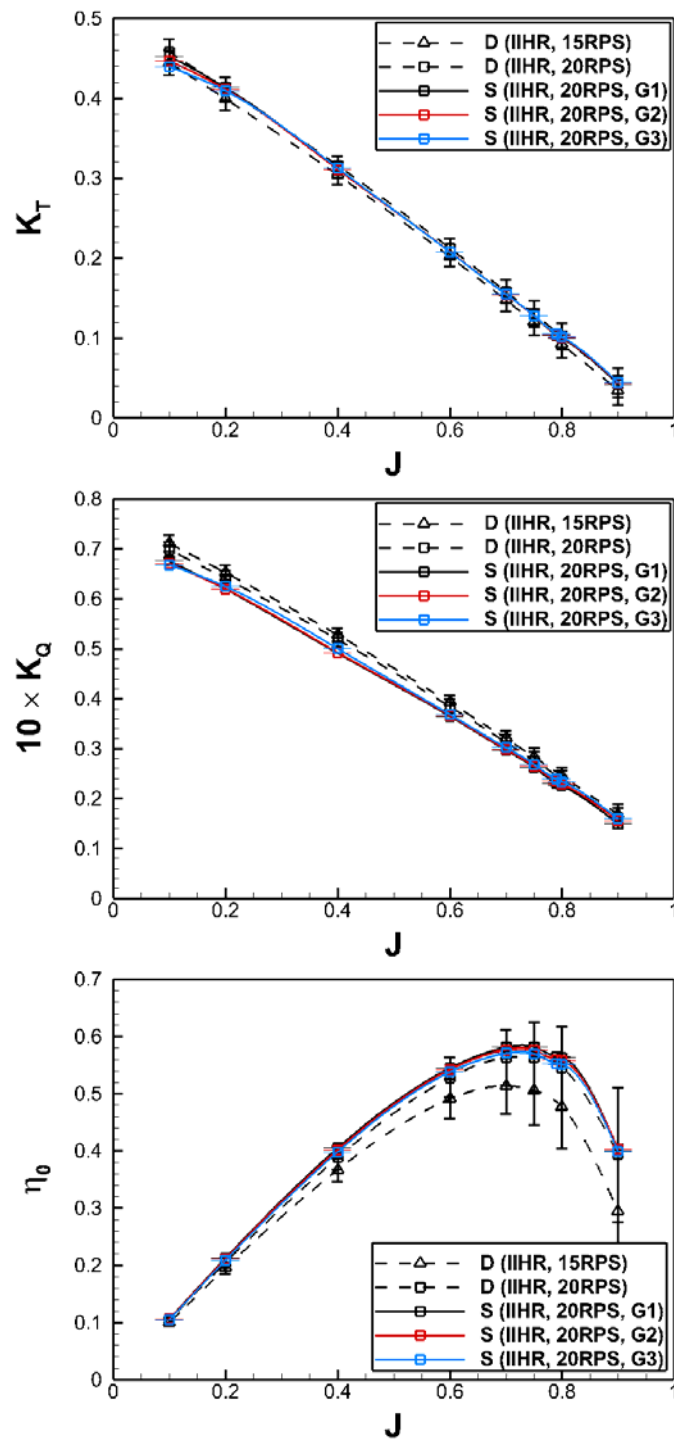


Figure 4-2. Validation results for the POT (bars for D show SD of 5 different experiments, bars for S show grid uncertainty)

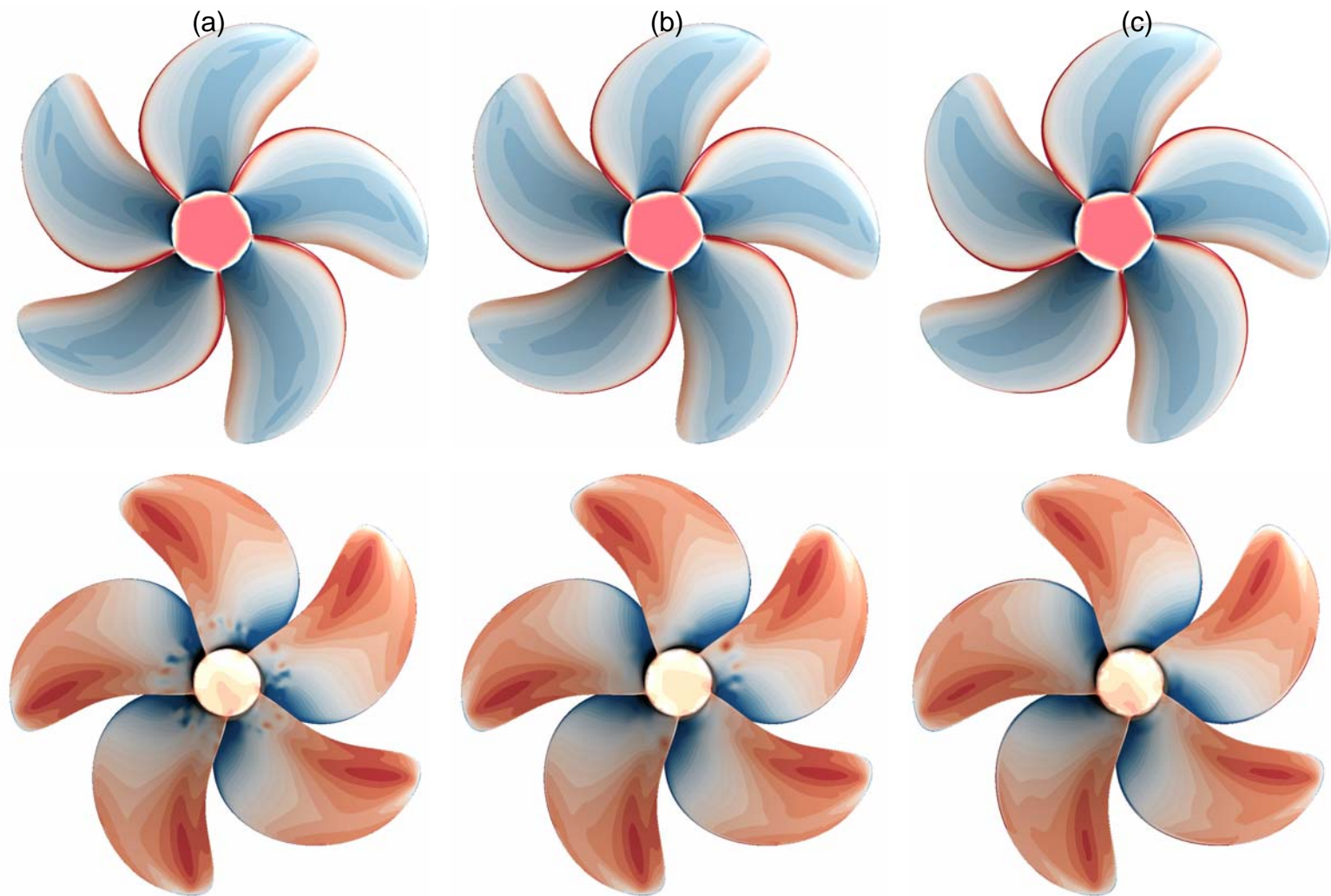


Figure 4-3. Dynamic pressure distributions on the propeller suction/pressure sides (SP point): (a) G1; (b) G2; (c) G3

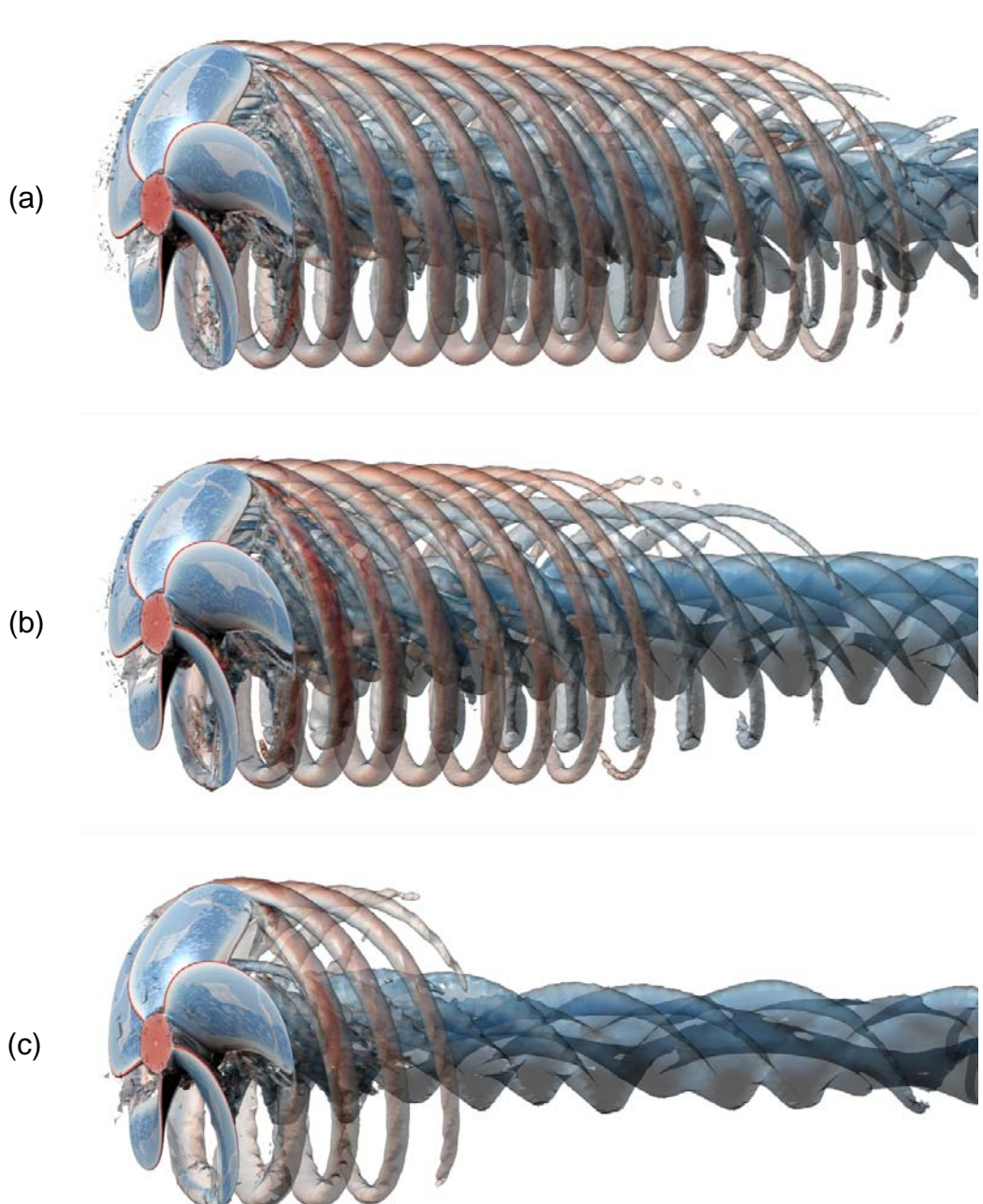


Figure 4-4. Dynamic pressure distributions and  $Q = 300$  (SP point): (a) G1; (b) G2; (c) G3

## 5. HYDROSTATIC SETUP AND DECAY TESTS

### 5.1. Hydrostatic Setup

Table 5-1 shows the hydrostatic setup results. The IIHR model ship used for the experiment is molded from the input database and CFD uses the identical database for the grid generation. For CFD, the hydrostatic computation is performed for the ship at even keel in calm water. The location of the longitudinal center of gravity (*LCG*) is moved longitudinally until the trim moment becomes negligible. The dimensionless draft (*T/L*) and displacement volume ( $\nabla/L^3$ ) are computed to be 0.0469 and 0.000427, and the  $E\%D$  are 0.01% and -0.04%.  $E\%D$  for the wetted area ( $A_w/L^2$ ) is -0.21%, which is satisfactory. The *LCG* of IIHR, 0.4852, is the designed value, and the *LCG* of CFD, 0.4848, is computed to be very close: 0.0007%  $E\%D$ .

### 5.2. Free Heave Decay

#### Setup and methodology

Table 5-2 shows the validation of the free heave decay results. Damped periods are calculated from the time history of heave as shown in Figure 5-1, and the values are validated against the empirical solution for the natural heave frequency ( $\omega_z$ ), which is calculated by referring Sadat-Hosseini et al. (2012):

$$\omega_z = 2\pi\sqrt{gC_{WP}/(8\pi^2C_B T)} \quad (4)$$

where  $C_B$  is the block coefficient,  $T$  is the draft and  $C_{WP}$  is the water plane area coefficient.

#### Validation

Until the first one and half cycle, the damped period matches with the empirical value with small error (<3.4  $E\%D$ ) for both initial conditions ( $z/L = 0.02, 0.047$ ). The error increases as the

decay continues due to the large damping. Therefore, the damped period at the first cycle of simulation is considered as natural heave period and reported as CFD data in Table 5-1. The analytical natural period is reported as IIHR data since the experiment is not available.

### 5.3. Free Pitch Decay

#### Setup and methodology

Table 5-3 shows the free pitch decay validation results. Same as the free heave decay test validation results, the damped period is calculated from the pitch time history as shown in Figure 5-2, and the values are validated against the empirical solution for natural frequency of pitch ( $\omega_\theta$ ) referred from Sadat-Hosseini et al. (2012):

$$\omega_\theta = 2\pi \sqrt{gB^3 C_{IT} / (96\pi^2 \hat{I}_y L^4)} \quad (5)$$

where  $C_{IT}$  is the y-directional coefficient of the inertia of the water plane area,  $\hat{I}_y$  is the y-directional non-dimensional mass moment of inertia.

#### Validation

Similar to the free heave decay test, only the damped periods up to the first one and half cycle are valid (<1.1 E%D), therefore, the first damped period is reported as natural pitch period in Table 5-1 for CFD, which is the least period affected by the damping, and the empirical solution for the natural frequency of pitch is reported for IIHR.

### 5.4. Free Roll Decay

#### Setup and methodology

Table 5-4 shows the validation results for free roll decay test. Time-histories used for the analysis is shown in Figure 5-3. Two initial roll angles: small ( $\phi = 8.92^\circ$ ) and large ( $\phi = 20.16^\circ$ )

are used. The x-directional radius of gyration ( $k_{xx}$ ) measured from IIHR (0.39B) is initially used for the small initial roll angle case, however, the damped frequency ( $\omega_d$ ) shows -10.1 E%D, which is large. Therefore,  $k_{xx}$  is increased by 11% (0.43B) based on the roll natural frequency  $\omega_\phi = \sqrt{\Delta\overline{GM}_T/(I_{xx} + A_{44})}$ , which is obtained from the time history of the roll decay simulation:

$$(I_{xx} + A_{44})\ddot{\phi} + A_\phi\dot{\phi} + B_\phi|\dot{\phi}|\dot{\phi} + C_\phi\dot{\phi}^3 + \Delta\overline{GM}\phi = 0 \quad (6)$$

$$\ddot{\phi} + \alpha_\phi\dot{\phi} + \beta_\phi|\dot{\phi}|\dot{\phi} + \gamma_\phi\dot{\phi}^3 + \omega_{n,\phi}^2\phi = 0 \quad (7)$$

where  $I_{xx}$  is the second moment of inertia in x-direction,  $A_{44}$  is the added mass for roll motion,  $A_\phi$  and  $\alpha_\phi$  are linear roll damping coefficients,  $B_\phi$  and  $\beta_\phi$  are quadratic roll damping coefficients,  $C_\phi$  and  $\gamma_\phi$  are cubic roll damping coefficients and  $\overline{GM}_T$  is the transverse metacentric height. When the adjusted  $k_{xx}$ , is used, the E%D for the damped frequency decreases to -0.5. As a next step, the adjusted  $k_{xx}$  is used for the large initial roll angle case, however, the damped frequency still shows discrepancies for G2 and G3 by showing 4.2 E%D in average. The  $k_{xx}$  is adjusted one more time since small initial roll angle case is regarded to be affected by the damping due to smaller restoring force. The  $k_{xx}$  adjusted twice (0.447B) shows better agreement on damped frequency for large initial roll angle case by having -0.8 and -0.1 E%D for G2 and G3, respectively.

### **Logarithmic decrement**

To estimate the linear roll damping coefficient, the logarithmic method is used as well as the Himeno method (Himeno, 1981). The logarithmic method regards the ratio of the damped roll as the power term of the natural exponential function and calculate the logarithmic decrement ( $\delta_{log}$ ). Then, the linear roll damping coefficient for the logarithmic method ( $\alpha_{\phi,log}$ ) is calculated

by  $\alpha_{\phi,log} = \delta_{log} \cdot f_d$ . Herein, the series of  $\delta_{log}$  are calculated from consecutive minima or maxima in the time history of roll, averaged and then reported.

### Himeno method

To estimate both the linear and the non-linear roll damping coefficients, the Himeno method is used. The method assumes the energy done by the restoring force contributes to roll damping. The theory performs integration by half of roll period respect to the roll angle for the 1D ordinary differential equation roll equation. During the integration, the  $\ddot{\phi}$  term becomes zero and approximations are assumed for the damping terms. The outcome from the integration is expressed as the roll extinction curve:

$$\Delta\phi = a\phi'_n + b\phi_n'^2 + c\phi_n'^3 \quad (8)$$

where  $\phi'_n = (\phi_n + \phi_{n+1})/2$ ,  $a = \frac{1}{4}T_\phi\alpha_{\phi,him}$ ,  $b = \frac{4}{3}\beta_{\phi,him}$  and  $c = \frac{3}{4}\pi^2\gamma_{\phi,him}/T_\phi$ . In current study, the data is fitted by the least square method and only finds the damping coefficients for  $\phi'_n$  and  $\phi_n'^3$  terms. The calculated extinction curves are shown at Figure 5-4. The equivalent linear roll damping ( $\alpha_e$ ) is approximated by:

$$\alpha_e = \alpha_\phi + \frac{8}{3\pi}\omega\phi_i\beta_\phi + \frac{3}{4}\omega^2\phi_i^2\gamma_\phi \quad (9)$$

### Validation

$E\%D$  for  $\delta_{log}$  and  $\alpha_{\phi,log}$  improves clearly once the larger initial roll angle is imposed (from >35.9% to <12%  $E\%D$ ), which tells the importance of having enough restoring force to minimize the non-linear damping effect when logarithmic method is being used. Himeno method is only used for the large initial roll angle case. For  $\alpha_{\phi,him}$ , the agreement is satisfactory (<17.8

$E\%D$  at maximum), but  $E\%D$  is higher for G2 when the  $k_{xx} = 0.43B$ , while  $E\%D$  is higher for G3 when  $k_{xx} = 0.447B$ , which makes it hard to find the trend. However, considering that the latter case predicts the closer damped frequency to IIHR, it seems G2 is able to predict the  $\alpha_{\phi,him}$  better than G3. The  $E\%D$  for  $\gamma_{\phi,him}$  value is generally large (<46.7  $E\%D$ ), but the trend is clear: G2 predicts better than G3 by near 8% difference. The values of  $\alpha_e$  themselves are not close to  $\alpha_{\phi,log}$ , but about 2.5 times larger. The  $E\%D$  for  $\alpha_e$  is a little higher (<24  $E\%D$ ) than the  $E\%D$  for  $\alpha_{\phi,him}$  and the effect of grid resolution for the  $E\%D$  is very small (<1%). When the damped roll amplitudes ( $\phi_m$ ) are simply averaged during 6.5 cycles, the absolute  $E\%D$  is <11%, and the effect of grid resolution is also very small (<1.5%). The overall performance is better for G2 when the absolute averaged  $E\%D$  is sought.

Table 5-1. Validation results for the hydrostatic setup

Symbol	IIHR	CFD	E%D
$T/L$	0.046963	0.046956	0.01
$\nabla/L^3$	0.00427	0.00428	-0.04
$A_w/L^2$	0.1802	0.1805	-0.21
$LCG/L$	0.4852	0.4848	0.007
$T_z/(L/U)$	0.455 (2.20)	0.463 (2.16)	-1.7
$T_\theta/(L/U)$	0.455 (2.20)	0.450 (2.22)	1.1
$T_\phi/(L/U)$	1.958 (0.51)	1.946 (0.51)	-0.8
$GM/L$	0.00259	0.00253	2.42
$k_{xx}/B$	0.39	0.447	-14.62
$k_{yy}/L$	0.25	0.25	
$k_{zz}/L$	0.25	0.25	

Table 5-2. Validation results for the heave decay test

Var.	Cycle	Empirical solution	S		E%Empirical	
			G3		G3	
			Initial $z/L = 0.02$	Initial $z/L = 0.047$	Initial $z/L = 0.02$	Initial $z/L = 0.047$
$T_d * U/L$	1	0.455	0.463	0.463	-1.7	-1.7
	1.5		0.452	0.439	0.6	3.4
	2		0.411		9.7	
	2.5		0.395		13.1	
	3		0.400		12.0	

Table 5-3. Validation results for the pitch decay test

Var.	Cycle	Empirical solution	S		E%Empirical	
			G3 Initial $\theta=5^\circ$		G3 Initial $\theta=5^\circ$	
$T_d * U/L$	1	0.455	0.450		1.1	
	1.5		0.458		-0.6	
	2		0.403		11.4	

Table 5-4. Validation results for the roll decay test

	D		S					(D-S)%D						
	IIHR		G2			G3		G2			G3			
Initial $\phi$	8.92°	20.16°	8.92°		20.16°			8.92°		20.16°				
$k_{xx}/B$	0.39	0.39	0.39	0.43	0.43	0.447	0.43	0.447	0.39	0.43	0.43	0.447	0.43	0.447
$\omega_d$ [1/s]	1.572	1.59	1.734	1.581	1.65	1.60	1.67	1.59	-10.1	-0.5	-3.4	-0.8	-4.9	-0.1
$\delta_{log}$	0.129	0.1041	0.073	0.067	0.1052	0.0916	0.1098	0.0972	42.0	47.8	-1.1	12.0		6.6
$\alpha_{\phi,log}$ [1/s]	0.032	0.026	0.020	0.017	0.028	0.023	0.029	0.025	35.9	47.5	-4.7	11.1		6.4
$\alpha_{\phi,him}$ [1/s]		0.029			0.033	0.027	0.031	0.034			-15.0	4.8	-9.1	-17.8
$\gamma_{\phi,him}$ [s]		1.32e-4			9.8e-5	8.6e-5	8.8e-5	7.0e-5			25.6	35.1	33.7	46.7
$\alpha_e$ [1/s]		0.078			0.070	0.059	0.064	0.060			10.8	24.0	18.0	23.1
$\phi_m$ [deg]	7.4	13.7	8.3	8.1	14.6	15.2	17.1	15.0	-5.2	-9.0	-6.5	-11.0		-9.6
No. cycle		6.5			6.5	6.5	3.5	6.5						
Ave. <sup>(1)</sup>									23.3	26.2	6.9	10.6	10.7	10.6

<sup>(1)</sup> error for  $\gamma$  is excluded

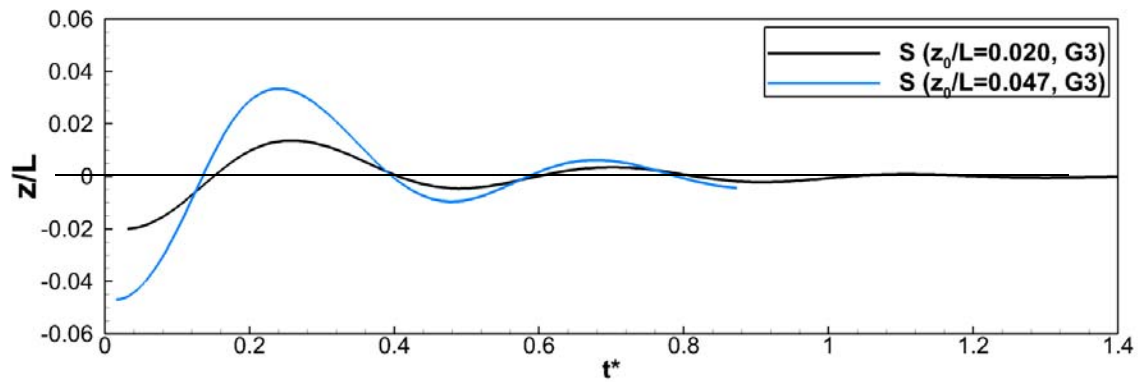


Figure 5-1. Time-histories from the heave decay tests: initial  $z/L = 0.02$  and  $0.047$

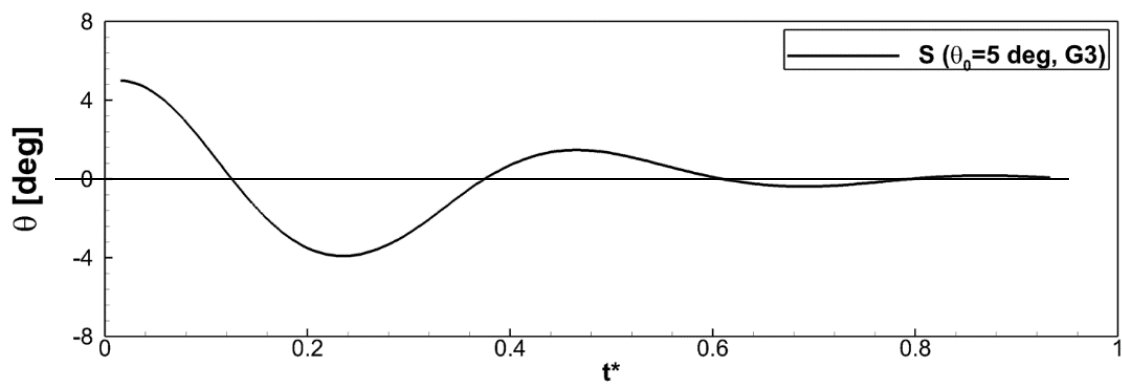


Figure 5-2. Time-history from the pitch decay test: initial  $\theta = 5^\circ$

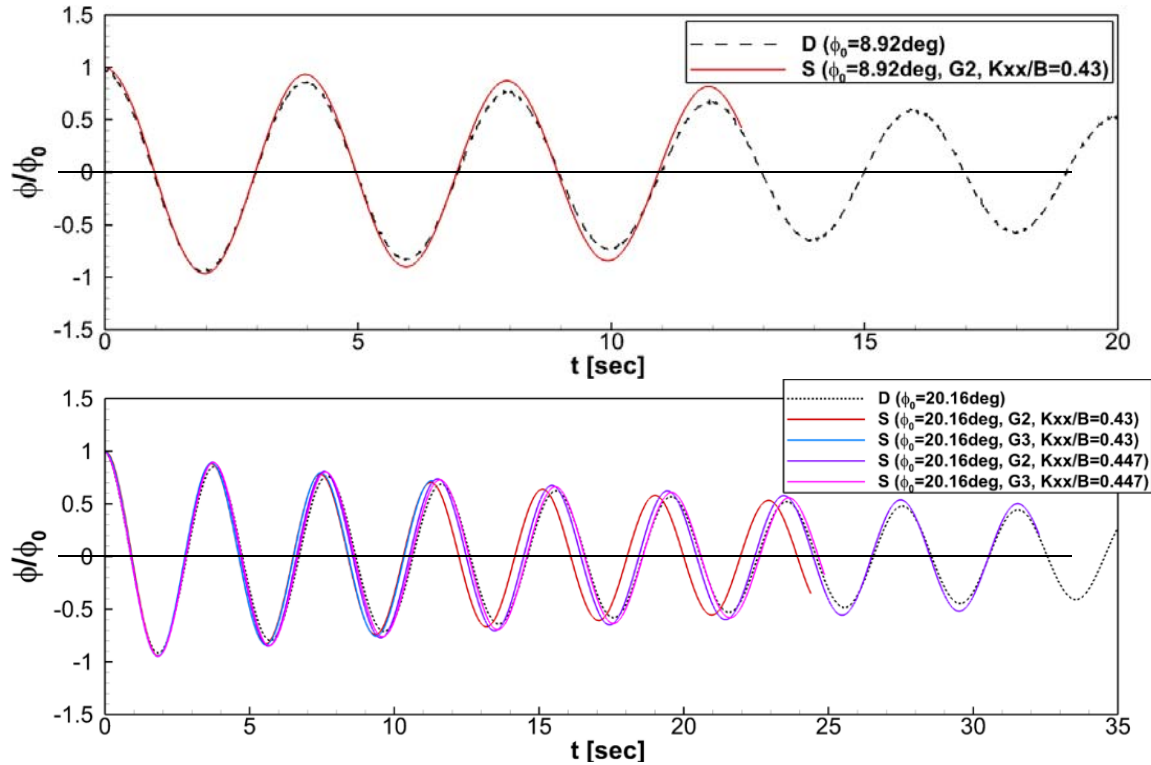


Figure 5-3. Time histories from the roll decay test: (a) initial  $\phi = 8.92^\circ$ , (b) initial  $\phi = 20.16^\circ$

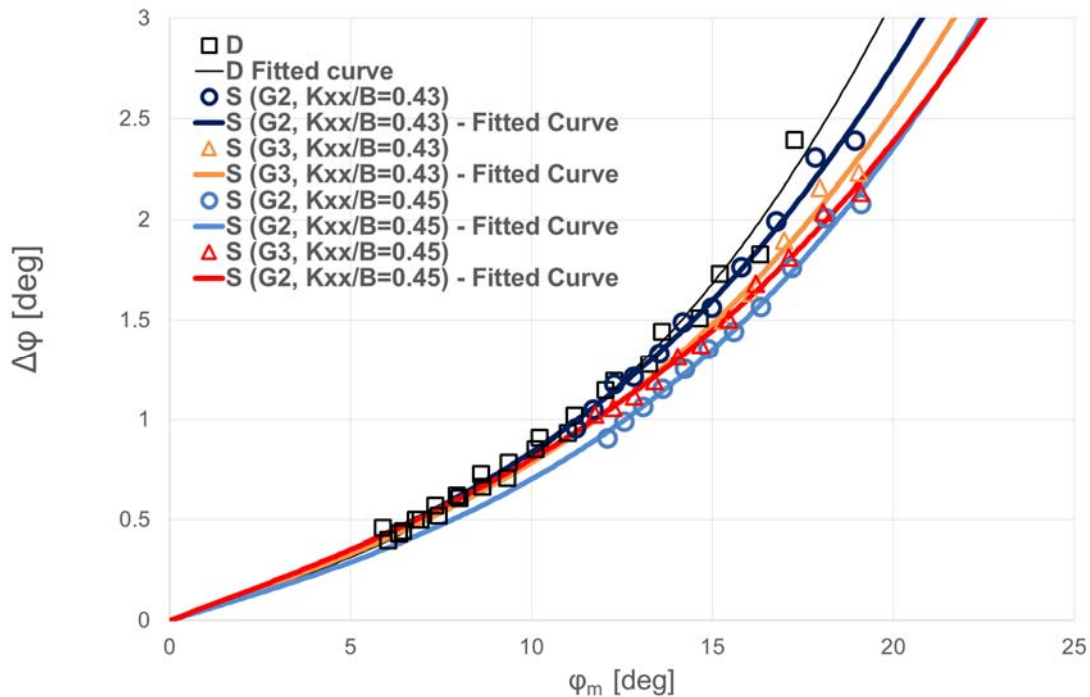


Figure 5-4. Roll extinction curve (initial  $\phi = 20.16$  deg)

## 6. RESISTANCE TEST

### 6.1. Verification

Table 6-1 shows the grid resolution study results for motions, resistance and the nominal wake fraction coefficient in the resistance test. The time-histories of motions and resistance show oscillations after the variables reaches the steady state as shown in Figure 6-1, therefore, the mean values are taken.

#### Motions

The sinkage shows OC and the trim shows oscillatory divergence (OD). Like the POT, the  $U_I\%S_1$  is larger than  $\varepsilon_{21}\%S_1$ , which makes it hard to assess the grid convergence.

#### Resistance

The friction, residual and total resistance shows OC, monotonic divergence (MD) and OD, respectively.  $U_I\%S_1$  for the frictional resistance is about 4 times smaller than  $\varepsilon_{21}\%S_1$ , however, the residual and total resistances still show large  $U_I\%S_1$  along with motions.

#### Nominal wake

The nominal wake fraction coefficient, which is the mean of axial velocity distribution at V1 shows MC. The change of the nominal wake respect to the grid resolution can be visually seen in Figure 6-4 to 6. The relative percentage difference of the  $1 - \omega$  is 1.3% between G1 and G3.

#### Discussion

The  $U_G\%S_1$  estimation is only available for the residual resistance that shows MD (2.5%). The overall  $U_{SN}\%D$  is large (15.2% for motions and 21.2% for forces) due to  $U_I\%S_1$ . The larger domain size is enlarged and the same test is run to check if the reflected wave is the source of the

large  $U_l\%S_1$  since the residual resistance, which is more affected by the pressure change, shows larger  $U_l\%S_1$ , however, the domain size was not the source.

## 6.2. Validation

Table 6-2 shows the validation results of motions and resistances. CFD is validated against both IIHR and FORCE, which are from T2015 submission, and is also compared with other two CFD results (IIHR and FORCE scale KCS) both submitted to T2015 by Sadat-Hosseini et al. (2015).

### Motions

The averaged  $E\%D$  of sinkage is less against IIHR than FORCE by 16% for the grid triplets and shows similar performance as Sadat-Hosseini et al. (2015). As grid becomes finer, the data show improvements for the sinkage. The averaged  $E\%D$  (over grid triplet) of trim is much less against FORCE than IIHR (35% closer to experiment). Compared to Sadat-Hosseini et al. (2015), current result shows 4.3 less (at maximum)  $E\%D$  by having smaller trim angle, which indicates that the current grid produces less of pitch moment. The  $E\%D$  for G1 is greater than G3 for trim, which is not desirable.

### Resistance

The frictional and total resistances are predicted well ( $<3\% E\%D$ ) for the grid triplets while the residual resistance shows some discrepancy ( $9\% E\%D$ ) against IIHR. The frictional resistance for IIHR is obtained from ITTC frictional curve proposed in 1957. The residual resistance shows fairly good agreement against FORCE too ( $7\% E\%D$  in average) and the current CFD predicts the residual resistance better than Sadat-Hosseini et al. (2015).

### **6.3. Longitudinal Distribution of the Resistance**

#### **Objective and methodology**

Figure 6-2 shows the longitudinal distribution of the resistance induced by the hydrodynamic pressure on the hull. By plotting the resistance longitudinally, more localized information of the integral value is obtained. The current data from the resistance test will be compared with the self-propulsion test results to see the difference of the resistance distribution when the propeller is active in the next chapter. For this specific figure (for the later chapters as well), the x-directional sign is opposite (+x towards the aft which produces positive resistance) from the coordinate system that is commonly used in this study. 74 sections are equally distributed longitudinally, and only the hydrodynamic pressure is integrated at each section due to following reasons: frictional resistance does not show significant changes along the longitudinal direction; gravitational resistance is the point value imposed at the center of gravity, therefore, plotting the distribution of the gravitational resistance is impossible unless the weight distribution on the hull is designed during the modelling; hydrostatic resistance itself usually has higher order than the frictional or hydrodynamic resistances and it is mostly cancelled by the gravitational resistance, therefore, the value becomes meaningful mostly when the gravitational resistance is subtracted, which is not possible in the current study. The gravitational resistance is designed, again, as a point value.

#### **Discussion**

The hydrodynamic resistance is the highest at the bulbous bow due to the stagnation, drops right away as the flow passes the bulbous bow (due to acceleration), and recovers until  $x/L = 0.08$  (from FP) where the tangent line starts emerge below the waterline. Then the resistance drops again until  $x/L = 0.2$  (from FP), which is almost the start of the mid-section. As the flow passes

the mid-section, the resistance gradually goes up until  $x/L = 0.8$  (from FP) where the mid-section almost ends. From  $x/L = 0.8$  (from FP) to the transom, the resistance drops and recovers a little after the propeller plane.

### **Source of the resistance**

When the distribution is integrated locally, the bow part ( $x/L = 0.0$  to 0.2 from FP) contributes for most of the positive hydrodynamic resistance, the mid-section ( $x/L = 0.2$  to 0.8 from FP) contributes to the resistance with 6 times smaller negative value compared to the bow part and the stern part ( $x/L = 0.8$  to 1.0 from FP) contributes with 3.4 times smaller negative values compared to the bow part. Most importantly, the positive resistance comes from the bow part in the calm water. Figure 6-3 graphically shows the pressure distribution near the stern.

## **6.4. Local Flow**

### **Vertical sections and nominal wake**

As already mentioned previously, Figures 6-4 to 6 include the nominal wake distribution at V1 for grid triplets and also include the velocity distributions at the other vertical sections (V2 to 4). The boundary layer becomes narrower as grid is refined. The range of the axial velocity distribution is vast (from  $u/U = 0.2 - 1.0$ ) due to the thick boundary layer.

### **Horizontal sections**

Figure 6-6 shows the distribution of the axial velocities at horizontal sections (H1 to 4) for G3. The distribution is confirmed to be almost symmetric and streamlined, and its data will be compared to the case involves the propeller, i.e. self-propulsion test, in the later chapter.

Table 6-1. Verification results for the resistance test

	U <sub>I</sub> %S <sub>1</sub>	ε <sub>21</sub> %S <sub>1</sub>	ε <sub>32</sub> %S <sub>1</sub>	R	Conv	P	U <sub>G</sub> %S <sub>1</sub>	U <sub>SN</sub> %D
<b>Motion</b>								
σ/L × 10 <sup>2</sup>	9.96	-1.06	2.66	-0.40	OC		9.96	
τ [deg]	20.52	-4.05	2.31	-1.75	OD		20.52	
Ave.	15.24						15.24	
<b>Force</b>								
C <sub>F</sub> × 10 <sup>3</sup>	0.27	0.76	-1.58	-0.48	OC		0.27	
C <sub>R</sub> × 10 <sup>3</sup>	53.02	13.96	1.49	9.38	MD	-1.62	2.52	53.08
C <sub>T</sub> × 10 <sup>3</sup>	10.25	3.27	-0.97	-3.39	OD			10.25
Ave.	21.18							21.20
Local flow (direct measurement)								
1 - ω		0.65	0.65	1.00	MC	0.00		

Table 6-2. Validation results for the resistance test

Var.	D		S				E%D (D = IIHR)				E%D (D = FORCE)					
							2.7	6.1	2.7	6.1	2.7	6.1	2.7	6.1		
L [m]	2.7	6.1														
Facility/Grid	IIHR	FORCE	G1	G2	G3	T2015	T2015	G1	G2	G3	T2015	G1	G2	G3	T2015	T2015
<b>Motion</b>																
σ/L × 10 <sup>2</sup>	0.176	0.207	0.188	0.186	0.191	0.187	0.188	-6.6	-5.5	-8.5	-6.2	9.5	10.4	7.8	9.8	9.4
τ [deg]	-0.122	-0.165	-0.173	-0.166	-0.170	-0.181	-0.180	-41.5	-35.2	-39.2	-47.8	-5.3	-0.6	-3.5	-10.0	-9.4
Ave.								24.0	20.4	23.8	27.0	<b>7.4</b>	<b>5.5</b>	<b>5.7</b>	<b>9.9</b>	<b>9.4</b>
<b>Force</b>																
C <sub>F</sub> × 10 <sup>3</sup>	-3.610	-2.900	-3.682	-3.710	-3.652	-3.710	-3.050	-2.0	-2.8	-1.1	-2.8				-5.2	
C <sub>R</sub> × 10 <sup>3</sup>	-1.054	-0.935	-0.874	-0.996	-1.009	-0.802	-0.795	17.1	5.5	4.2	23.9	6.5	-6.5	-7.9	14.2	15.0
C <sub>T</sub> × 10 <sup>3</sup>	-4.664	-3.835	-4.556	-4.705	-4.661	-4.512	-3.845	2.3	-0.9	0.1	3.3	<b>7.1</b>	<b>3.1</b>	<b>1.8</b>	<b>10.0</b>	-0.3
Ave.												6.5	6.5	7.9	14.2	<b>6.8</b>
Local flow (direct measurement)																
1 - ω			0.613	0.617	0.621											

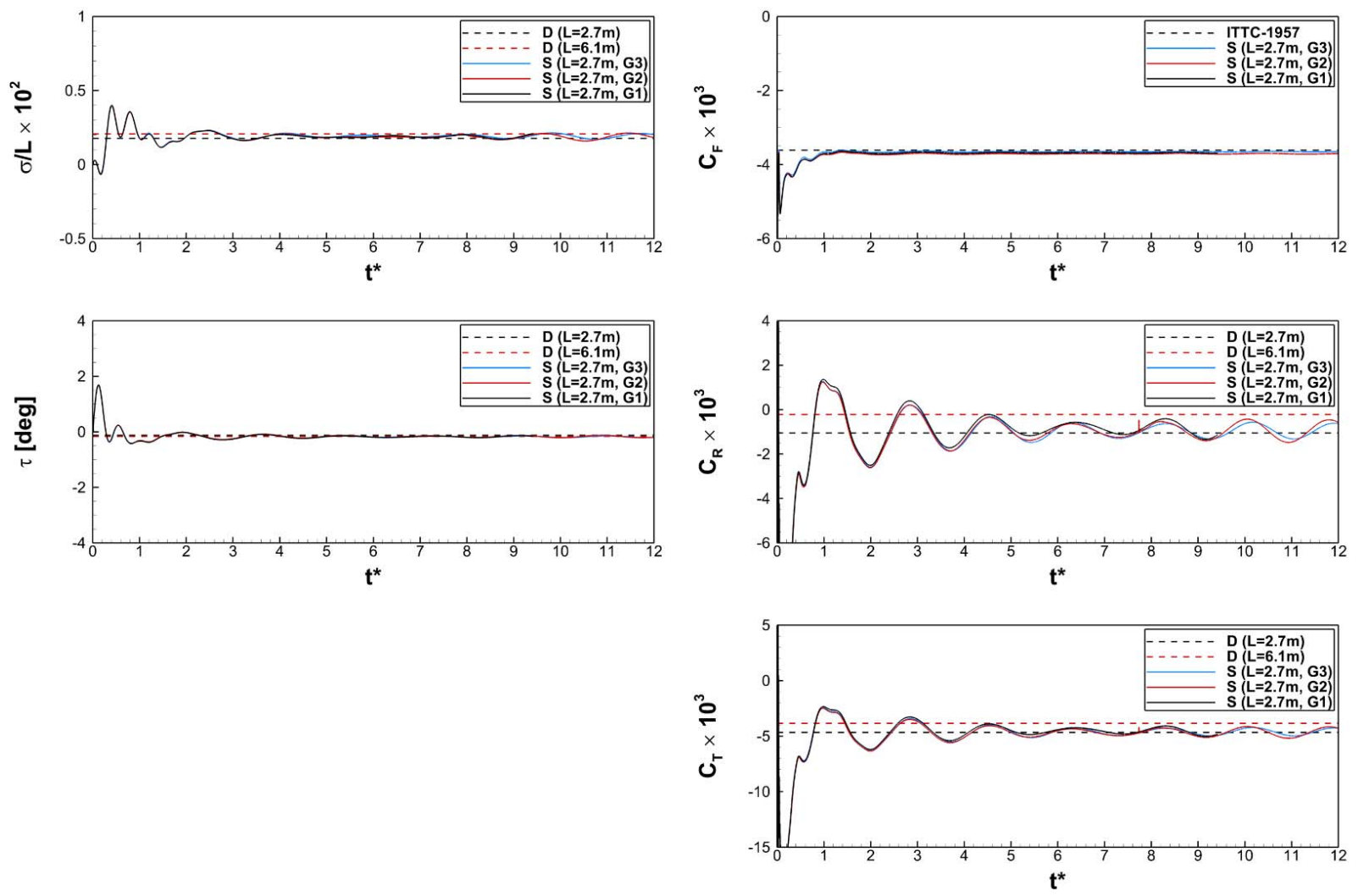


Figure 6-1. Time-histories from the resistance test

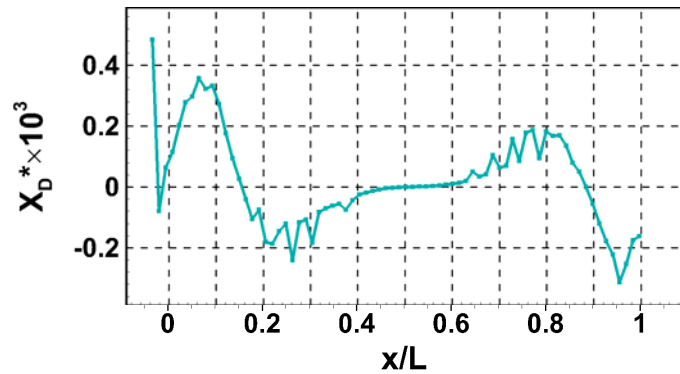


Figure 6-2. Longitudinal distribution of the hydrodynamic x-force on the hull

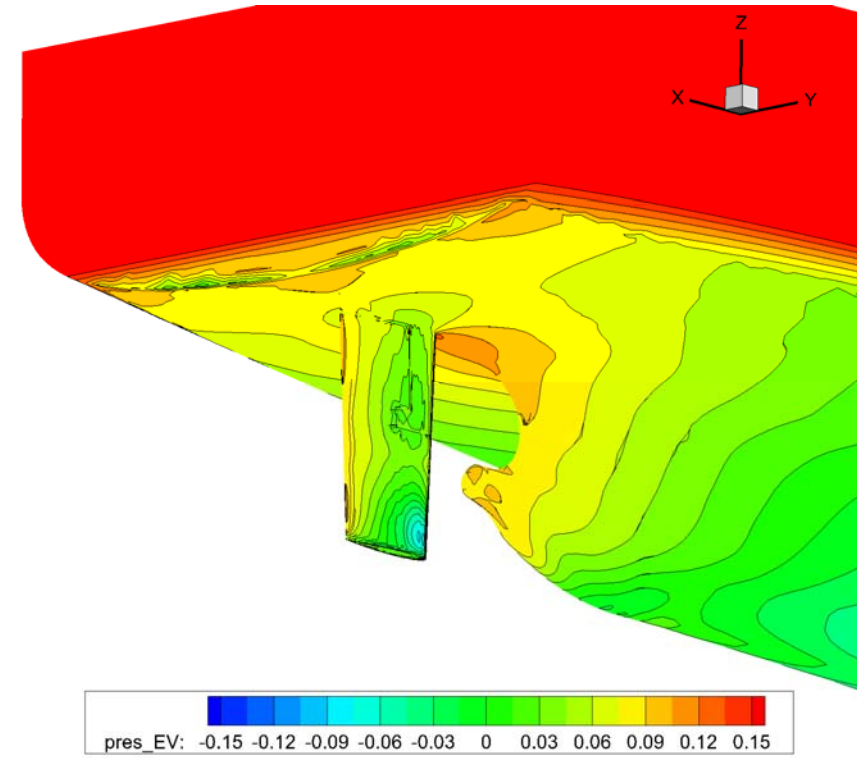


Figure 6-3. Distribution of the hydrodynamic pressure near the stern region

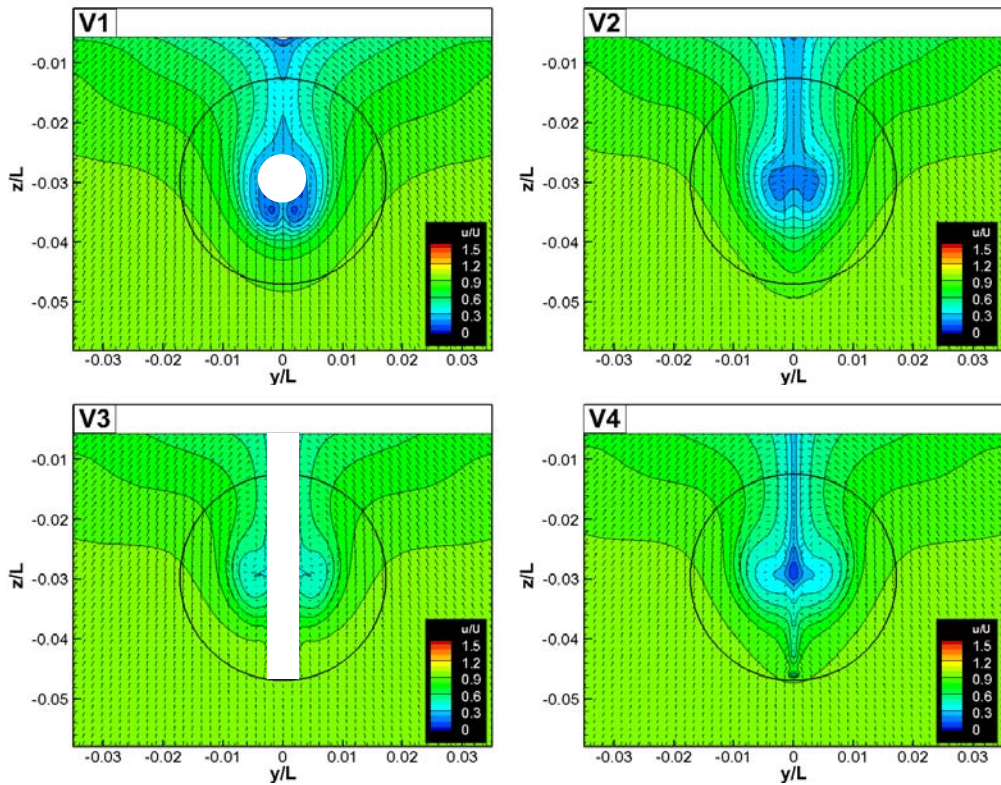


Figure 6-4. x-vel. contours and y,z-vel. vectors at vertical sections (G1)

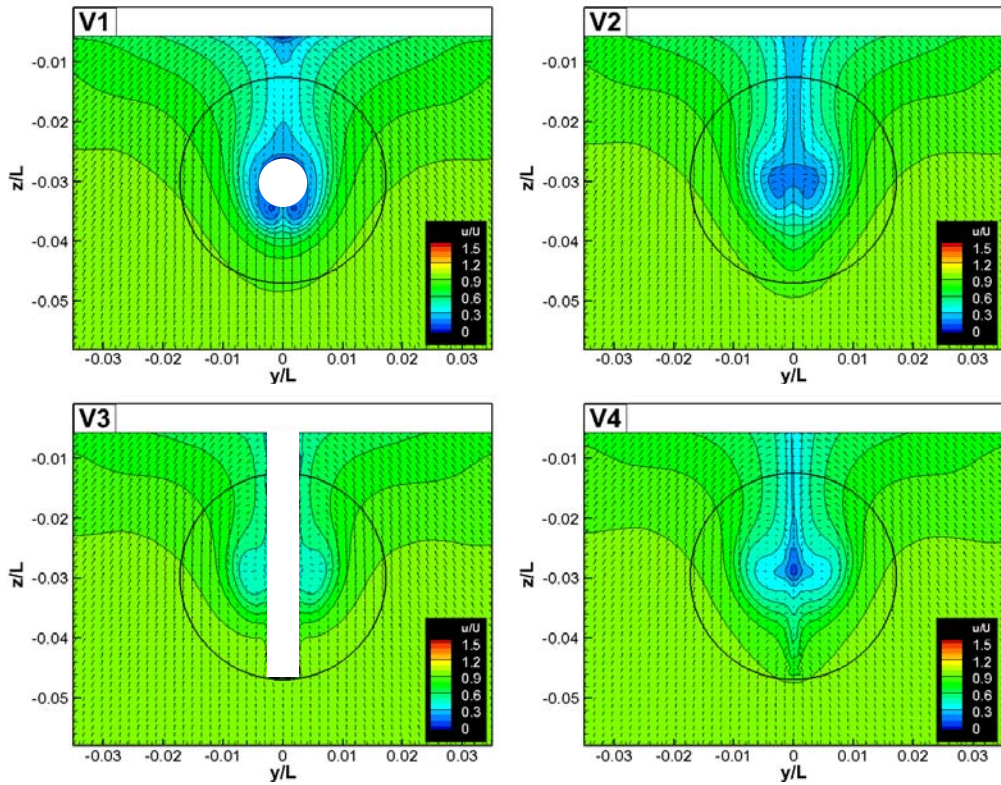


Figure 6-5. x-vel. contours and y,z-vel. vectors at vertical sections (G2)

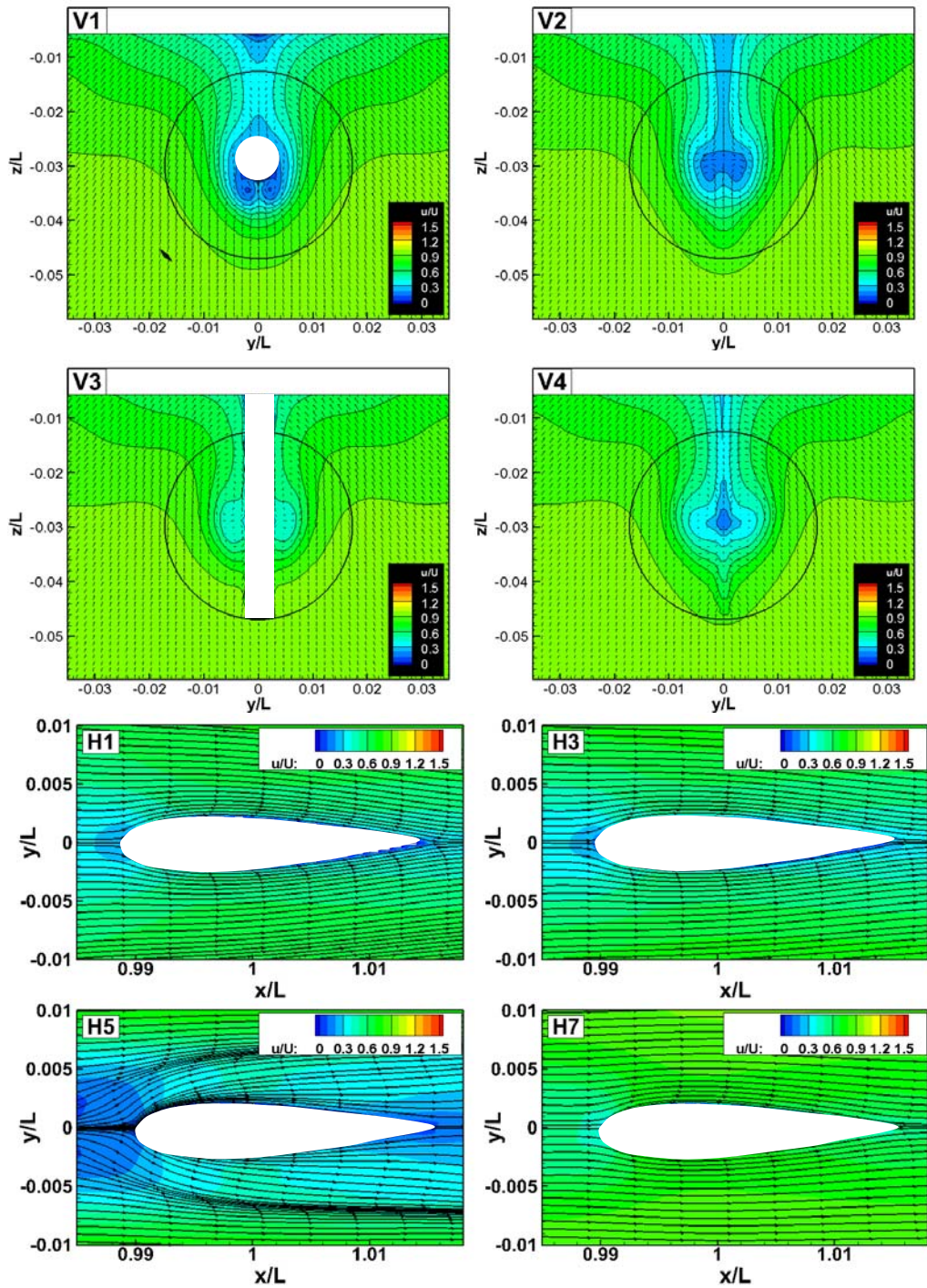


Figure 6-6. x-vel. contours and y,z-vel. vectors at V&H sections (G3)

## 7. CALM WATER SELF-PROPELLION TEST

### 7.1. Validation

Table 7-1 shows the validation result of motions, forces, PID controlled variables and self-propulsion factors in the calm water self-propulsion test. Grid triplets are assessed for AP model, however, the usage of G1 is refrained for BF model since the BF model does not produce asymmetrical propeller wake, and thereby, the test results do not show much difference against the resistance test. For the validation section, mean value of each variable is taken from the time-history (Figure 7-1). The hydrodynamic forces on both bare-hull and appendages are calculated and used when explaining the characteristics of force/moment balance during the self-propulsion test, and are presented in Table 7-2.

#### Motions

The prediction accuracy for heave is reasonable for both BF and AP models. BF model shows <4.5% and AP model shows <10%  $E\%D$ . BF model shows less  $E\%D$  than AP model for heave by 5.5% and 2.3% differences for G2 and G3, respectively. The source of the difference between the BF and AP is expected to come from the different pressure distribution around the stern region caused by using different propulsion models and is also expected to cause by the difference of pitch angle, which is strongly coupled with heave. The pitch angle is small (less than 0.16°), however, AP and BF shows notable differences: BF shows -31.8% and -42.9%  $E\%D$  and AP shows -57.4% and -76.4%  $E\%D$  for G2 and G3, respectively. AP model additionally shows -60.8%  $E\%D$  for G1. The propeller vertical force does not exist for BF model, however, the AP model shows 3 times bigger amount than lateral force, and the force is pointing upward (see Table 7-2 and 7-3), which seem to have contributed for the additional pitch moment. Since the test is the free-running with a single screwed ship, the roll angle is also evaluated. Both measured and

computed roll angles are very small (less than 1°). Still, AP shows better agreement by predicting the same negative roll (leaning to portside) as IIHR.

### Force and moment

The propeller thrust coefficient is predicted reasonably for AP model. BF model predicts the dimensional thrust value accurately, however, calculating thrust coefficient value is affected by the over-predicted propeller rotational speed, which will be discussed in the following section. BF model under-predicts the thrust coefficient with 24.5% and 31.0%  $E\%D$  for G2 and G3, and AP model over-predicts with -4.5%, -4.9% and -4.5%  $E\%D$  for G1, G2 and G3, respectively. The propeller torque coefficient agreement is off from IIHR for both BF and AP models by 13.2% and -9% difference in average. BF model under-predicts with 15.1% and 11.3%  $E\%D$  and AP model over-predicts with -10.3%, -7.8%  $E\%D$  for G2 and G3, respectively. During the postprocess, the torque calculation requires the moment arm that is the relative displacement between the propeller grid point and the propeller axis for the current validation against IIHR. Therefore, the solution files from the computation, which are calculating the moment arms to be the relative distances between the center of gravity of the ship and the propeller grid points, are read and the moment arms are adjusted. As explained from Sanada et al. (2018), the torque measurement in the experiment is performed after calibrating the idle friction, however, the reason of current discrepancy of torque for AP model is not clear and more investigation is required for both CFD and experiment. The non-dimensional thrust ( $t'$ ) and the non-dimensional torque ( $q'$ ) are also evaluated as discussed in Sanada et al. (2018). The agreement of the non-dimensional thrust is reasonable by showing 4.3% and 1.7%  $E\%D$  in average for BF and AP models respectively, however, the agreement for the non-dimensional torque is much close for AP than BF, which are showing 2.4% and 51%  $E\%D$  in average, respectively.

## PID controlled variables

The ship speed is obtained by adjusting the propeller rotational speed with the PID controller. Both BF and AP models find the target speed precisely (less than 0.3%  $E\%D$ ), which confirms the validity of the current PID approach. The agreement for the propeller rotational speed is satisfactory only for AP model (less than 4.4%  $E\%D$ ), and it shows clear difference between the two models. The BF model fails to predict the propeller revolution rate when the incoming flow of the propeller is far from the uniform flow (effective wake fraction becomes smaller) since BF model calculates the thrust coefficient and torque coefficient based on the speed of the ship, not based on the propeller inflow velocity. Once the BF model is adjusted by simply imposing the effective wake fraction inside the velocity calculation routine, the  $E\%D$  of the thrust coefficient and the propeller rotational speed are predicted almost at the same level as AP (about 5%  $E\%D$ ). The effective wake fraction used during adjustment is obtained by averaging the axial velocity inside the propeller diameter located at V1 slice in G3-AP flow field. The neutral rudder angle is found to be small and it changes upon grid resolution for AP model. The neutral rudder angle for BF model is negligible. For AP model, the neutral rudder angle is found to become smaller as grid gets refined. G1 shows 16%  $E\%D$  while G2 and G3 show almost none and -102.7%  $E\%D$ .

## Self-propulsion factors

Self-propulsion factors from the computations are estimated in two different ways: using thrust identification method as used by Sanada et al. (2018); or the direct calculation from the flow field. Thrust identification method is firstly used as an alternative for the experiment (IIHR) since the measurement of the effective wake is hard to get, while in CFD, the solutions account for integer number of propeller rotation cycles are averaged and the effective wake could be estimated.

The AP model gives out reasonable and consistent validity over grid triplets when the thrust identification method is used, as expected:  $E\%D$  for advance coefficient, advance coefficient at the propeller inflow ( $J_B$ ),  $1 - \omega_e$ , propeller efficiency behind the ship ( $\eta_0$ ) and relative rotative efficiency ( $\eta_R$ ) are 5.4%, -3.3%, 8.2%, 2.0% and 5.1% in average. BF model, however, shows much larger discrepancies mostly due to over-predicting the propeller rotational speed. The comparison between the thrust identification and the direct measurement reveals that the advance coefficient at the propeller inflow and the  $1 - \omega_e$  are different by almost 17% and 14%. which indicates the invalidity of using thrust identification for the ship that involves the thick boundary layer near the propeller inflow. Still, the propeller efficiency values are close with each other by showing 1% difference.

## 7.2. Propeller-Hull-Rudder Interaction

The investigation on the Propeller-Hull-Rudder interaction could be achieved by performing simulations with different grid setups and by directly comparing solutions. Current grid system can detach the rudder or propeller from the fully assembled model, and the process does not undergo a significant grid change especially for the surface grid and the grid near to the surface. As the grids are detached, the volume grids that fills the fluid part among volume grids are often subjected to change.

### 7.2.1. Effect of the Propeller

Resistance test and self-propulsion test are compared to check the effect of the propeller (rudder exists for both case).

### **Bare-hull**

To check the point where causes the thrust deduction, the longitudinal mean hydrodynamic pressure resistance distribution is plotted in Figure 7-2 (first row). For the self-propulsion test, the BH's mean hydrodynamic pressure shows less drop after  $x/L = 0.8$  (from FP) compared to the resistance due to the existence of the propeller and the pressure disturbance that the propeller produce. The SD of pressure (shown as the error bar) indicates that the amount of hydrodynamic pressure fluctuation is not negligible, and thereby, affects the thrust deduction to oscillate. The mean and standard deviation of hydrodynamic pressure distribution near the stern region are graphically shown in Figure 7-3 and 7-4, respectively.

### **Rudder**

The rudder in self-propulsion test experiences totally different inflow due to the propeller wake from the resistance test. Under the self-propulsion condition, both resistance and the side force increase noticeably (Table 7-2). The side force becomes positive (points starboard) due to the propeller wake. The rudder also experiences pressure fluctuation, also due to the propeller wake, as shown in Figure 7-4.

### **Propeller inflow**

Due to the existence of the propeller, the propeller inflow is intensified for both axial and lateral velocities due to the propeller suction (V1 in Figure 7-5) compared to the nominal wake. The effective wake fraction coefficient is calculated in the same way as nominal wake fraction coefficient is obtained, i.e. averaged during sufficient time duration at V1. The  $1 - \omega_e$  is 18% higher (Table 7-1) than the  $1 - \omega$ . The distribution of the lateral flow shows the gathering of the flow towards the propeller center affecting the distribution of the axial velocity to become asymmetric.

### **Propeller wake – in vertical sections**

In Figure 7-5, once the effective wake (V1) passes the propeller, the axial and lateral velocities become higher/lower at the starboard (V2) than the portside, in average. The lateral velocity vectors seem intensified at the portside than the starboard since the lateral velocities of the effective wake (V1) coincide with the direction of the propeller rotation. The AoA of the propeller blade is expected to be less at the portside than the one at the starboard due to the same reason and is supported by the time history of the thrust of a single blade as shown in Figure 7-6: the less thrust is produced by the blade passing the portside than the blade passing the starboard, which brought less flow acceleration at the portside. Similarly, the lateral force of the single blade shows slight opposite trend from the thrust: the maximum positive occurs when the blade is right before the “C” from the figure 7-6 and the minimum negative occurs right before the “A”, but with larger magnitude. The vertical force shows maximum positive at around “D” and minimum negative right after “B”. As the flow passes the rudder, the flow is blocked by the rudder surface and the flows on both starboard and portside seem to start developing separately (V3). During this stage, the flow on the portside starts to shift upward due to including much of vertical vectors pointing upward while the flow on the starboard shifts downward, vice versa, but with less amount than the portside due to the aforementioned reason. Also, the circulation at the top right of the starboard side starts to appear. And finally, the flow passed the rudder becomes asymmetrical distribution as shown in V4 without being much mixed after the flow merges. Since the mean axial velocity is higher at the starboard, the rudder surface at the portside performs like a pressure side, consequently, and thus generates the side force (lift) pointing the starboard which exerts negative yaw moment at  $\delta = 0$  condition (PID controlled rudder case will be discussed later).

### **Propeller wake – in horizontal sections**

H1-4 in Figure 7-5 show axial velocity distributions and streamlines horizontally. H1 is close to the top region where the propeller sweeps. Due to the intensified lateral velocity on the portside, the stagnation point exist at the portside of the rudder, which exerts lift force to the starboard. H1 does not clearly indicate that the portside of the rudder is the pressure side since the magnitude of the axial velocity is shown larger on the portside of the rudder. The flow at H1 seems disturbed by the outer flow since H1 is close to the propeller perimeter. H2, however, clearly shows the flow explained in the previous section. H3 is located right at the hub and does not show distinct AoA on the rudder. H4, which is located at the lower part of the rudder, has negative AoA due to the lateral velocity pointing portside (see V2). The pressure side is the starboard, and lift force points the portside.

#### **7.2.2. Effect of the Rudder**

Two difference self-propulsion tests (with and without rudder) are performed and compared instead of the resistance test since the rudder effect is considered to be more prominent when the propeller exists.

##### **Bare-hull**

The existence of the rudder decreases the BH resistance by 1~1.2%, which is not considered as significant amount (Table 7-2). Figure 7-2 shows that the pressure distribution on the hull is almost identical up to  $x/L = 0.975$  (from FP) where the propeller locates, but the existence of rudder alleviates the high pressure right on top of the propeller, which eventually lowers the pressure at the stern, and produces lower resistance.

### **Propeller inflow**

The  $1 - \omega_e$  (from V1 at Figure 7-6) is about 3.8% higher (0.815) when the rudder is not at present. Currently, the reason is not clear. However, the existence of rudder tends to perturb the lower pressure field in the propeller wake which lowers the flow acceleration.

### **Propeller**

Table 7-2 shows that the existence of the rudder decreases the propeller side force. Figure 7-6 shows the wake distributions on the slices. Compared to 7-5, the axial velocity magnitude at V2 is much higher at the starboard, which induce the side force pointing to the portside. In Figure 7-3, the mean pressure distribution on the propeller surface shows lower pressure near the hub for the non-rudder case presumably caused by not being blocked by the rudder. The standard deviation of the pressure distribution shows that the fluctuation of the pressure is much higher for the case that has the rudder.

### **Propeller wake**

As mentioned earlier, the propeller wake in Figure 7-6 shows distinct increase of axial velocity on the starboard when the rudder is not at presence and the flow keeps its pattern as it advances (V3 and V4). On horizontal slices, the direction of the lateral velocity is hard to be distinguished from the ones on Figure 7-5 except H3. The H3 for the non-rudder case shows the streamlines heading to portside while the H3 for the rudder at presence case shows straight streamlines.

### **7.3. Neutral Rudder Angle**

#### **$\delta = 0$ condition**

During the self-propulsion test in the calm water using CFD, additional study was conducted using G3-AP to understand more on the neutral rudder angle especially when the AP is active. KCS, the single screw propelled ship, heads to portside when the rudder is fixed ( $\delta = 0$ ) due to the negative total yaw moment acting on the ship as discussed earlier (Table 7-2). The major contribution for this negative yaw moment comes from the “Rudder stock”, exerting nearly 160% of the total yaw moment (additional 60% contribution is being cancelled out by the “Hull”, the “Rudder” and the “Propeller”, which are exerting positive yaw moments. This high yaw moment value arise from the large angle of attack (AoA) at the leading edge of the “Rudder stock” due to the propeller wake (Table 7-4).

#### **PID controlled $\delta$ condition**

When the rudder angle is controlled by PID controller, the contribution of the “Rudder” increases by having the neutral rudder angle and reduces the negative yaw angle, forcing the ship to head straight. Meanwhile, the contribution of the “Rudder stock” increases only by 12%.

#### **Pressure distribution on the rudder**

To verify the analysis using integral value, the dynamic pressure distributions for  $\delta = 0$  and  $\delta$  controlled conditions are visually presented in Figure 7-8 and the difference of the pressure distribution is also presented in Figure 7-9. The angle of attack near the leading edge was found for both “Rudder stock” and “Rudder” in Figure 7-10. In Figure 7-10, the mean dynamic pressure distribution difference between  $\delta = 0$  and  $\delta$  controlled cases (subtracted  $\delta$  controlled case from  $\delta = 0$ ) shows that the “Rudder” exerts significant amount of positive side force (to starboard), and

hence, turn the ship to portside when  $\delta = 0$ , while the side force difference at the “Rudder stock” is relatively small compared to “Rudder”.

### **Angle of attack on the rudder**

Figure 7-10 shows that the AoA at H1 and H2 (at “Rudder stock”) is always larger than  $2.7^\circ$  for both  $\delta = 0$  and  $\delta$  controlled cases while the AoA at H4 (at “Rudder”) diminishes from  $1.5^\circ$  to  $0.2^\circ$  as the PID controlled rudder is used.

## **7.4. Local Flow**

For the verification and validation on the flow field, the flow behind the rudder ( $x/L = 1.025$  from FP, V5 from Figure 2-2) is studied. The study involves grid dependency verification test and the validation against the local flow measurement provided by OU PIV as shown in Figure 7-11. For the grid dependency test, all grid triplets with AP model are assessed. Since the measurement was performed in the carriage coordinate system, the surge-free OU PIV result is considered to have less clearance between the rudder and the point of interest than the CFD due to involving mean surge of the model while CFD always measure at a constant distance from the FP. Still, it is clear that the agreement with the OU PIV becomes closer as grid is refined. The two vortices near the hub is only predicted by G1, while G2 and G3 only shows one on the right. The vortex near the  $(y/L, z/L) = (0.0, 0.045)$  is only predicted by G1 or G2. The vortex near the  $(y/L, z/L) = (0.008, 0.018)$  could be detected by all. The lateral flow magnitude at the upward/portside is much larger than any part of the flow region from OU PIV, and CFD follows the trend qualitatively, however, does not show quantitative agreement even for G1, partially due to the mean surge component in OU experiment. OU’s axis of propeller is located much higher than the CFD. Still, the CFD result looks more reasonable when both sinkage and trim, which are very small, are considered. The Q-criteria during the test using G1-AP is shown at Figure 7-12.

Table 7-1. Validation results for the SP tests

Var.	D	S					E%D				
	IIHR	BF		AP			BF		AP		
		G2	G3	G1	G2	G3	G2	G3	G1	G2	G3
<b>Motion</b>											
$z/L$	0.0022	0.00210	0.00214	0.00201	0.00198	0.00209	4.5	2.7	8.6	10.0	5.0
$\theta [^\circ]$	-0.090	-0.118	-0.128	-0.144	-0.141	-0.158	-31.8	-42.9	-60.8	-57.4	-76.4
$\phi [^\circ]$	-0.12	0.35	0.36	-0.47	-0.59	-0.60	380.4	388.4	-276.6	-372.7	-380.7
Ave. abs							<b>138.9</b>	<b>144.7</b>	<b>115.3</b>	<b>146.7</b>	<b>154.0</b>
<b>Force</b>											
$K_T$	0.245	0.185	0.169	0.256	0.257	0.256	24.5	31.0	-4.5	-4.9	-4.5
$K_Q$	0.0397	0.0337	0.0352		0.0438	0.0428	15.1	11.3		-10.3	-7.8
$t'$	0.0186	0.0196	0.0192	0.0182	0.0185	0.0182	-5.4	-3.2	2.2	0.5	2.2
$q'$	0.0247	0.0346	0.0401		0.0252	0.0240	-40.1	-62.3		-2.0	2.8
Ave. abs							<b>21.3</b>	<b>27.0</b>		<b>4.4</b>	<b>4.3</b>
<b>PID Controlled</b>											
$u/U$	1.000	0.999	1.000	1.003	1.000	1.001	0.1	0.0	-0.3	0.0	-0.1
$n'$	37.72	44.61	46.19	36.46	36.76	36.48	-18.3	-22.5	3.3	2.5	3.3
$\delta [^\circ]$	0.75	0.74	0.93	0.63	0.75	1.52	1.3	-24.0	16.0	0.00	-102.7
Ave. abs							<b>6.6</b>	<b>15.5</b>	<b>6.5</b>	<b>0.8</b>	<b>35.4</b>
<b>SP factors by the thrust identification</b>											
$t$					0.110						
$J$	0.540	0.648	0.678	0.511	0.510	0.512	-20.0	-25.6	5.4	5.6	5.2
$1 - w_e$	0.701	0.996	1.079	0.642	0.646	0.643	-42.1	-53.9	8.4	7.8	8.3
$J_B$	0.770	0.650	0.629	0.799	0.790	0.797	15.6	18.3	-3.8	-2.6	-3.5
$\eta_0$	0.492	0.564	0.573	0.482	0.481	0.483	-14.6	-16.5	2.0	2.2	1.8
$\eta_R$	1.075	1.345	1.263		0.983	1.004	-25.1	-17.5		8.6	6.6
Ave. abs							<b>23.5</b>	<b>26.3</b>		<b>5.4</b>	<b>5.1</b>
<b>SP factors by the direct measurement</b>											
$1 - w_e$					0.785						
$J_B$					0.625						
$\eta_0$					0.474						

Table 7-2. Breakdown of total F&M for the resistance/SP test (G3)

	Hull	Rudder stock	Rudder	Rudder-TOT	Hub	Blade1	Blade2	Blade3	Blade4	Blade5	Prop-TOT	TOT
<b>X*<math>\times 10^3</math></b>												
[1] Resistance	-4.619	-0.060	-0.059	-0.119								-4.738
[2] SP (AP, no rud)	-5.383				-0.049	1.092	1.091	1.090	1.090	1.088	5.403	0.020
[3] SP (AP, $\delta=0$ )	-4.994	-0.133	-0.155	-0.289	-0.005	1.087	1.079	1.089	1.015	1.045	5.311	0.028
[4] SP (AP, $\delta$ controlled)	-5.008	-0.127	-0.163	-0.289	-0.005	1.083	1.079	1.095	1.018	1.054	5.325	0.028
<b>Y*<math>\times 10^3</math></b>												
[2] SP (AP, no rud)	0.029				-0.004	-0.031	-0.031	-0.031	-0.031	-0.159		-0.130
[3] SP (AP, $\delta=0$ )	-0.067	0.496	-0.027	0.469	-0.005	-0.042	-0.033	-0.009	-0.004	-0.023	-0.116	0.285
[4] SP (AP, $\delta$ controlled)	-0.044	0.437	-0.281	0.156	-0.005	-0.035	-0.020	-0.008	-0.017	-0.036	-0.120	-0.007
<b>Z*<math>\times 10^3</math></b>												
[2] SP (AP, no rud)	-1.574				-0.033	-0.071	-0.072	-0.071	-0.071	-0.071	-0.389	-1.963
[3] SP (AP, $\delta=0$ )	-1.395	-0.143	-0.413	-0.556	-0.031	-0.072	-0.050	-0.050	-0.067	-0.082	-0.352	-2.303
[4] SP (AP, $\delta$ controlled)	-1.294	-0.155	-0.391	-0.545	-0.032	-0.061	-0.054	-0.065	-0.076	-0.073	-0.361	-2.200
<b>K*<math>\times 10^3</math></b>												
[2] SP (AP, no rud)	0.025				0.0002	-0.005	-0.005	-0.005	-0.005	-0.005	-0.026	-0.0005
[3] SP (AP, $\delta=0$ )	0.033	-0.016	0.004	-0.012	0.0002	-0.004	-0.005	-0.006	-0.006	-0.005	-0.026	-0.005
[4] SP (AP, $\delta$ controlled)	0.027	-0.014	0.015	0.001	0.0002	-0.005	-0.005	-0.006	-0.005	-0.005	-0.026	0.002
<b>M*<math>\times 10^3</math></b>												
[1] Resistance	0.277	-0.097	-0.176	-0.273								0.003
[2] SP (AP, no rud)	-0.300				-0.017	0.014	0.014	0.014	0.014	0.052		-0.248
[3] SP (AP, $\delta=0$ )	0.209	-0.074	-0.208	-0.282	-0.015	0.013	0.024	0.024	0.013	0.007	0.066	-0.007
[4] SP (AP, $\delta$ controlled)	0.191	-0.079	-0.198	-0.277	-0.015	0.018	0.022	0.018	0.009	0.011	0.063	-0.023
<b>N*<math>\times 10^3</math></b>												
[2] SP (AP, no rud)	-0.009				0.002	0.013	0.013	0.014	0.013	0.014	0.069	0.060
[3] SP (AP, $\delta=0$ )	0.028	-0.237	0.013	-0.224	0.002	0.019	0.015	0.004	0.001	0.009	0.050	-0.147
[4] SP (AP, $\delta$ controlled)	0.024	-0.209	0.135	-0.074	0.002	0.015	0.008	0.003	0.007	0.016	0.051	0.001

Table 7-3. Breakdown of z-force for the SP test (G3)

[4] SP (AP, $\delta$ controlled)	Hull	Rudder stock	Rudder	Rudder-TOT	Hub	Blade1	Blade2	Blade3	Blade4	Blade5	Prop-TOT	TOT
Friction	0.12	-0.01	-0.01	-0.01	0.00	0.00	0.00	0.00	-0.01	-0.01	-0.02	0.08
Hydrostatic	-723.33	-0.15	-0.38	-0.53	-0.02	-0.01	-0.02	-0.02	-0.02	-0.02	-0.10	-723.95
Hydrodynamic	34.94	0.00	0.00	0.00	-0.02	-0.04	-0.04	-0.04	-0.05	-0.05	-0.24	34.69
Weight	686.98											686.98

Table 7-4. AoAs calculated at different vertical locations

case	Slice	$\Delta x/L$	$\Delta y/L$	AoA [deg]
SP (AP, $\delta=0$ )	H1	0.989492	-0.00069	<b>3.77</b>
	H2	0.990099	-0.00056	<b>3.25</b>
	H4	0.99069	0.000232	<b>-1.43</b>
SP (AP, $\delta$ controlled)	H1	0.989586	-0.00055	<b>3.01</b>
	H2	0.990048	-0.00057	<b>3.28</b>
	H4	0.990717	2.92E-05	<b>-0.18</b>

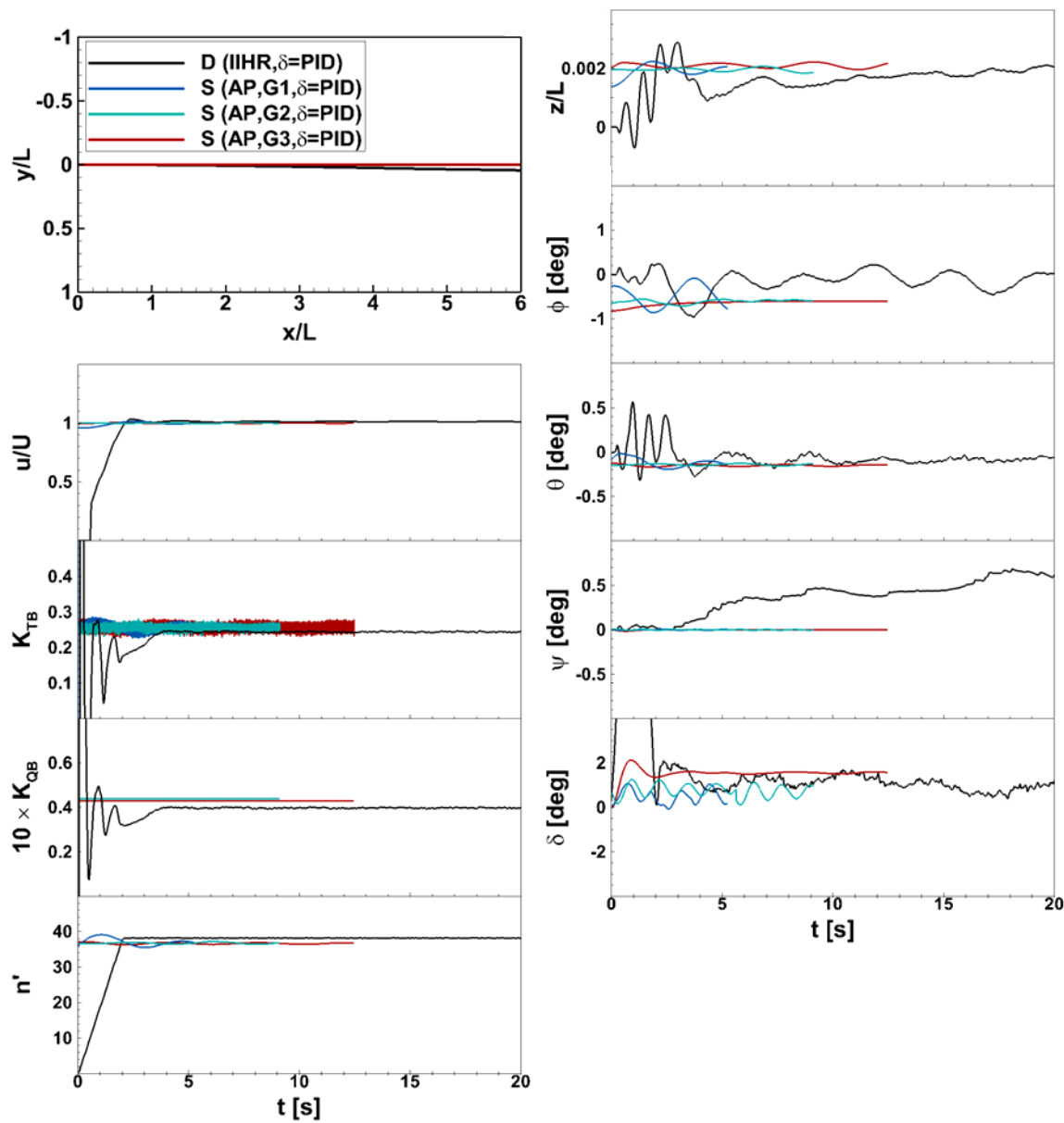


Figure 7-1. Time-histories from the SP test

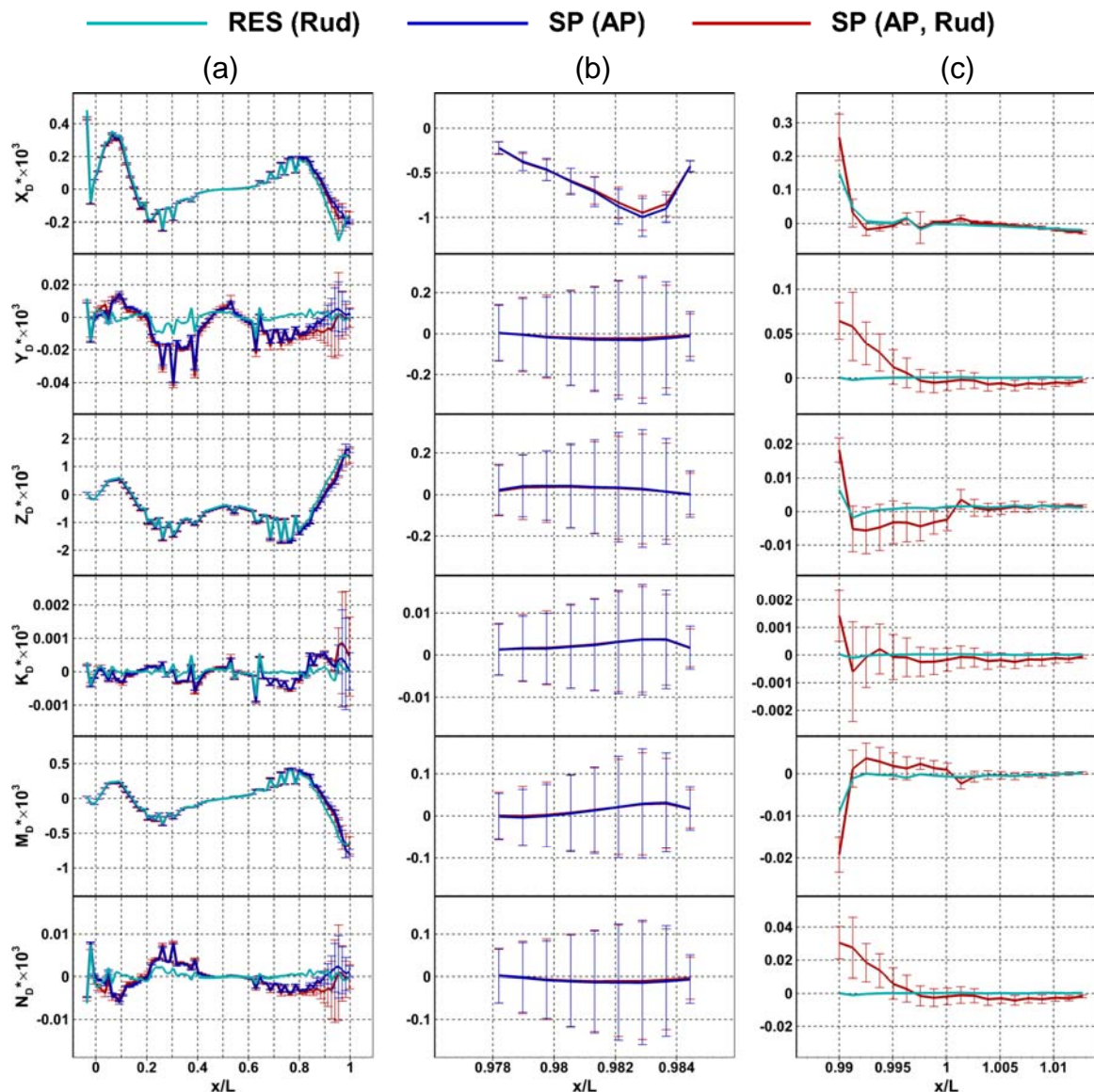


Figure 7-2. Long. distribution of mean hydrodynamic F&M (bar shows SD): (a) BH; (b) Propeller; (c) Rudder

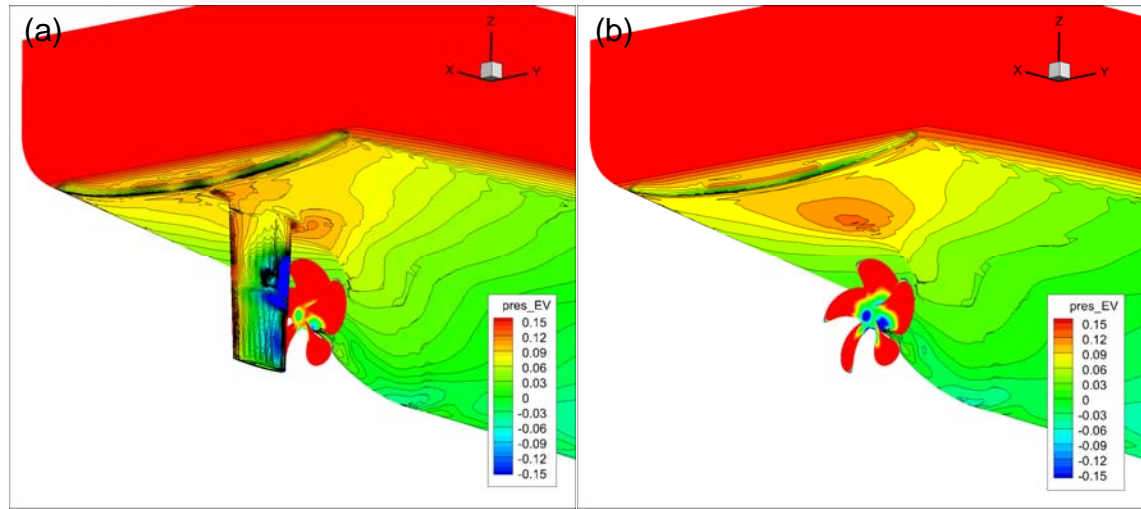


Figure 7-3. Dist. of mean hydrodynamic pressure near the stern: (a) SP with rudder; (b) SP without rudder

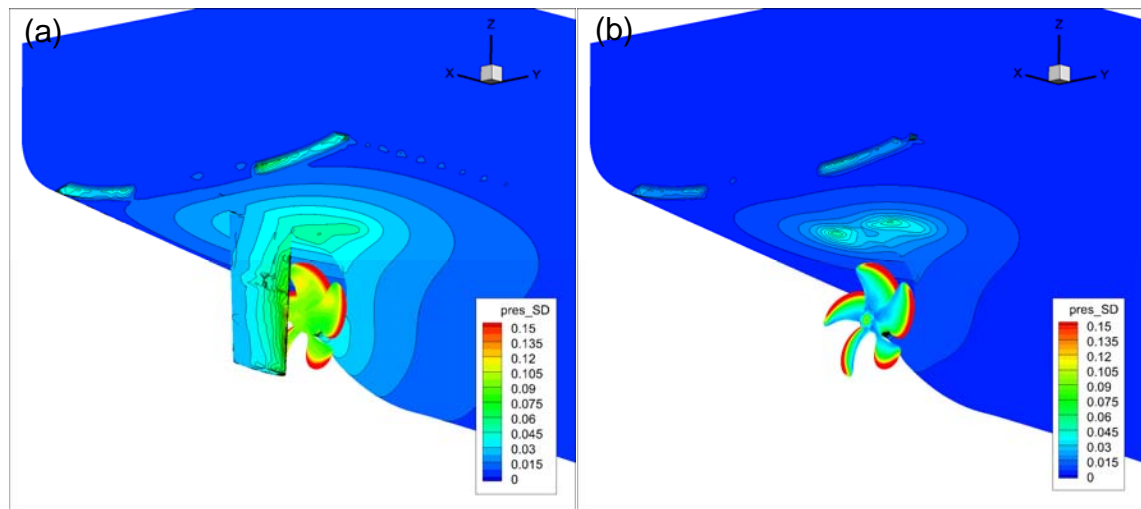


Figure 7-4. Dist. of SD of hydrodynamic pressure near the stern: (a) SP with rudder; (b) SP without rudder

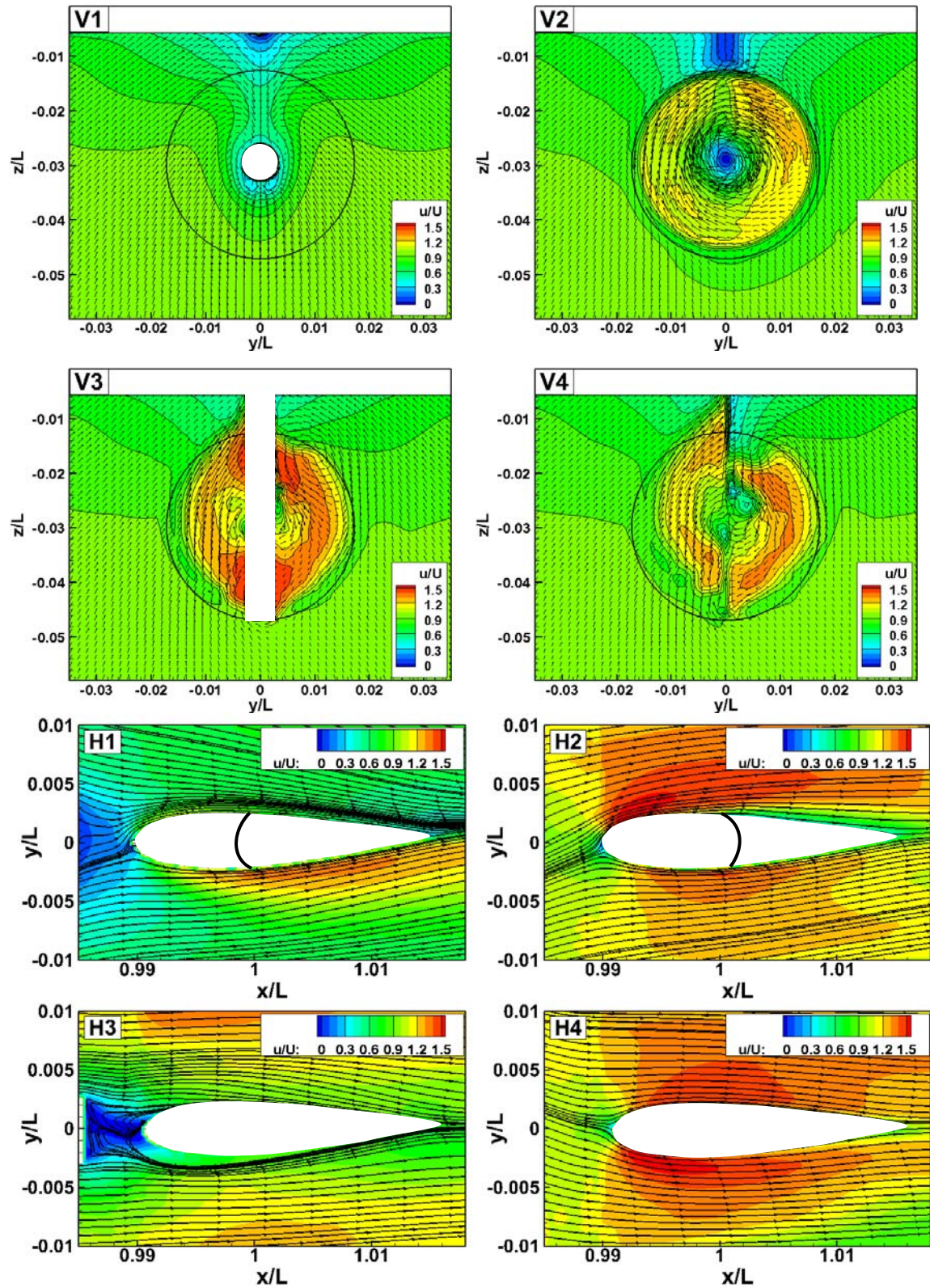


Figure 7-5. Wake-contour/streamlines on V&H sections for the SP test

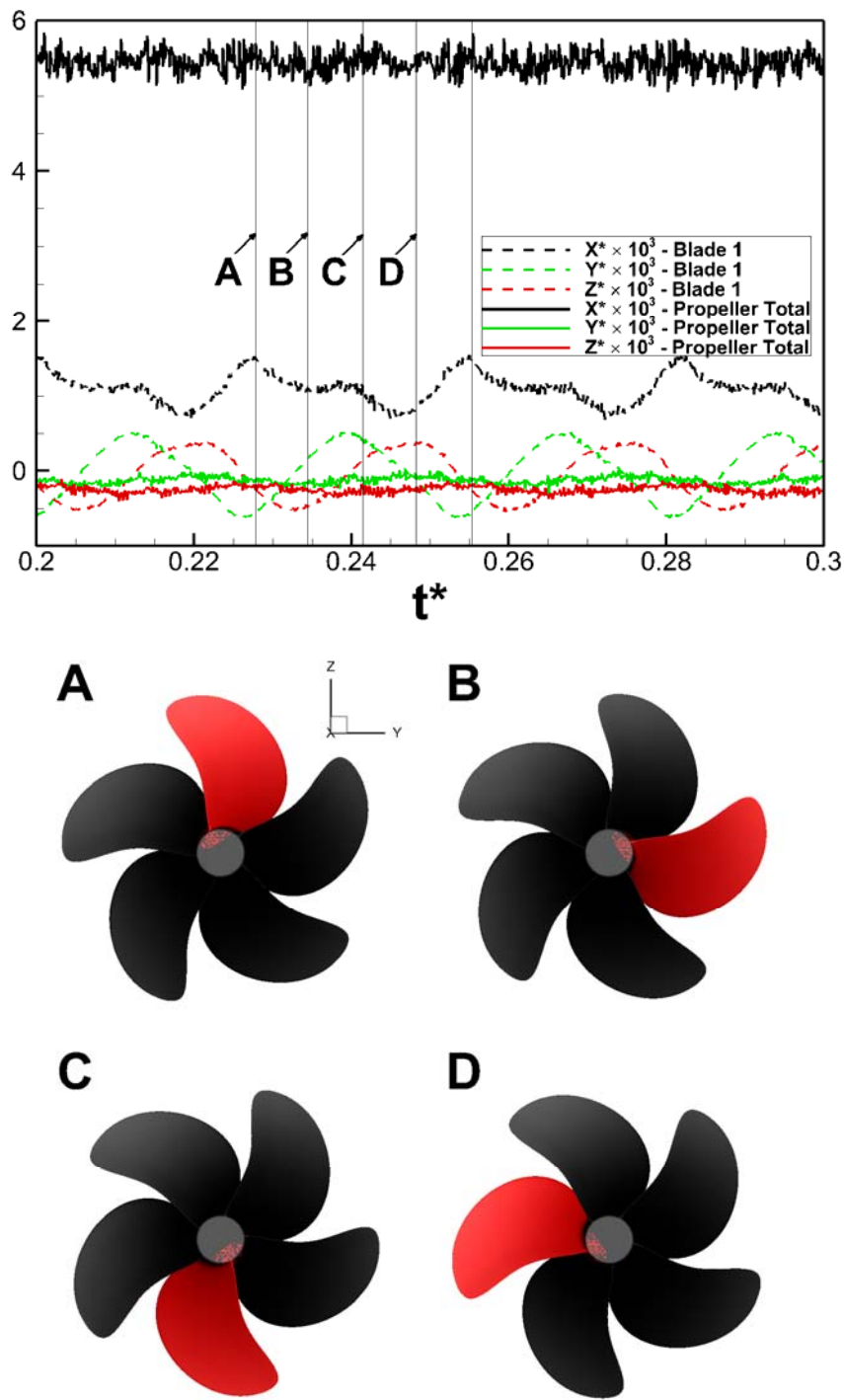


Figure 7-6. Time-histories of forces of a single blade (red) and a propeller from the SP test

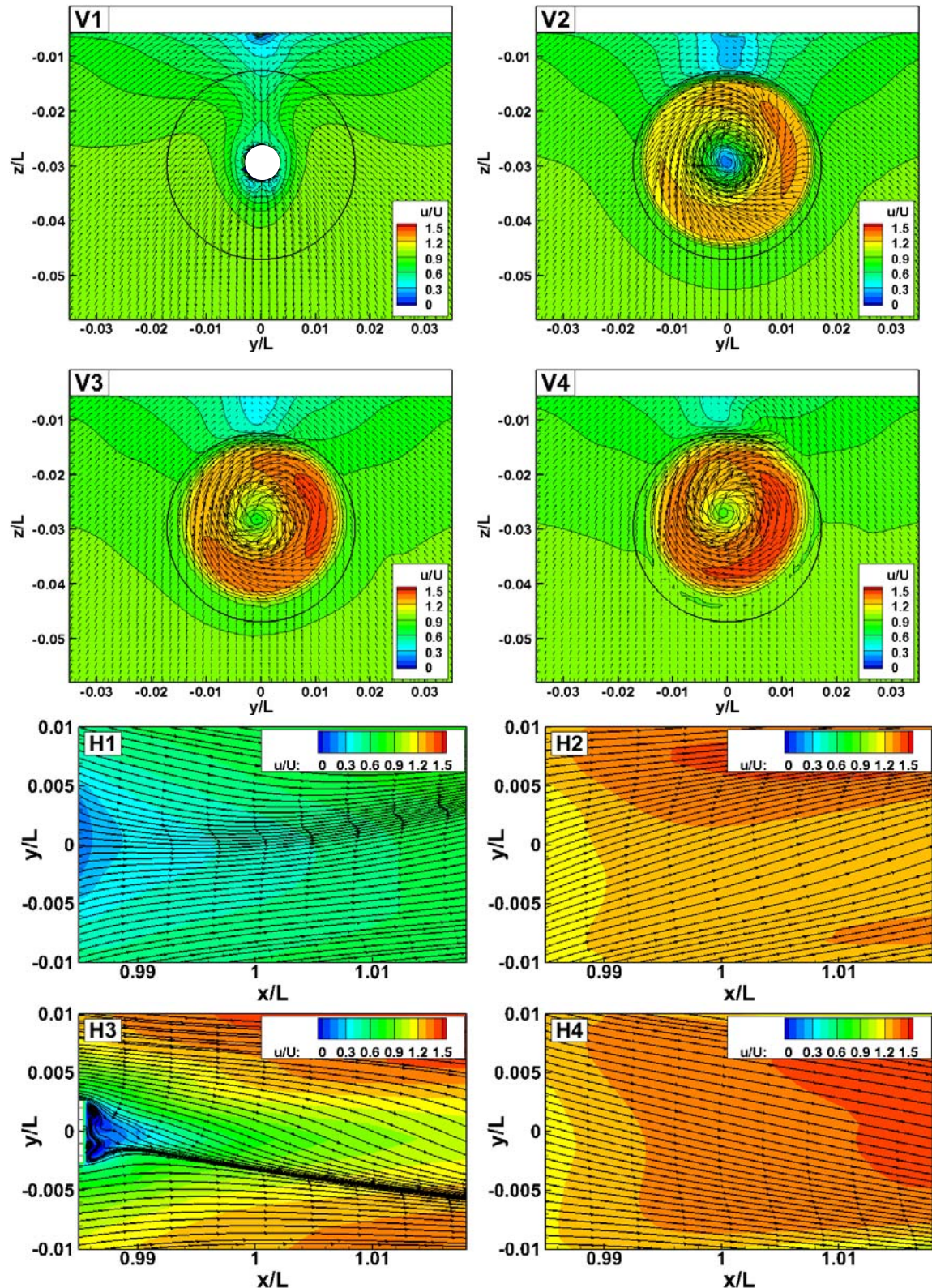


Figure 7-7. Wake-contour/streamlines on V&H sections for the SP test (w/o rudder)

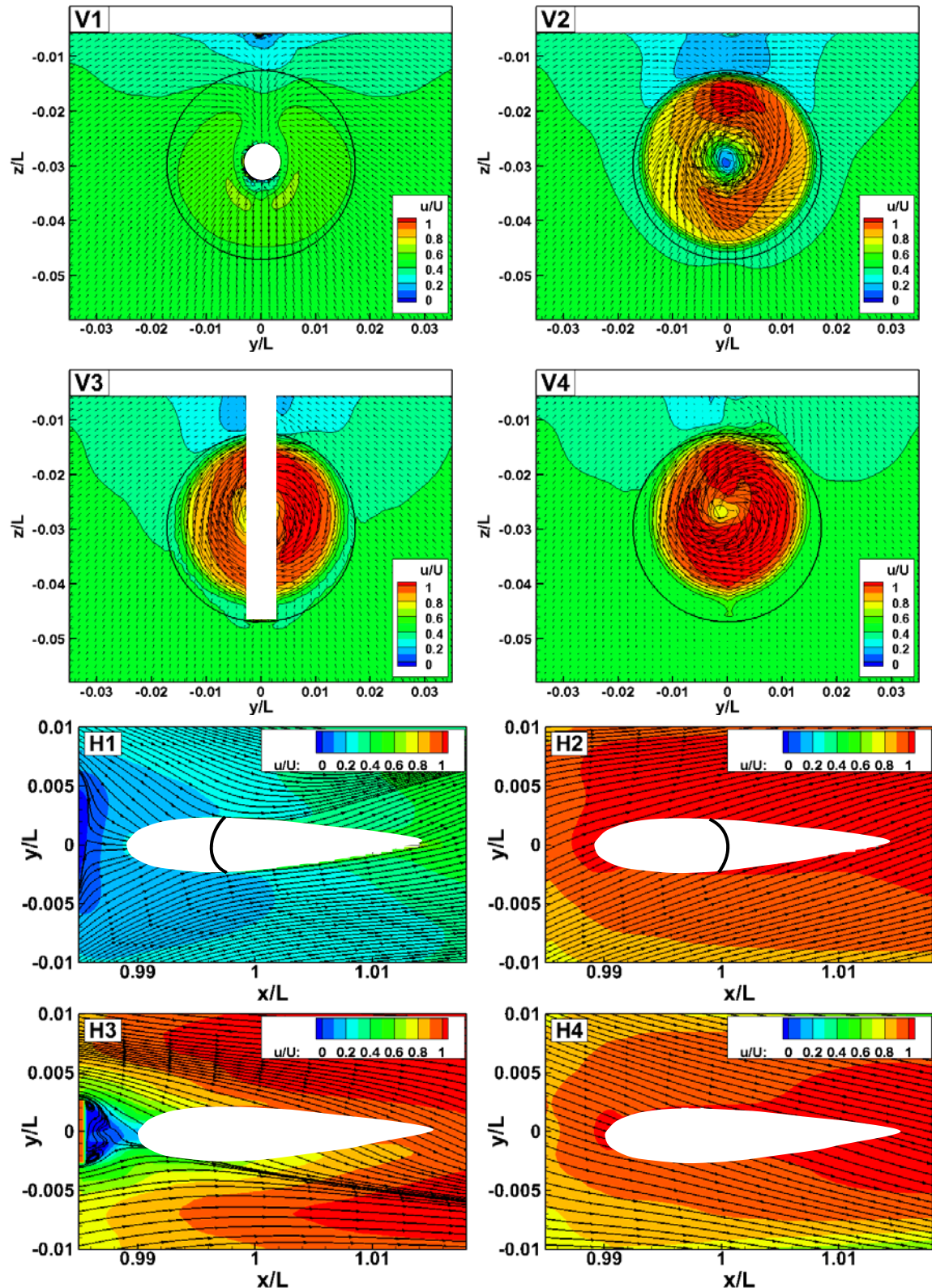


Figure 7-8. Wake-contour/streamlines on V&H sections: Perturbation caused by SP test from the resistance test

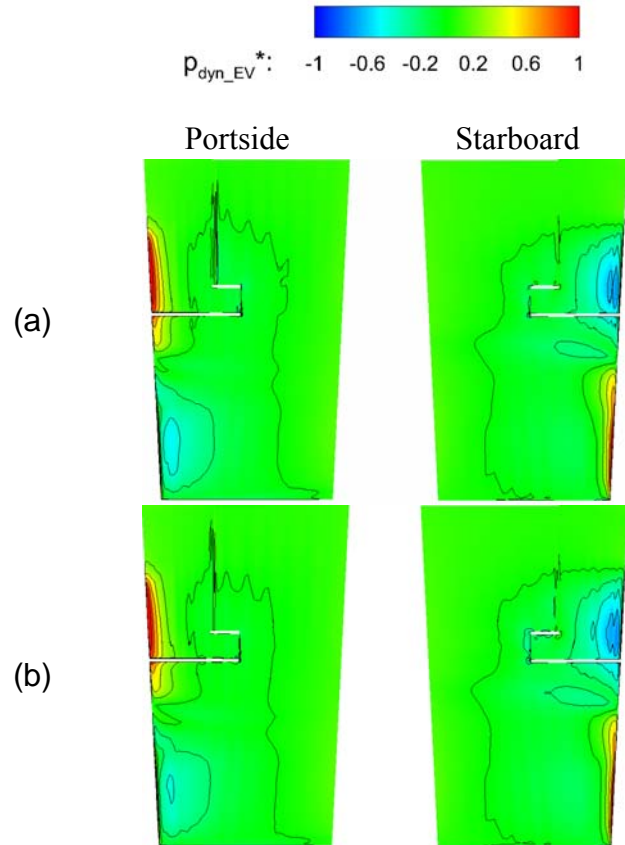


Figure 7-9. Dynamic pressure distribution on the rudder: (a) SP ( $\delta=0$ ); (b) SP (PID controlled  $\delta$ )

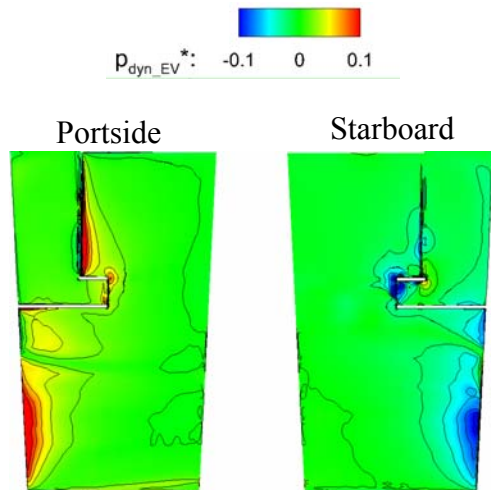


Figure 7-10. Dynamic pressure distribution on the rudder: Perturbation caused by SP ( $\delta=0$ ) test from SP (PID controlled  $\delta$ ) test

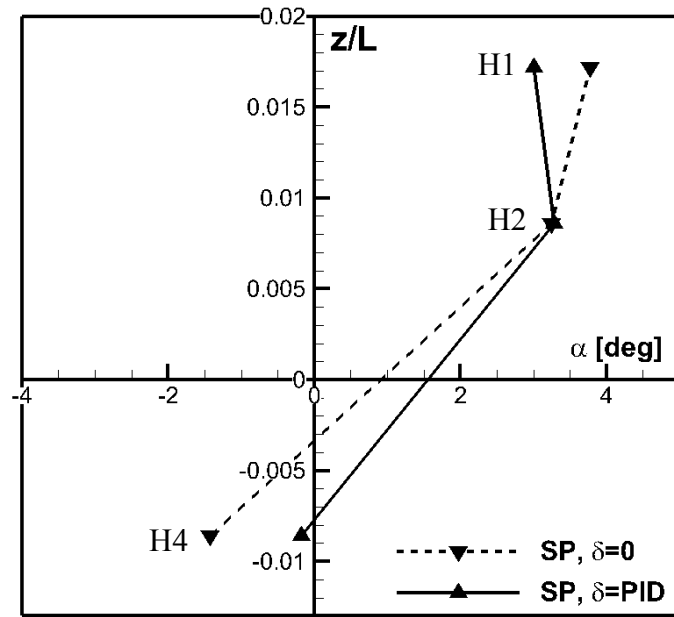


Figure 7-11. AoA on the rudder vs. vertical locations

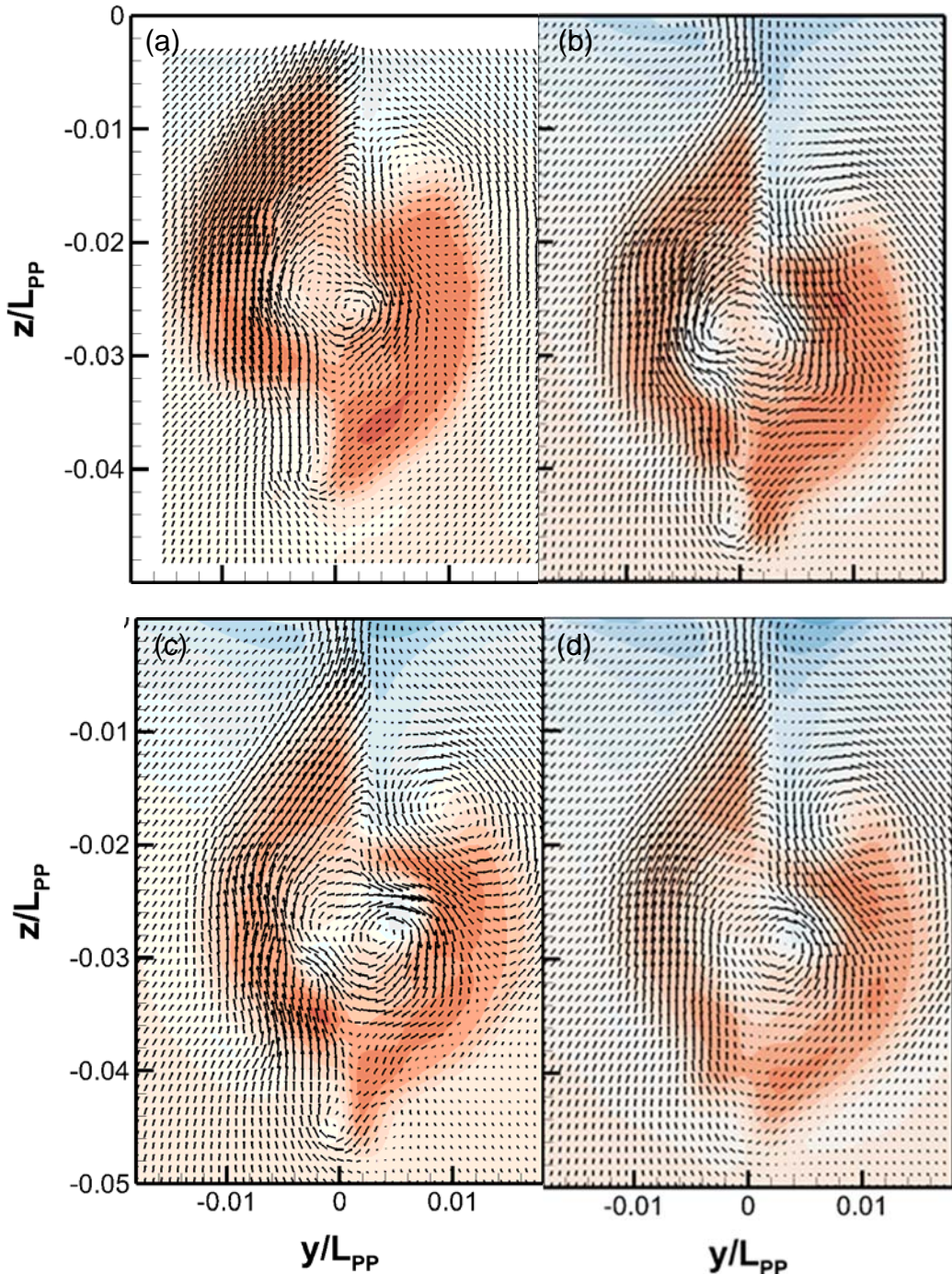


Figure 7-12. Local flow validation at V5: (a) OU PIV; (b) G1-AP; (c) G2-AP; (d) G3-AP

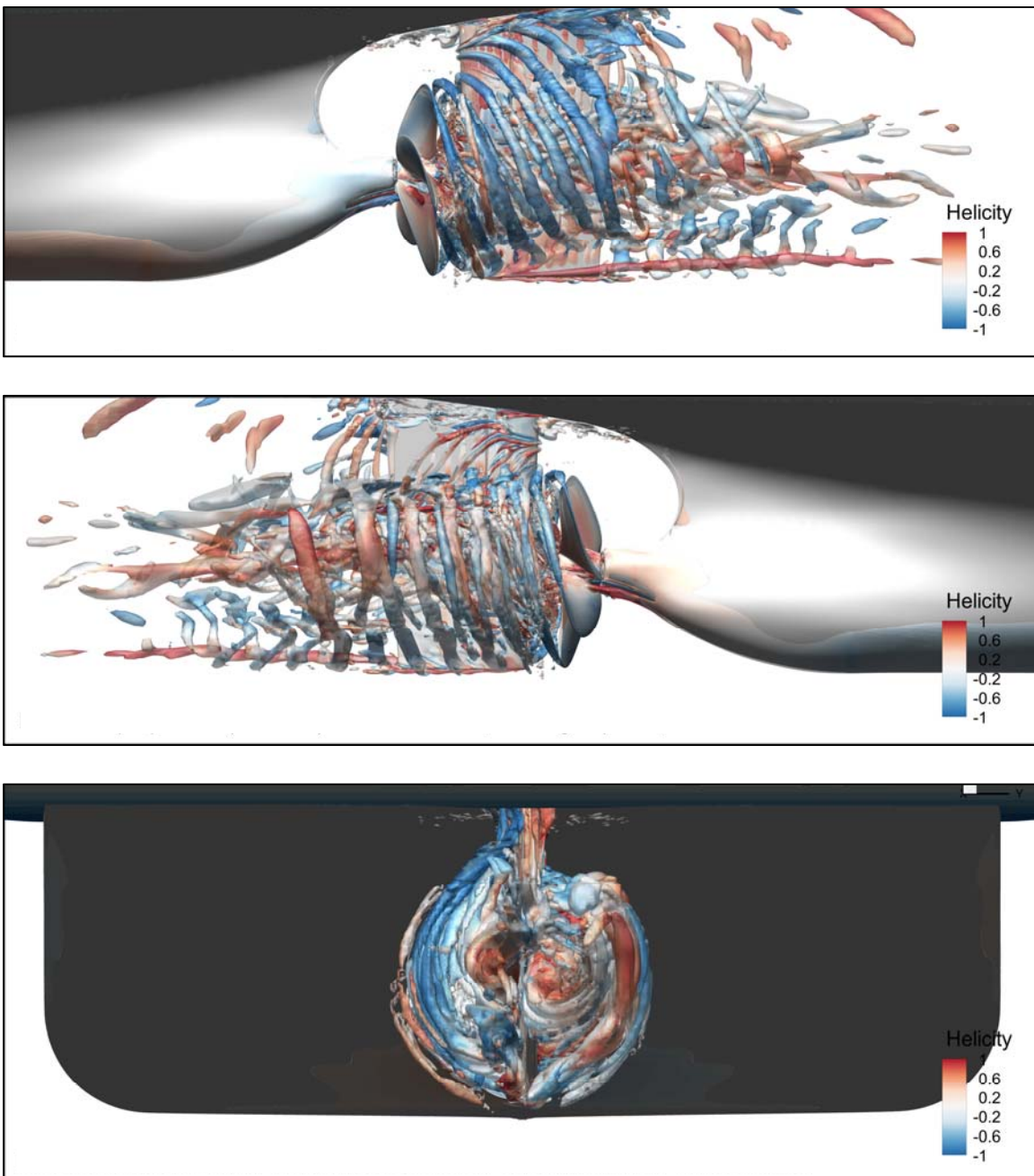


Figure 7-13. Pressure on hull and blades and  $Q = 1000$  at wake for SP test (G1)

## 8. CALM WATER MANEUVERING

### 8.1. Turning-circle Test

#### Validation

Figure 8-1 and 8-2 show the trajectory and time-histories of motions for  $\pm 35^\circ$  turning-circle tests and Table 1 shows the  $E\%D$  for IMO (International Maritime Organization) criteria. G2-BF shows better agreement to MARIN or JMU (Japan Maritime University) during the starboard turning. G3-AP showed different trend from the zig-zag, and it matched better with IIHR up to transfer ( $Tr/L$ ). For portside turning, neither of G2-BF or G3-AP agrees well with IIHR or MARIN, which again emphasize the lack of turning ability for CFD model during the portside turning. Meanwhile, both results are matching well with JMU experiment result which was performed with smaller model than IIHR or MARIN. The KCS model, due to single screw, tends to have small tactical diameter ( $Td/L$ ) for the portside turning compared to the starboard turning. While the experimental results follow the trend, CFD results show almost symmetrical trajectories.

#### Sensitivity test

Sensitivity test is done for the starboard turning ( $+36^\circ$  for the maximum rudder angle) and the result shows almost the same result with the normal starboard turning results, which indicates that the  $1^\circ$  of rudder angle difference does not affect the turning test.

#### Forces and moments

In Figure 8-1 and 8-2, the thrust and torque coefficients for both AP and BF models increase significantly starting from the calm water self-propulsion values due to the amplification and redistribution of the nominal wake during the turning (Figure 8-7). The yaw moment of the rudder is always larger for G2-BF than G3-AP due to the higher magnitude of dimensional thrust.

The effective wake predicted by BF model is not accurate, therefore, the possibility exists that the trajectory of BF model might have been closer to experiment data than the AP model due to inaccurate thrust and torque. The yaw moment of rudder of G2-AP is in the middle of G3-AP and G2-BF, however, the trajectory is still closer to G3-AP. The magnitude of yaw moment of propeller is one order less than the yaw moment of rudder, which means that the rudder force is a more dominant during the test.

## 8.2. Zig-zag Test

### Validation

Figure 8-3 to 8-6 show the trajectories and time-histories for  $\pm 10^\circ/10^\circ$  and  $\pm 20^\circ/20^\circ$  zig-zag tests. Table 2 and 3 shows the  $E\%D$  for IMO criteria. CFD results for zig-zag  $10^\circ/10^\circ$  and  $20^\circ/20^\circ$  show better agreement with IIHR when the ship turns to portside while the agreement with MARIN or JMU is better when the ship turns to starboard. G3-AP showed poorer prediction than G2-BF when the ship turns to portside even though the propulsion model is superior. The difference of turning capability becomes noticeable when the yaw rates for both the G3-AP and the G2-BF are checked.

### Sensitivity test

The preliminary test for initial rudder offset angle sensitivity is performed for zig-zag  $+10^\circ/10^\circ$  and  $+20^\circ/20^\circ$ . G2-BF is used. With the same initial condition (PID controlled  $\delta$ ), the rudder range of  $-9^\circ$  to  $11^\circ$  and  $-19^\circ$  to  $21^\circ$  are used for zig-zag  $+10^\circ/10^\circ$  and  $+20^\circ/20^\circ$  cases, respectively: 1 degree offsets are given to normal rudder ranges. Initially, the test objective is to see the effect of the rudder range calibration when the neutral rudder angle exist, which is near to  $1^\circ$  in this test. Using the shifted rudder range is more effective for zig-zag  $+10^\circ/10^\circ$  case than

$+20^\circ/20^\circ$  case. For  $+10^\circ/10^\circ$  case, the shifted rudder range condition shows much different results for most of the variables and  $E\%D$  is smaller for MARIN. For the  $+20^\circ/20^\circ$  case, the effect still exists, but it does not change the trend much for most of the variables. From this study, it was found that even the small amount of change on the maximum rudder angle can affect the zig-zag trend since the difference of rudder force caused by  $1^\circ$  deflection constantly affect the ship during the overshoot, which is a long duration during the entire zig-zag test.

Table 8-1. Validation on IMO criteria for  $\pm 35^\circ$  turning-circle tests

$\delta$ [deg]	Var.	D		S			E%D (D=IIHR)				E%D (D=MARIN)							
	Case	IIHR	MARIN	BF, G2			AP, G3	BF, G2			AP, G3	BF, G2			AP, G3			
	$k_{xx}/B$	0.39	n/a	0.39	0.45			0.39	0.45			0.39	0.45					
	$\delta$	PID controlled		0	PID controlled			0	PID controlled			0	PID controlled					
	$\delta$ range					+1° shifted				+1° shifted				+1° shifted				
$35^\circ$	$Ad/L$	3.06	2.90	2.99	2.99	2.96	2.95	3.11	2.2	2.3	3.3	3.7	-1.6	-3.2	-3.0	-2.0	-1.6	-7.3
	$Tr/L$	1.34	1.21	1.17	1.16	1.15	1.14	1.22	13.2	13.5	14.1	14.8	8.6	3.4	3.8	4.4	5.3	-1.2
	$TD/L$	3.08	2.83	2.83	2.80	2.79	2.76	3.08	8.2	9.1	9.4	10.3	-0.1	0.1	1.1	1.5	2.4	-9.0
	$t^*(Ad, Tr)$	4.39	4.18	4.11	4.10	4.07	4.06	4.25	6.4	6.7	7.3	7.5	3.3	1.6	1.9	2.5	2.7	-1.6
	$t^*(TD)$	8.44	8.41	7.71	7.67	7.63	7.62	8.48	8.6	9.0	9.5	9.7	-0.5	8.2	8.7	9.2	9.3	-0.8
	Ave. abs						<b>7.7</b>		<b>8.1</b>	<b>8.7</b>	<b>9.2</b>	<b>2.8</b>	<b>3.3</b>		<b>3.7</b>	<b>3.9</b>	<b>4.3</b>	<b>4.0</b>
$-35^\circ$	$Ad/L$	2.87	2.93	3.06	3.08		3.12	-6.8	-7.2		-8.8		-4.4	-4.8		-6.6		
	$Tr/L$	-1.13	-1.09	-1.22	-1.23		-1.26	-8.0	-8.4		-11.4		-12.8	-13.2		-15.5		
	$TD/L$	-2.69	-2.64	-2.90	-2.90		-3.00	-7.9	-8.0		-11.5		-9.8	-9.9		-13.6		
	$t^*(Ad, Tr)$	4.09	4.18	4.22	4.23		4.34	-3.1	-3.4		-6.1		-0.8	-1.0		-3.9		
	$t^*(TD)$	7.88	8.08	7.87	7.87		8.35	0.2	0.2		-6.0		2.7	2.7		-3.4		
	Ave. abs						<b>5.2</b>	<b>5.4</b>		<b>8.8</b>		<b>6.1</b>	<b>6.3</b>		<b>8.6</b>			

Table 8-2. Validation on IMO criteria for  $\pm 10^\circ/10^\circ$  zig-zag test

$\delta$ [deg]	OS	Var.	D		S			E%D (D=IIHR)				E%D (D=MARIN)				
		Case	IIHR	MARIN	BF, G2		AP, G3	BF, G2		AP, G3	BF, G2		AP, G3			
		$k_{xx}/B$	0.39	n/a	0.45			0.45			0.45					
		$\Delta$	PID controlled		0	PID controlled			0	PID controlled			0	PID controlled		
		$\delta$ range					+1° shifted			+1° shifted				+1° shifted		
$+10^\circ/10^\circ$	1 <sup>st</sup>	$t^*$	3.08	3.61	3.40	3.36	3.54	3.58	-10.2	-9.1	-14.8	-16.0	5.8	6.7	1.8	0.8
		$x/L$	3.02	3.47	3.28	3.25	3.39	3.47	-8.9	-7.7	-12.4	-15.0	5.5	6.6	2.4	0.2
		$y/L$	0.36	0.59	0.46	0.45	0.54	0.50	-29.4	-27.1	-52.6	-41.9	22.3	23.7	8.3	14.8
		$\psi [deg]$	18.55	23.00	21.56	21.50	23.46	21.98	-16.2	-15.9	-26.5	-18.5	6.3	6.5	-2.0	4.4
		$OSA [deg]$	8.55	13.00	11.56	11.50	13.46	11.98	-35.1	-34.4	-57.4	-40.0	11.1	11.6	-3.6	7.8
		Ave. abs						<b>19.9</b>	<b>18.8</b>	<b>32.7</b>	<b>26.3</b>	<b>10.2</b>	<b>11.0</b>	<b>3.6</b>	<b>5.6</b>	
	2 <sup>nd</sup>	$t^*$	8.21	9.60	9.31	9.25	10.2		-13.4	-12.7	-24.3		3.0	3.6	-6.3	
$-10^\circ/10^\circ$	1 <sup>st</sup>	$x/L$	7.51	8.65	8.49	8.46	9.09		-13.0	-12.5	-20.9		1.9	2.2	-5.1	
		$y/L$	0.36	0.75	0.27	0.75	-0.02		23.1	-111.4	104.5		63.3	-0.9	102.1	
		$\psi [deg]$	-29.46	-30.85	-32.46	-29.74	-38.07		-10.2	-1.0	-29.2		-5.2	3.6	-23.4	
		$OSA [deg]$	19.46	20.85	22.46	19.74	28.07		-15.4	-1.4	-44.3		-7.7	5.3	-34.6	
		Ave. abs						<b>15.0</b>	<b>27.8</b>	<b>44.6</b>		<b>16.2</b>	<b>3.1</b>	<b>34.3</b>		
		$t^*$	3.41	3.53	3.63		4.19		-6.6		-22.8		-2.9		-18.6	
		$x/L$	3.22	3.37	3.46		3.91		-7.5		-21.3		-2.6		-15.9	
	2 <sup>nd</sup>	$y/L$	-0.54	-0.40	-0.59		-0.81		-9.3		-49.5		-47.5		-101.8	
		$\psi [deg]$	-24.07	-20.76	-24.33		-27.23		-1.1		-13.1		-17.2		-31.2	
		$OSA [deg]$	14.07	10.76	14.33		17.23		-1.8		-22.5		-33.2		-60.1	
		Ave. abs						<b>5.3</b>	<b>25.8</b>		<b>20.7</b>		<b>45.5</b>			
		$t^*$	8.75	9.42	9.28		10.67		-6.1		-22.0		1.4		-13.3	
		$x/L$	8.01	8.50	8.44		9.50		-5.4		-18.6		0.6		-11.8	
		$y/L$	-1.05	-0.29	-0.83		-1.08		21.2		-2.8		-184.1		-272.2	
		$\psi [deg]$	23.01	30.23	31.04		33.68		-34.9		-46.4		-2.7		-11.4	
		$OSA [deg]$	13.01	20.23	21.04		23.68		-61.7		-82.0		-4.0		-17.1	
		Ave. abs						<b>25.8</b>		<b>34.4</b>		<b>38.6</b>		<b>65.1</b>		

Table 8-3. Validation on IMO criteria for  $\pm 20^\circ/20^\circ$  zig-zag tests

$\delta$ [deg]	OS	Var.	D		S			E%D (D=IIHR)				E%D (D=MARIN)					
		Case	IIHR	MARIN	BF, G2		AP, G3	BF, G2		AP, G3	BF, G2		AP, G3				
		$k_{xx}/B$	0.39	n/a	0.39	0.45		0.39	0.45		0.39	0.45					
		$\delta$	PID controlled		0	PID controlled		0	PID controlled		0	PID controlled					
		$\delta$ range					+1° shifted			+1° shifted							
$+20^\circ/20^\circ$	1st	$t^*$	3.36	3.63	3.77	3.78	3.81	3.85	4.06	-12.2 -12.6 -13.3	-14.6	-20.7	-4.0 -4.3 -5.0	-6.2	-11.9		
		$x/L$	3.02	3.11	3.29	3.29	3.29	3.30	3.53	-8.9 -8.9 -9.0	-9.2	-16.7	-5.7 -5.7 -5.8	-6.0	-13.3		
		$y/L$	0.68	0.95	0.91	0.92	0.94	0.99	1.05	-33.4 -35.5 -38.5	-44.4	-53.8	4.6 3.1 1.0	-3.3	-10.0		
		$\psi [deg]$	39.35	43.22	43.64	44.01	44.05	45.41	44.36	-10.9 -11.8 -12.0	-15.4	-12.7	-1.0 -1.8 -1.9	-5.1	-2.6		
		$OSA [deg]$	19.35	23.22	23.64	24.01	24.05	25.41	24.36	-22.2 -24.1 -24.3	-31.3	-25.9	-1.8 -3.4 -3.6	-9.4	-4.9		
		Ave. abs						<b>17.5</b>	<b>18.6</b>	<b>19.4</b>	<b>23.0</b>	<b>26.0</b>	<b>3.4</b>	<b>3.7</b>	<b>3.4</b>	<b>6.0</b>	<b>8.5</b>
	2nd	$t^*$	8.59	9.34	9.63	9.59		9.72	10.22	-12.1	-11.7	-13.2	-19.1	-3.0	-2.6	-4.0	-9.4
$-20^\circ/20^\circ$	1st	$x/L$	6.62	6.89	7.43	7.34		7.40	7.72	-12.2	-10.8	-11.6	-16.5	-7.9	-6.6	-7.4	-12.0
		$y/L$	1.31	1.91	1.76	1.70		1.87	1.84	-33.8	-29.9	-42.5	-40.5	7.9	10.6	2.0	3.3
		$\psi [deg]$	-41.81	-41.58	-44.09	-44.42		-43.42	-45.67	-5.5	-6.2	-3.9	-9.2	-6.0	-6.8	-4.4	-9.8
		$OSA [deg]$	21.81	21.58	24.09	24.42		23.42	25.67	-10.5	-12.0	-7.4	-17.7	-11.6	-13.1	-8.5	-18.9
		Ave. abs						<b>14.8</b>	<b>14.1</b>	<b>15.7</b>	<b>20.6</b>	<b>26.0</b>	<b>7.3</b>	<b>8.0</b>	<b>5.3</b>	<b>10.7</b>	
		$t^*$	3.63	3.82	3.88	4.18			-6.8		-15.0		-1.5		-9.3		
		$x/L$	3.06	3.25	3.35	3.52			-9.5		-14.9		-3.3		-8.4		
	2nd	$y/L$	-0.86	-0.86	-0.99	-1.17		-15.7		-36.6		-15.7		-36.6			
		$\psi [deg]$	-44.81	-44.40	-44.39	-47.92		0.9		-6.9		0.0		-7.9			
		$OSA [deg]$	24.81	24.40	24.39	27.92		1.7		-12.5		0.0		-14.4			
		Ave. abs						<b>6.9</b>	<b>17.2</b>		<b>4.1</b>		<b>15.3</b>				
		$t^*$	9.13	9.59	9.46	9.83		-3.6		-7.7		1.4		-2.4			
		$x/L$	6.88	7.12	7.26	7.35		-5.5		-6.8		-2.0		-3.2			
		$y/L$	-1.88	-1.81	-1.89	-2.24		-0.5		-18.7		-4.8		-23.8			
		$\psi [deg]$	36.59	40.04	45.09	44.55		-23.2		-21.7		-12.6		-11.2			
		$OSA [deg]$	16.59	20.04	25.09	24.55		-51.2		-47.9		-25.2		-22.5			
		Ave. abs						<b>16.8</b>	<b>20.6</b>		<b>9.2</b>		<b>12.6</b>				

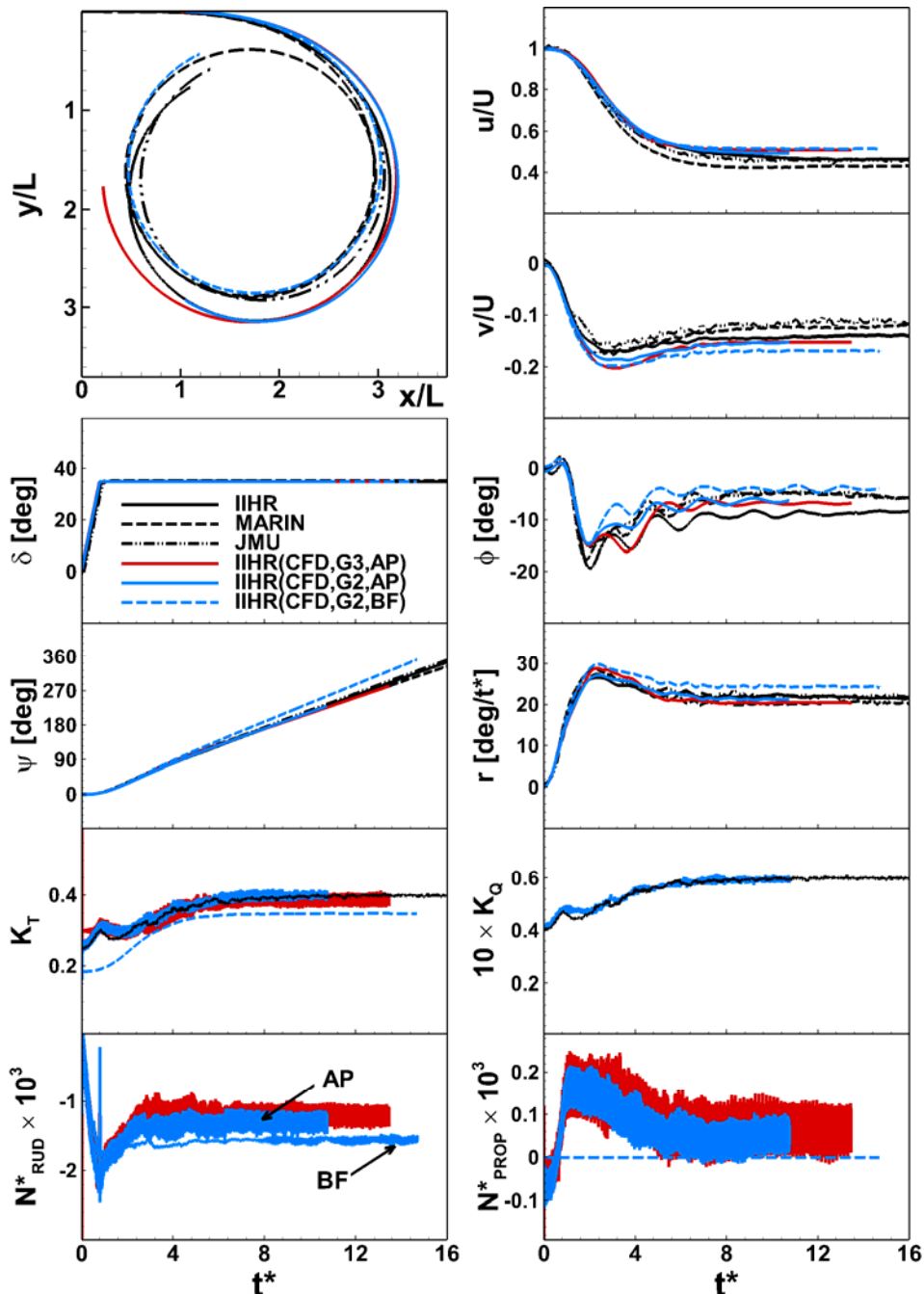


Figure 8-1. Time-histories from the  $+35^\circ$  turning-circle test

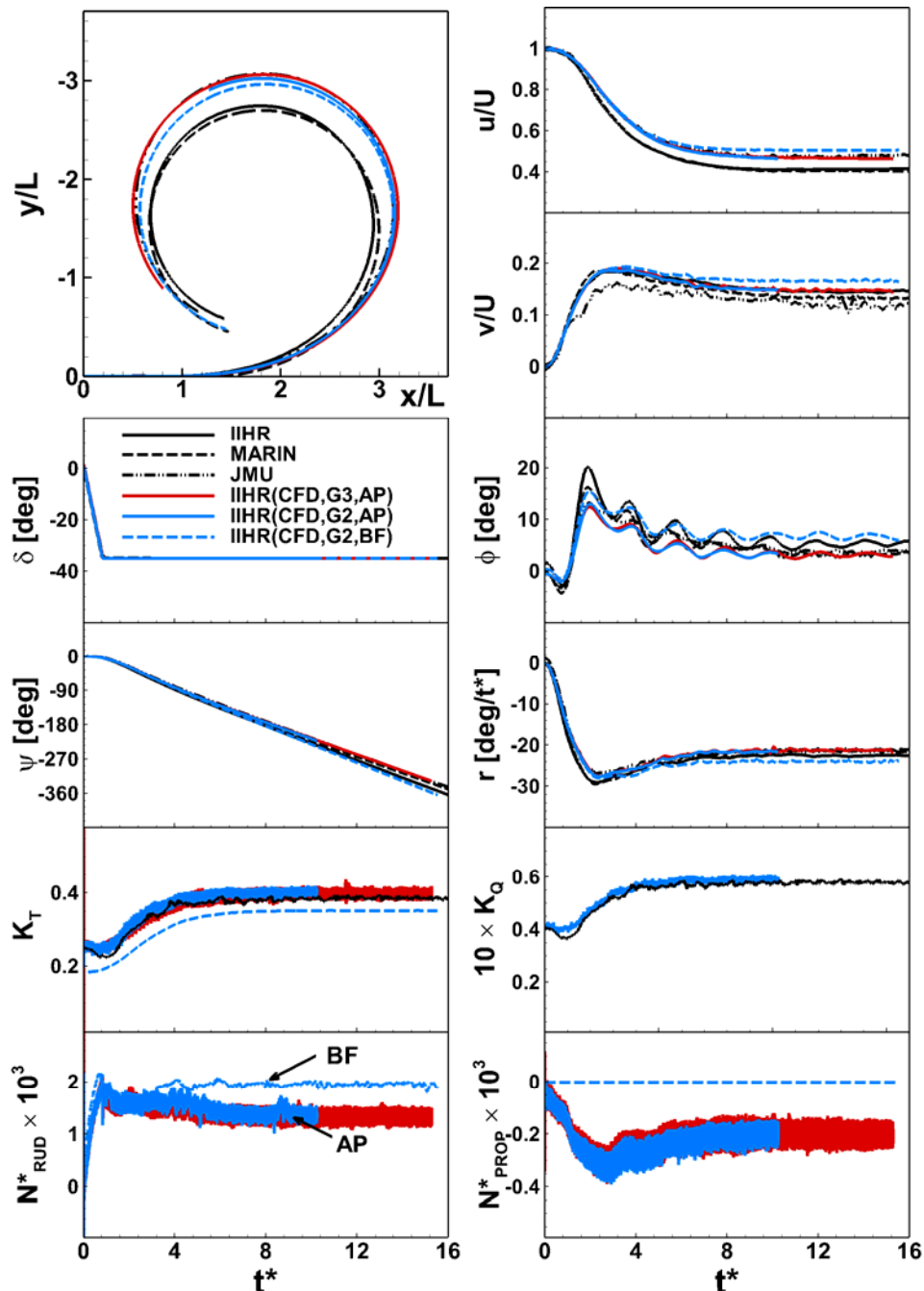


Figure 8-2. Time-histories from the  $-35^\circ$  turning-circle test

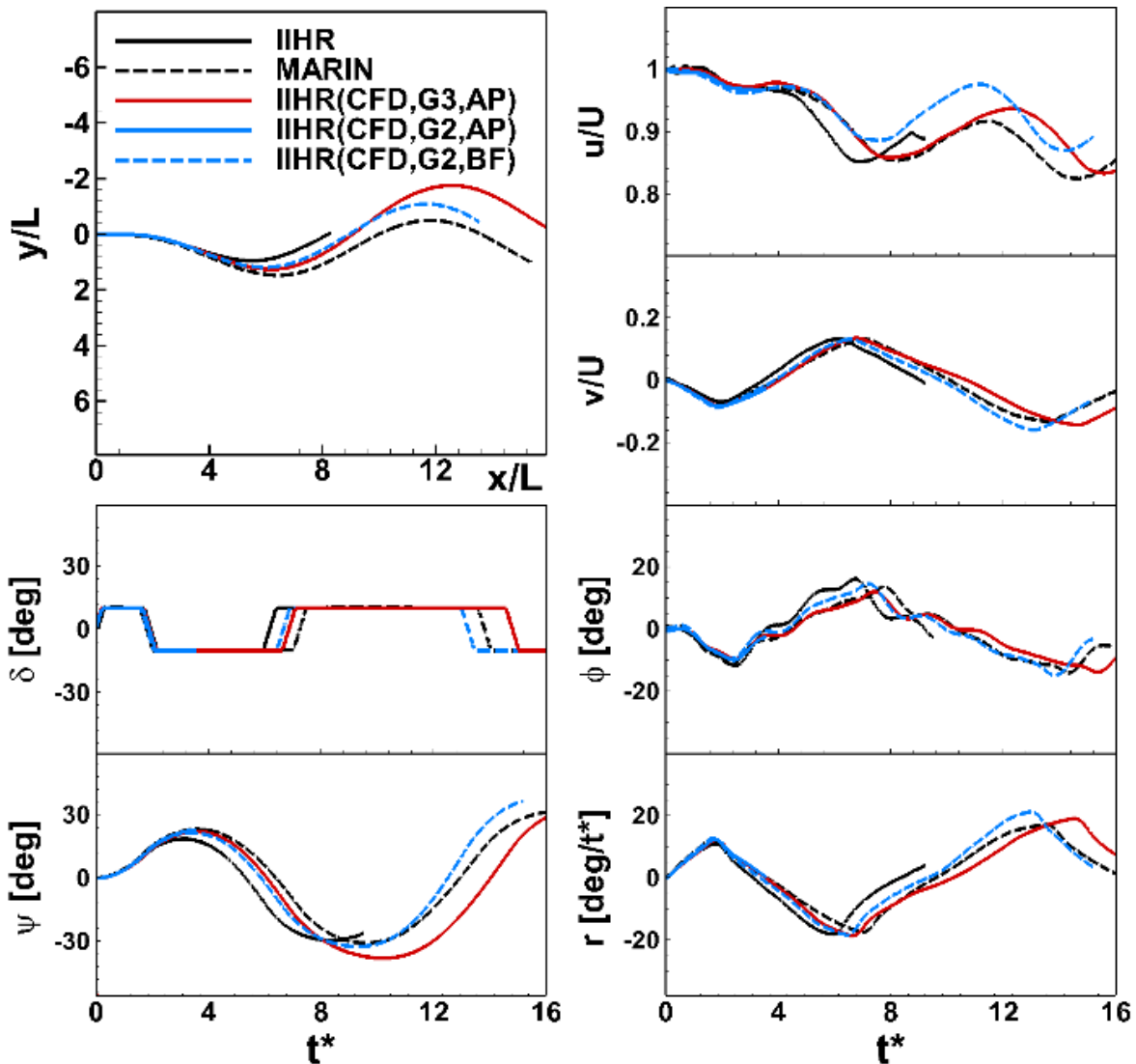


Figure 8-3. Time-histories from the  $+10^\circ/10^\circ$  zig-zag test

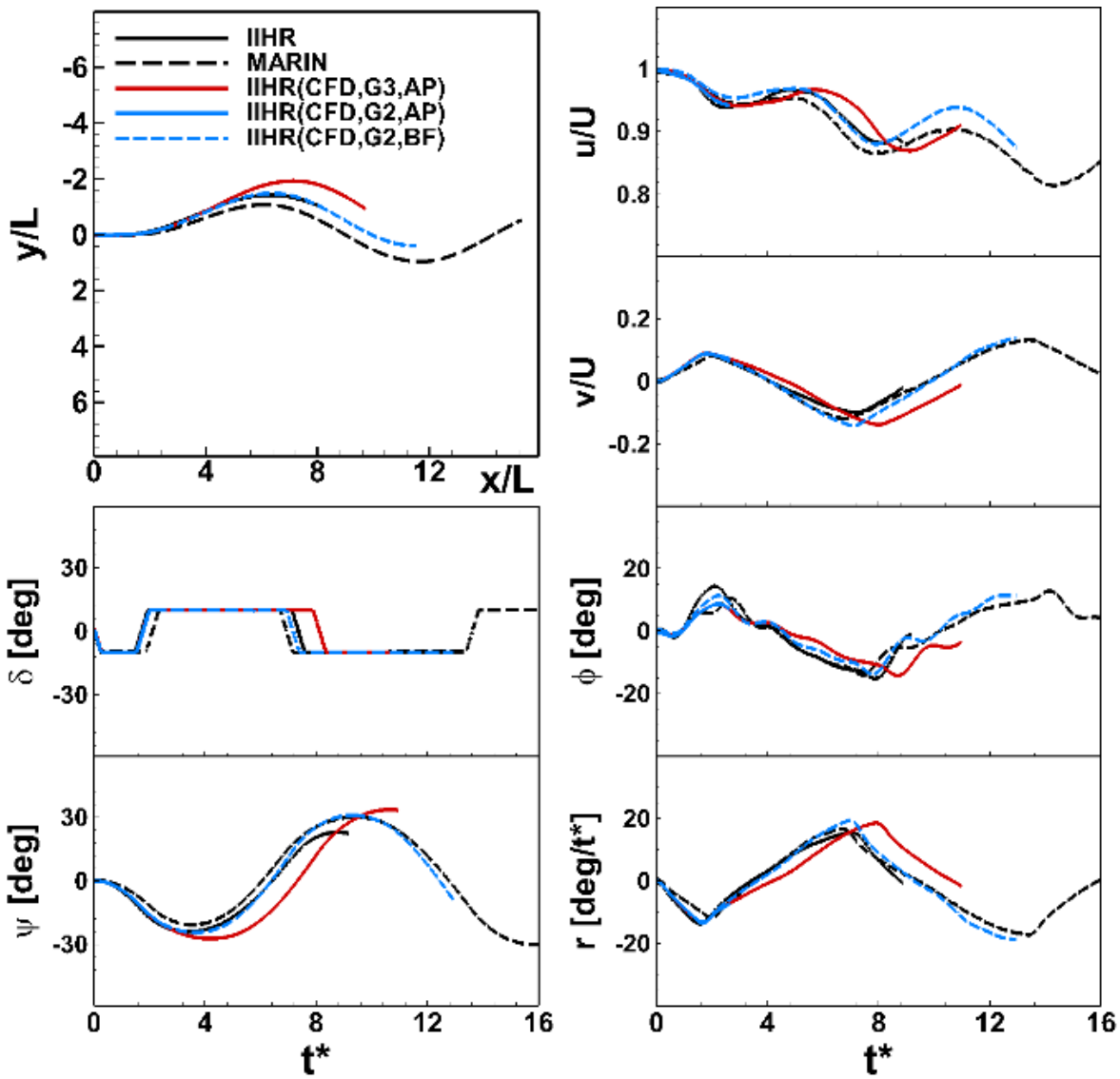


Figure 8-4. Time-histories from the  $-10^\circ/10^\circ$  zig-zag test

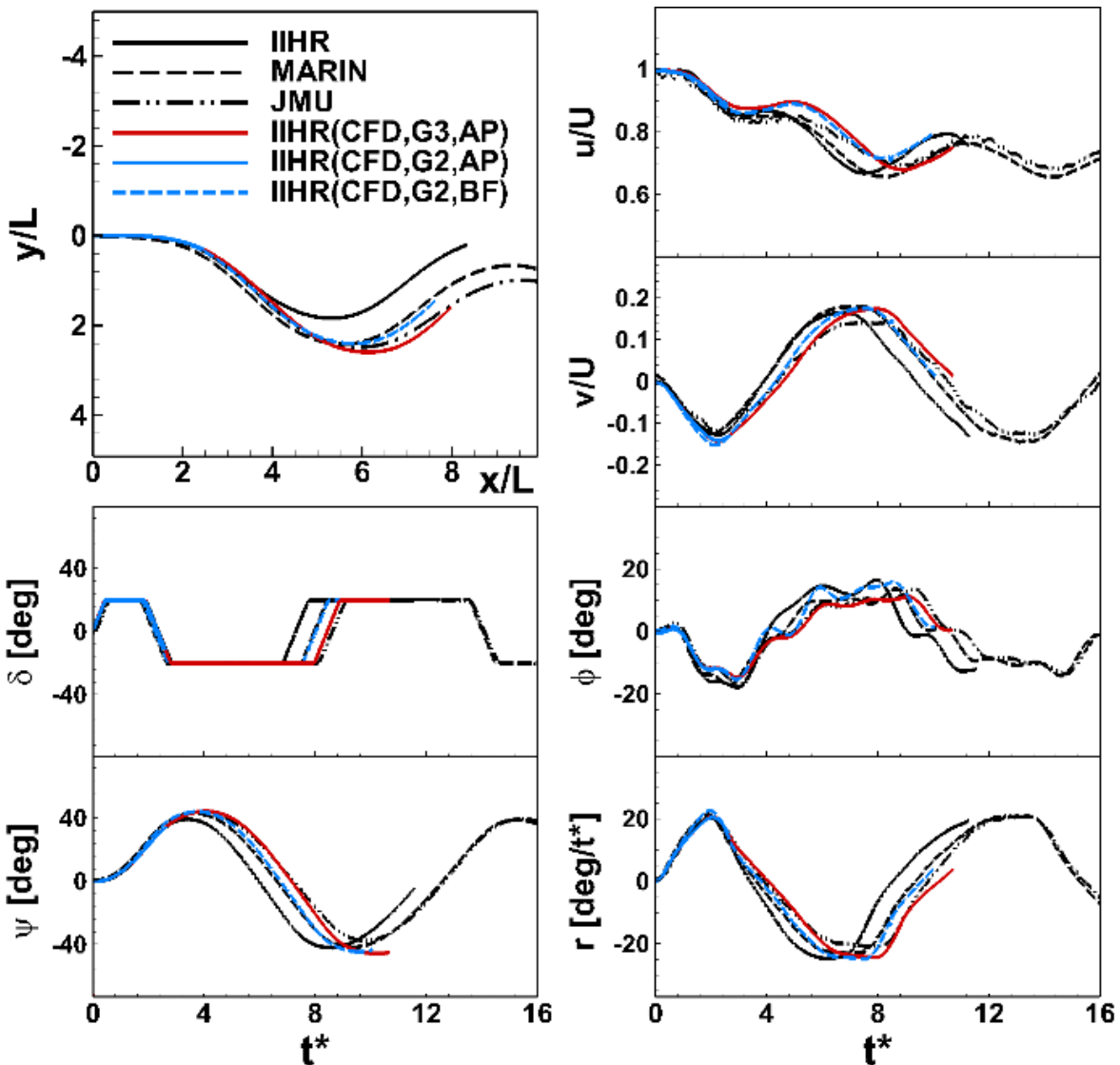


Figure 8-5. Time-histories from the  $+20^\circ/20^\circ$  zig-zag test

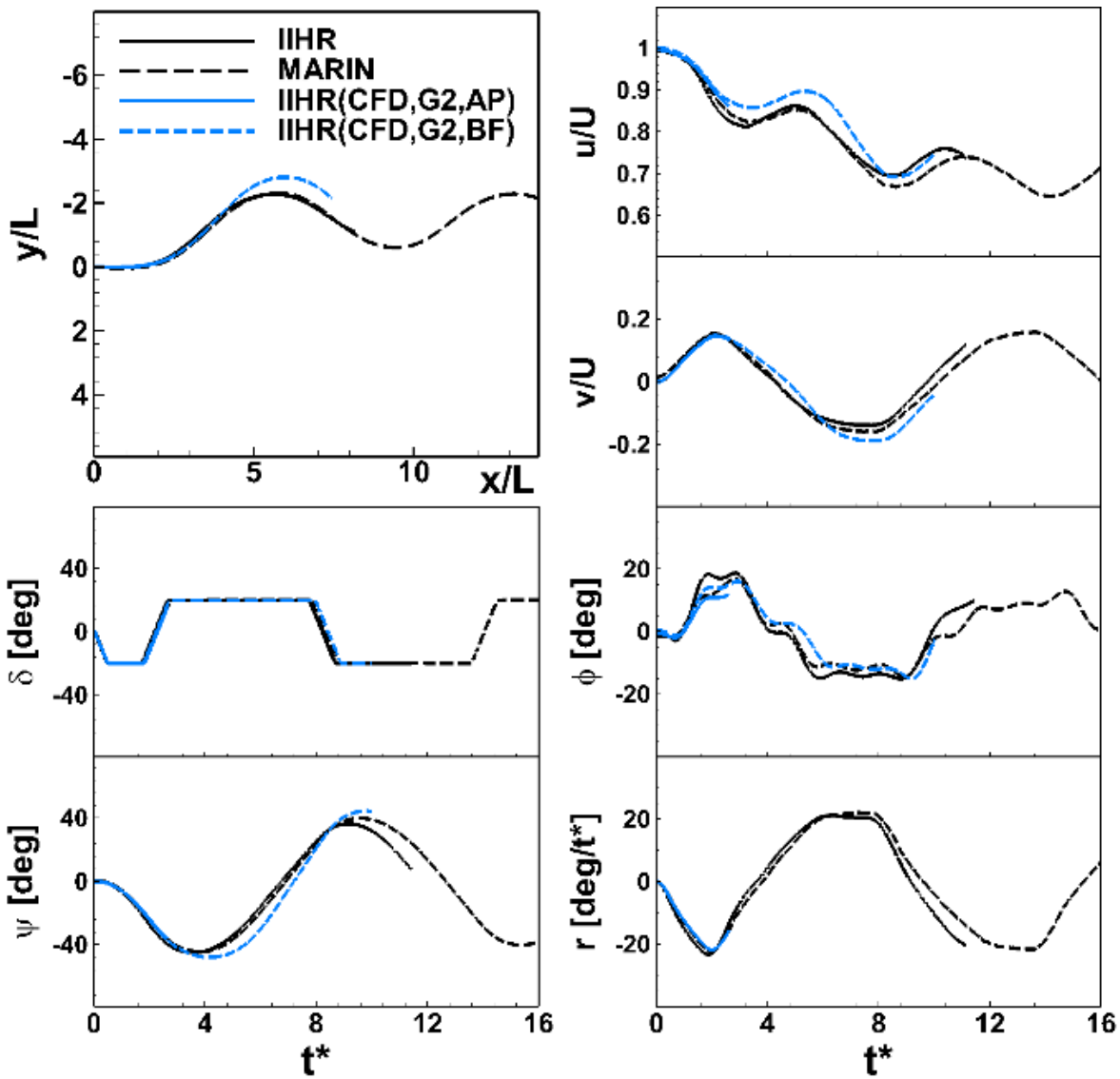


Figure 8-6. Time-histories from the  $-20^\circ/20^\circ$  zig-zag test

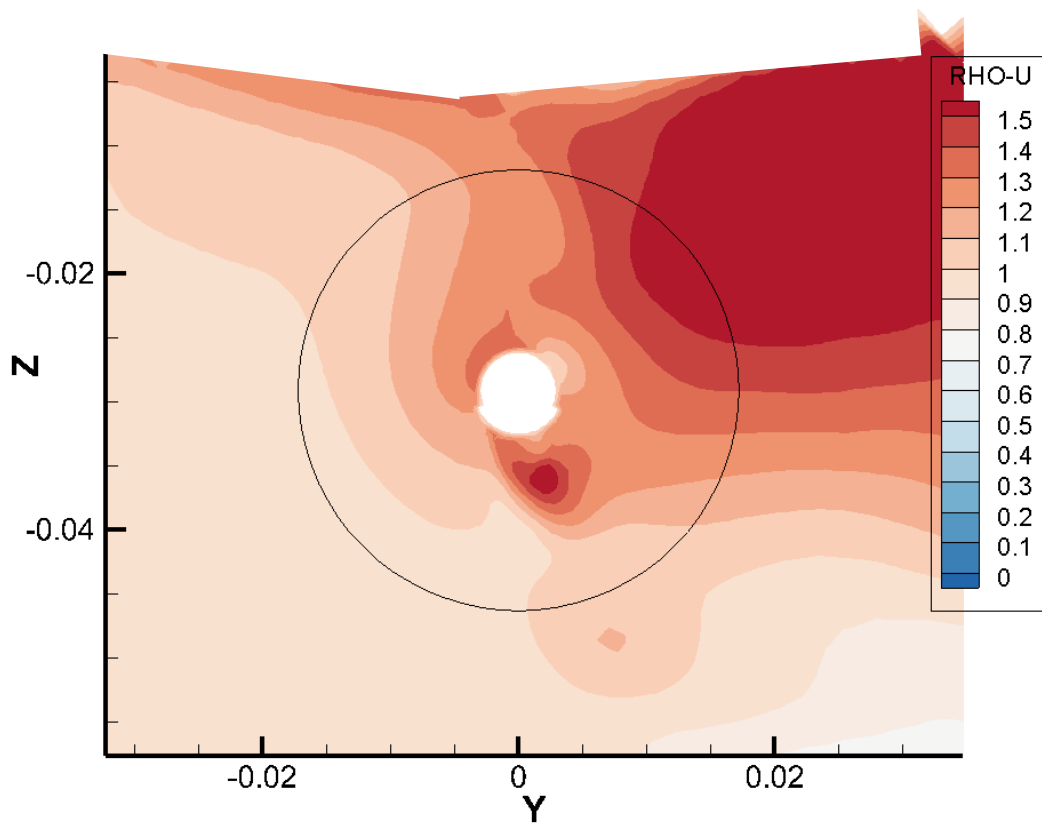


Figure 8-7. Effective wake field from the  $+35^\circ$  turning test ( $\psi > 210^\circ$ )

## 9. COURSE KEEPING IN REGULAR HEAD WAVES

### 9.1. Self-propulsion Test

#### 9.1.1. 2DOF Captive Self-propulsion Test

##### Objective and methodology

Self-propulsion test in waves ( $Fn = 0.26$ ) is performed prior to the course-keep tests in order to find the propeller rotational speed that needs to be increased in the wave conditions. The self-propulsion test in waves is initially performed with a 2DOF captive condition for faster convergence compared to the 6DOF condition. Both BF and AP models are used for G2 and G3. Three different propeller rotational speeds are used for each wave length condition:  $n_{calm}$ ,  $n_{calm} + \Delta n$  and  $n_{calm} + 2\Delta n$ , where  $n_{calm}$  is the converged propeller rotational speed from the calm water self-propulsion test,  $\Delta n$  [1/s] is 0.5 for  $\lambda/L = 0.65$ , 1 for  $\lambda/L = 0.85$ , 2 for both  $\lambda/L = 1.00$  and 1.15, and lastly 3 for both  $\lambda/L = 1.37$  and 1.95.  $\Delta n$  is a rough estimate by checking the added-resistance trend (Sadat-Hosseini et al. 2015). The mean total resistance coefficient is obtained when each propeller rotational speed is used, and the linear regression curve is fitted against the ratio of the propeller rotational speed (in waves) to the propeller rotational speed found in calm water SP ( $=n_{wave}/n_{calm}$ ). Then, the point where the mean total resistance becomes zero is found from the regression curve so that the course-keeping test can be initiated. The reason of using the ratio is due to the consistently shifted propeller rotational speed predicted when BF model is in use.

##### Validation

Table 9-1 and Figure 9-1 shows the validation results of the propeller rotational speeds using the regression curve at each wave length. The  $E\%D$  of  $n_{wave}$  (or  $n_{wave}/n_{calm}$  for BF

model) are very similar to  $E\%D$  of  $n_{calm}$  shown in the calm water self-propulsion test. The averaged  $E\%D$  are 16.5% and 3.7% in average for BF and AP model, respectively.

### **9.1.2. 6DOF Free-running Self-propulsion Test**

#### **Objective and methodology**

Due to the motion constraints, the propeller rotational speed determined in 2DOF simulations often fails to put the ship at target mean  $Fn$  ( $=0.26$ ) when the value is used for 6DOF course-keeping test. Thus, the 6DOF SP test in waves is performed to adjust the value if the aforementioned issue occurs. The process of adjustment is to simply decrease/increase the propeller rotational speed manually/iteratively until the ship reaches to the target mean  $Fn$ , which is the same procedure performed in the experiment. The setup besides decreasing/increasing the propeller rotational speed are the same as the normal course-keeping test: rudder is PID controlled to keep the course; all motions are free.

#### **Validation**

Table 9-1 and Figure 9-1 shows the validation results of the 6DOF self-propulsion test in waves. Whenever the propeller rotational speed is adjusted by 6DOF self-propulsion test in waves, the results are named as “RPS adjusted” followed by the name of the propulsion model. For AP model, 6DOF self-propulsion test in wave is performed for  $\lambda/L = 0.65, 0.85, 1.00$  and  $1.15$  where the propeller rotational speed obtained from 2DOF self-propulsion test showed large mean  $Fn$  discrepancies during the course-keeping test. During the test, only a single iteration is required for  $\lambda/L = 0.65$  and  $0.85$  wave conditions while two iterations are required for  $\lambda/L = 1.00$  and  $1.15$  conditions, respectively, to achieve the reasonably mean  $Fn$ . For BF model, the test is only performed for  $\lambda/L = 1.15$ . The initial increment/decrement (depending on loss/gain of mean  $Fn$  during the course-keeping test) of the propeller rotational speed is  $0.5$  [1/s], and a smaller value is

used when mean  $F_n$  is close to the target. The final propeller rotational speeds determined from the 6DOF SP test show much closer mean  $F_n$  to the target value ( $=0.26$ ), and the  $E\%D$  of the propeller rotational speeds are closer to  $E\%D$  from calm water self-propulsion test.

## 9.2. Course Keeping in Regular Head Wave

### 9.2.1. Time-history

Figure 9-2 to 9-7 shows trajectories and time-histories of wave elevation, motions, thrust and torque coefficients, propeller rotational speed and PID controlled variables for  $\lambda/L = 0.65, 0.85, 1.15, 1.37$  and  $1.95$  conditions. For every case, both BF and AP model are used.

#### Motions

The agreement for heave, pitch and the ship speed are satisfactory for both AP and BF models. Trajectory, roll angle, yaw angle and the rudder angle often show differences with IIHR since the side force in the head wave condition is not large enough which may only induce small perturbations. For BF model, the trajectory is always straight due to the axisymmetric propulsion model. Both AP and BF models often show the fluctuation of the ship speed while IIHR does not show any fluctuation whose reason is still under investigation.

#### Thrust, torque and propeller rotational speed

It can be easily checked that the signals of the thrust and torque do not contain higher harmonics ( $>$ first harmonics) unlike the total resistance signal previously checked from the added-resistance test under constraint (Sadat-Hosseini et al. 2015). AP model shows good agreement for the thrust/torque coefficients and propeller rotational speed; however BF shows large gap against IIHR (especially the zeroth harmonic) due to the propulsion model whose issue is already covered in Chapter 7. Additionally, BF model does not show thrust and torque fluctuations which is found

to be relevant to the fluctuation of the propeller inflow as it will be discussed later. The AP model's high frequency noises on the thrust/torque signals are due to the high data collecting rate (2500Hz). Note that the torque signals of the simulations shown in the time-history did not undergo the adjustment explained in Chapter 7 and are respect to the center of gravity of the ship, therefore, the zeroth and first harmonic amplitudes are not exactly the same as those will be shown in RAO section, which has adjusted values, and the time-histories of the torque should be used only to check the first harmonic phase which is less likely affected by the adjustment.

### 9.2.2. Validation of the Zeroth Harmonic Amplitude

Figures 9-8 and 9-9 show RAOs of zeroth harmonic amplitude for heave, pitch and thrust/torque coefficients. Table 9-2 shows the  $E\%D$  for all variables.

The first harmonic amplitude of the wave elevation used to formulate the RAOs of motions is obtained from the wave elevation signal obtained from the wave probe located 0.5m away from the model ship's FP (to the starboard) at each facility. More discussions on the difference of values obtained from each experiment facility is explained in Sanada et al. (2018). To compare the wave elevation (disturbed by ship motion), simulation had to put the wave probe at the same location and extract the height where level-set variable becomes zero (in case of VOF model, the location should be a point where the volume fraction becomes 0.5). However, the disturbance by ship motions on the wave elevation is not considered in the current study and assumes the zeroth harmonic amplitude as zero and first harmonic amplitude as one.

#### Motions

In figure 9-8, RAO of the heave shows the same trend as the one from added-resistance test (Sadat-Hosseini et al. 2015). The trend shows the decrease of magnitude as the wave becomes long wave, and it matches with the experiment closely. The averaged  $E\%D$  over the wave length

is 6.3% for BF model and 5.9% for AP model when both models use the propeller rotational speed that gives out the closest mean  $F_n$  to the target value ( $=0.26$ ). The magnitudes of the pitch RAO from the current course-keeping tests are much smaller compared to the added-resistance test. The averaged  $E\%D$  for the pitch RAO is 163.7% for BF model and 160.3% for AP model. Further uncertainty analysis is required to complete the validation. Due to the weak side force in the head wave condition, the validation on the other motions relevant to the side are not presented.

### **Thrust and torque**

The peaks of both thrust and torque coefficient RAOs locate at  $\lambda/L = 1.15$  like the added-resistance test. However, the difference between these two setup arises in the long wave condition ( $\lambda/L = 1.37, 1.95$ ) where the magnitudes from the current course-keeping test do not drop from the peak as much as it does in the short wave ( $\lambda/L = 0.65, 0.85$ ), which indicates that the effect of the propeller is more prominent during the long wave condition compared to the condition that does not equip the propeller. The average  $E\%D$  for thrust and torque coefficients are 20.2% and 12.0% for BF and 4.0% and 5.8% for AP.

#### **9.2.3. Validation of the First Harmonic Amplitude**

Figures 9-10 to 9-11 show RAOs of the first harmonic amplitude for heave, pitch and thrust/torque coefficients. Table 9-3 shows the corresponding  $E\%D$ .

### **Motions**

In Figure 9-10, the RAO trend of the first harmonic amplitude of heave and pitch resemble the ones from the added-resistance test results and show the increase of excitement as the increase of wave length. Both values stay near one in the long wave conditions. The averaged  $E\%D$  for the RAO of heave is 29.3% for BF model and 9.6% for AP model. BF model noticeably fails to predict

the heave near resonance condition due to the inaccurate propulsion modelling which might have affected the pressure distribution near the hull.  $E\%D$  for the RAO of pitch is predicted reasonably for both BF and AP models: 13.5% and 5.8%, respectively.

### **Thrust and torque**

As shown in Figure 9-11, the first harmonic amplitudes of thrust and torque coefficients are in relatively good agreement between the IIHR and the AP model. The  $E\%D$  for the RAO of the thrust coefficient is 22.9% in average. The study for the thrust excitement will be discussed later. The  $E\%D$  for the RAO of torque coefficient for AP model is 17.7% in average. The  $E\%D$  for BF model exceeds 78% for both variables.

#### **9.2.4. Validation of the First Harmonic Phase**

Figures 9-12 to 9-13 shows the RAOs of the first harmonic phases for motions and thrust/torque coefficients. Table 9-4 shows the respective  $E\%2\pi$ . The first harmonic phases are obtained respect to the wave signal measured at the FP, which is the same condition as the added-resistance test.

### **Motions**

The agreement between the experiment and CFD is close for the RAOs of heave and pitch: 5.3% and 3.0%  $E\%2\pi$  for BF model and 5.5% and 3.4%  $E\%2\pi$  for AP model. Both RAOs of heave and pitch experience gradual decrease as the wave length increases.

### **Thrust and torque**

BF model's prediction accuracy for the RAOs of thrust and torque is low: 30.4% and 30.9%  $E\%2\pi$ . BF model shows almost 90-degree phase lack for both thrust and torque near the resonance

and the short wave conditions. AP shows close agreements by showing 2.7% and 8.2% E% $2\pi$ . RAOs of thrust and torque also show gradual decrease as the wave length increases.

### 9.2.5. Added Powering Variables

Figures 9-14 shows the RAOs of the added-powering variables. Table 9-5 shows the  $E\%D$ . Due to having consistent  $E\%D$  for thrust/torque coefficients and the propeller rotational speed in both calm water and wave conditions, the prediction accuracies for added powering variables are good especially for AP model.

#### **Added thrust, added torque and added propeller rotational speed**

The averaged  $E\%D$  for the added thrust ( $\tau_{AW}$ ) is 26.6% for BF model and 11.2% for AP model. For the added torque ( $\kappa_{AW}$ ), the averaged  $E\%D$  remains at 33.9%  $E\%D$  for BF model, however, the AP model only shows 9.4%. When the added propeller rotational speed ( $v_{AW}$ ) is compared, AP model shows 8.8% while BF model shows 20.5%. RAOs trends for the added thrust and added torque variables resemble the total resistance trend from the added-resistance test closely.

#### **Fluctuation of thrust and torque**

Thrust fluctuation ( $\tau_{AF}$ ) is in good agreement against IIHR for AP model. The  $E\%D$  is 11.7% in average. The prediction for the torque fluctuation ( $\kappa_{AF}$ ) for AP model shows  $E\%D$  of 14.6% in average. BF model fails to predict the fluctuations by showing more than 73%  $E\%D$  for both variables.

### 9.2.6. Self-propulsion Factors

In Table 9-6 and Figure 9-15 to 16, the zeroth harmonic amplitude, the first harmonic amplitude and the first harmonic phase of the advance coefficient,  $1 - \omega_e$ , propeller efficiency

behind the effective wake ( $\eta_0$ ) and relative rotational efficiency ( $\eta_R$ ) are presented. Figure 16 additionally shows second harmonic amplitudes of  $1 - \omega_e$  and the  $\eta_0$ . The values are estimated based on two different methods: (1) thrust identification using the mean thrust (both experiment and CFD); (2) direct calculation from the flow field (CFD only). For the second method, the effective wake fraction is obtained at V1 slice at the rate of 625Hz, then, the time-history is formulated and the fast fourier transform (FFT) analysis is performed. Only AP model is used during the current validation. For the best estimation, cases showing mean  $Fn$  closest to 0.26 are selected like done for the formulation of the RAO.

### **Effective wake fraction**

The averaged (over wavelength)  $1 - \omega_e$  calculated from the thrust identification method are 0.736 for the IIHR and 0.667 for the CFD. The  $E\%D$  is 9.2%. The averaged  $1 - \omega_e$  by using direct calculation is 0.841. Since the direct calculation of the effective wake fraction is considered more accurate than the thrust identification method, and since the difference is noticeably large, it is noteworthy that the thrust identification method fails to calculate the  $1 - \omega_e$  by -26% accuracy for the current KCS model when comparing the method 1 and 2 results (within CFD results). Thrust identification method is assuming the uniform propeller inflow similar as the POT during the process, and thus, the adoption of the method for the single-screw ship seems invalid when calculating the effective wake fraction. The RAO of the zeroth harmonic amplitude of the  $1 - \omega_e$  obtained from the direct measurement shows similar trend as the RAOs of zeroth harmonic amplitude of thrust and propeller rotational speed while the peak value stays at  $\lambda/L = 1.37$ . The first and second harmonic amplitudes of the  $1 - \omega_e$  increases as the wavelength increases. The first harmonic amplitude reaches up to 4% in the longest wavelength condition. The first harmonic phase increases gradually as the wavelength increases.

### **Propeller efficiency**

The average (over wavelength) of the  $\eta_0$  are 0.46 and 0.452 for the IIHR and the CFD, respectively, when the thrust identification method is both used. The  $E\%D$  is 2.0% in average. The RAO shows the efficiency of the propeller becomes the lowest at the  $\lambda/L = 1.15$  condition. The direct calculation method shows almost the same trend as the thrust identification method. However, the large difference is shown during the short wave conditions. Thrust identification does not involve the effective wake fraction calculation during the efficiency calculation and seems valid for efficiency calculation: the method simply finds the torque at the same advance coefficient where the thrust becomes the same and calculate the ratio of the thrust and the torque, however, more investigation seems required to sort out the point where the thrust identification fails.

### **Relative rotative efficiency**

The relative rotative efficiency is in good agreement between the IIHR and the CFD (5.5%  $E\%D$  in average). The trend for the relative rotative efficiency is not confirmed.

#### **9.2.7. Relative Motions**

Figure 9-17 shows the relative motions of FP and AP. The relative motions are calculated based on the equations from Sadat-Hosseini et al. (2015). The results show that the difference of FP and AP relative motions become the largest at the resonance condition. The phase difference becomes almost 180° at the same condition.

#### **9.2.8. Location of the Added-resistance**

In Figure 9-18 and 9-19, the longitudinal distributions of the mean hydrodynamic resistances on the bare-hull are compared with the calm water self-propulsion result. The mean hydrodynamic resistance is larger near the bow for the wave case and is balancing with the pressure

drop of the actuating propeller. The standard deviation of hydrodynamic resistance is larger at bow region than the stern region. The midship region show relatively little amount of fluctuation.

### **9.2.9. Local Flow**

Figure 9-20 shows the comparison of local flow measurements between G3-AP and OU PIV. Since the measurement coordinate was at the carriage, which is the same condition as the calm water self-propulsion test case, the PIV measurement and the CFD results are showing large motion responses due to the wave. The OU PIV results were done by phase-averaging in waves. The G3-AP results are lacking the prediction accuracy on the wake magnitude due to the insufficient resolution near the rudder as discussed in the calm water self-propulsion test. The phase difference between the experiment and the CFD is reasonably small.

Table 9-1. Validation of propeller rotational speed for the SP tests in head waves

Var.	$\lambda/L$	D	S				(D-S)%D			
		IIHR (L=2.7m)	BF, G2		AP, G3		BF, G2		AP, G3	
			2DOF	6DOF	2DOF	6DOF	2DOF	6DOF	2DOF	6DOF
$n_{calm}$ [RPS]		19.0	22.03		18.14		<b>-16.0</b>		<b>4.6</b>	
$n_{wave}$ [RPS]	0.65	19.5	22.36		18.36	18.61	-14.6		5.8	4.5
	0.85	20.5	23.42		19.19	19.58	-14.2		6.4	4.5
	1.00	22.0	25.81		21.27	20.81	-17.3		3.3	5.4
	1.15	23.0	28.01	26.73	23.00	22.04	-21.8	-16.2	0.0	4.2
	1.37	23.0	26.56		21.95		-15.5		4.6	
	1.95	21.0	24.24		20.52		-15.4		2.3	
	Ave.						<b>16.5</b>	<b>16.2</b>	<b>3.7</b>	<b>4.6</b>
$n_{wave}/n_{calm}$	0.65	1.026	1.015		1.012	1.026	1.1		1.4	0.03
	0.85	1.079	1.063		1.058	1.079	1.5		2.0	-0.02
	1.00	1.158	1.171		1.172	1.147	-1.2		-1.2	0.9
	1.15	1.211	1.271	1.213	1.268	1.215	-5.0	-0.2	-4.7	-0.4
	1.37	1.211	1.205		1.210		0.4		0.1	
	1.95	1.105	1.100		1.131		0.5		-2.3	
	Ave.						<b>1.6</b>	<b>0.2</b>	<b>2.0</b>	<b>0.3</b>

Table 9-2. Validation of 0th harm. amp. for CK tests in head waves

Case	$\lambda/L$	$z_0/\zeta_1$	$\theta_0/\zeta_1 k$	$K_{TB,0}$	$K_{QB,0}$
D	0.65	-0.341	-0.0159	0.252	0.041
	0.85	-0.259	-0.0055	0.260	0.042
	1.00	-0.219	-0.0053	0.268	0.043
	1.15	-0.164	-0.0386	0.283	0.044
	1.37	-0.124	-0.0207	0.280	0.044
	1.95	-0.094	-0.0486	0.260	0.042
S (BF)	0.65	-0.359	-0.0324	0.188	0.034
	0.85	-0.258	-0.0140	0.202	0.036
	1.00	-0.217	0.0017	0.222	0.039
	1.15	-0.129	0.0608	0.235	0.040
	1.37	-0.128	0.0367	0.229	0.039
	1.95	-0.101	-0.0200	0.206	0.037
S (AP)	0.65	-0.369	-0.0397	0.260	0.043
	0.85	-0.266	-0.0300	0.266	0.044
	1.00	-0.205	-0.0086	0.276	0.045
	1.15	-0.151	0.0030	0.294	0.047
	1.37	-0.128	0.0071	0.293	0.047
	1.95	-0.088	-0.0161	0.278	0.044
$E\%D$ (BF)	0.65	-5.2	-103.2	25.5	16.7
	0.85	0.2	-154.0	22.3	14.0
	1.00	0.9	131.8	17.2	9.7
	1.15	21.3	257.6	17.1	9.3
	1.37	-3.5	277.0	18.2	10.4
	1.95	-7.1	58.9	20.6	11.9
	Ave.	<b>6.3</b>	<b>163.7</b>	<b>20.2</b>	<b>12.0</b>
$E\%D$ (AP)	0.65	-8.1	-149.0	-3.0	-4.2
	0.85	-2.9	-444.2	-2.3	-4.8
	1.00	6.4	-59.9	-3.0	-5.7
	1.15	7.8	107.7	-3.8	-6.4
	1.37	-3.5	134.2	-4.6	-6.7
	1.95	6.7	66.9	-7.1	-7.0
	Ave.	<b>5.9</b>	<b>160.3</b>	<b>4.0</b>	<b>5.8</b>

Table 9-3. Validation of 1st harm. amp. for CK tests in head waves

Case	$\lambda/L$	$z_1/\zeta_1$	$\theta_1/\zeta_1 k$	$K_{TB,1}$	$K_{QB,1}$
D	0.65	0.112	0.017	0.0035	0.0004
	0.85	0.258	0.260	0.0107	0.0015
	1.00	0.579	0.499	0.0144	0.0020
	1.15	0.858	0.789	0.0136	0.0019
	1.37	0.872	1.035	0.0233	0.0031
	1.95	0.873	1.112	0.0365	0.0047
S (BF)	0.65	0.132	0.021	0.0010	0.0001
	0.85	0.323	0.294	0.0020	0.0003
	1.00	0.923	0.597	0.0015	0.0002
	1.15	1.280	0.925	0.0008	0.0001
	1.37	1.050	1.110	0.0054	0.0007
	1.95	0.906	1.110	0.0158	0.0020
S (AP)	0.65	0.123	0.020	0.0054	0.0006
	0.85	0.239	0.239	0.0141	0.0017
	1.00	0.634	0.494	0.0131	0.0015
	1.15	0.975	0.787	0.0163	0.0022
	1.37	0.970	1.030	0.0280	0.0033
	1.95	0.921	1.080	0.0370	0.0045
$E\%D$ (BF)	0.65	-18.3	-23.8	70.0	70.0
	0.85	-25.0	-13.0	81.0	82.3
	1.00	-59.4	-19.7	89.7	90.5
	1.15	-49.2	-17.2	93.9	94.4
	1.37	-20.4	-7.2	77.0	78.3
	1.95	-3.8	0.1	56.7	57.8
	Ave.	<b>29.3</b>	<b>13.5</b>	<b>78.1</b>	<b>78.9</b>
$E\%D$ (AP)	0.65	-10.2	-22.0	-55.0	-38.7
	0.85	7.5	8.2	-31.8	-16.2
	1.00	-9.5	1.0	9.0	25.0
	1.15	-13.7	0.3	-19.9	-16.1
	1.37	-11.2	0.5	-20.2	-6.8
	1.95	-5.5	2.8	-1.4	3.3
	Ave.	<b>9.6</b>	<b>5.8</b>	<b>22.9</b>	<b>17.7</b>

Table 9-4. Validation of 1st harm. phases for CK tests in head waves

Case	$\lambda/L$	$\varepsilon_{z1}$	$\varepsilon_{\theta1}$	$\varepsilon_{TB,1}$	$\varepsilon_{QB,1}$
D	0.65	2.37	0.62	0.20	0.37
	0.85	1.98	2.44	1.94	1.98
	1.00	2.62	-3.03	3.01	3.02
	1.15	-2.95	-2.35	-3.00	-3.00
	1.37	-2.04	-1.33	-2.48	-2.44
	1.95	-1.51	-0.30	-1.01	-1.01
S (BF)	0.65	1.59	0.57	-2.76	-2.76
	0.85	1.36	2.05	4.16	4.16
	1.00	2.29	-3.26	4.66	4.66
	1.15	-3.03	-2.49	0.00	0.00
	1.37	-2.21	-1.59	-3.10	-3.10
	1.95	-1.54	-0.36	0.00	0.00
S (AP)	0.65	1.72	0.66	0.12	1.46
	0.85	1.62	2.16	1.77	1.19
	1.00	2.26	-3.27	2.88	2.13
	1.15	-3.15	-2.51	-3.26	-3.05
	1.37	-2.34	-1.63	-2.62	-2.19
	1.95	-1.72	-0.55	-1.24	-0.98
$E\%2\pi$ (BF)	0.65	12.4	0.7	47.1	49.9
	0.85	9.9	6.2	-35.4	-34.7
	1.00	5.2	3.7	-26.3	-26.1
	1.15	1.2	2.3	-47.8	-47.8
	1.37	2.7	4.1	9.9	10.6
	1.95	0.5	1.0	-16.0	-16.1
	Ave.	<b>5.3</b>	<b>3.0</b>	<b>30.4</b>	<b>30.9</b>
$E\%2\pi$ (AP)	0.65	10.2	-0.7	1.2	-17.3
	0.85	5.7	4.4	2.7	12.6
	1.00	5.6	3.9	2.0	14.2
	1.15	3.1	2.6	4.1	0.7
	1.37	4.7	4.8	2.3	-3.9
	1.95	3.3	3.9	3.7	-0.5
	Ave.	<b>5.5</b>	<b>3.4</b>	<b>2.7</b>	<b>8.2</b>

Table 9-5. Validation of added-powering var. for CK tests in head waves

Case	$\lambda/L$	$v_{AW}$	$\tau_{AW}$	$\kappa_{AW}$	$\tau_{AF}$	$\kappa_{AF}$
D	0.65	1.247	1.200	0.189	0.357	0.050
	0.85	2.170	2.006	0.295	0.480	0.062
	1.00	3.162	2.920	0.436	0.402	0.054
	1.15	3.163	3.273	0.478	0.341	0.047
	1.37	2.231	2.244	0.330	0.430	0.056
	1.95	0.550	0.477	0.070	0.300	0.039
S (BF)	0.65	0.784	0.641	0.112	0.088	0.011
	0.85	1.970	1.980	0.318	0.110	0.014
	1.00	4.010	4.080	0.653	0.035	0.004
	1.15	3.750	4.170	0.657	0.032	0.004
	1.37	2.690	2.780	0.443	0.146	0.018
	1.95	0.608	0.577	0.094	0.173	0.022
S (AP)	0.65	1.140	1.100	0.116	0.314	0.035
	0.85	2.040	1.810	0.280	0.535	0.064
	1.00	2.850	2.560	0.438	0.403	0.047
	1.15	3.000	3.150	0.487	0.425	0.057
	1.37	2.100	2.180	0.343	0.510	0.062
	1.95	0.644	0.622	0.075	0.292	0.035
$E\%D$ (BF)	0.65	37.1	46.6	40.9	75.5	77.8
	0.85	9.2	1.3	-7.7	77.1	77.6
	1.00	-26.8	-39.7	-49.8	91.2	91.7
	1.15	-18.6	-27.4	-37.5	90.7	91.4
	1.37	-20.6	-23.9	-34.3	66.1	67.8
	1.95	-10.6	-20.9	-33.2	42.3	43.8
	Ave.	<b>20.5</b>	<b>26.6</b>	<b>33.9</b>	<b>73.8</b>	<b>75.0</b>
$E\%D$ (AP)	0.65	8.6	8.3	38.7	12.1	28.8
	0.85	6.0	9.8	5.2	-11.6	-4.7
	1.00	9.9	12.3	-0.4	-0.3	11.5
	1.15	5.1	3.8	-2.0	-24.5	-23.0
	1.37	5.9	2.8	-4.0	-18.7	-9.5
	1.95	-17.1	-30.4	-6.3	2.8	10.2
	Ave.	<b>8.8</b>	<b>11.2</b>	<b>9.4</b>	<b>11.7</b>	<b>14.6</b>

Table 9-6. Validation of SP factors for CK tests in head waves

Case	$\lambda/L$	Thrust Identification			Direct calculation	
		$(1 - w_e)_0$	$(\eta_0)_0$	$(\eta_R)_0$	$(1 - w_e)_0$	$(\eta_0)_0$
D	0.65	0.707	0.482	1.060		
	0.85	0.723	0.471	1.070		
	1.00	0.753	0.459	1.070		
	1.15	0.740	0.435	1.070		
	1.37	0.750	0.440	1.070		
	1.95	0.742	0.471	1.073		
	Ave	<b>0.736</b>	<b>0.460</b>	<b>1.069</b>		
S (AP)	0.65	0.647	0.474	1.005	0.801	0.594
	0.85	0.667	0.469	1.007	0.827	0.590
	1.00	0.670	0.448	1.008		
	1.15	0.656	0.421	1.014	0.864	0.568
	1.37	0.658	0.424	1.011	0.874	0.575
	1.95	0.711	0.475	1.016	0.840	0.573
	Ave	<b>0.668</b>	<b>0.452</b>	<b>1.010</b>	<b>0.841</b>	<b>0.580</b>
$E\%D$ (AP)	0.65	8.4	1.6	5.1		
	0.85	7.7	0.5	5.9		
	1.00	11.1	2.4	5.8		
	1.15	11.4	3.3	5.3		
	1.37	12.3	3.7	5.5		
	1.95	4.2	-0.7	5.3		
	Ave	<b>10.6</b>	<b>2.2</b>	<b>5.5</b>		

Table 9-7. AoAs for the different z-positions

Slice (z/L)	$\Delta x/L$	$\Delta y/L$	AoA
H1 (0.0172)	0.989563	-0.00059	<b>3.22</b>
H2 (0.0086)	0.98989	-0.00065	<b>3.68</b>
H4 (-0.0086)	0.990694	8.52E-05	<b>-0.52</b>

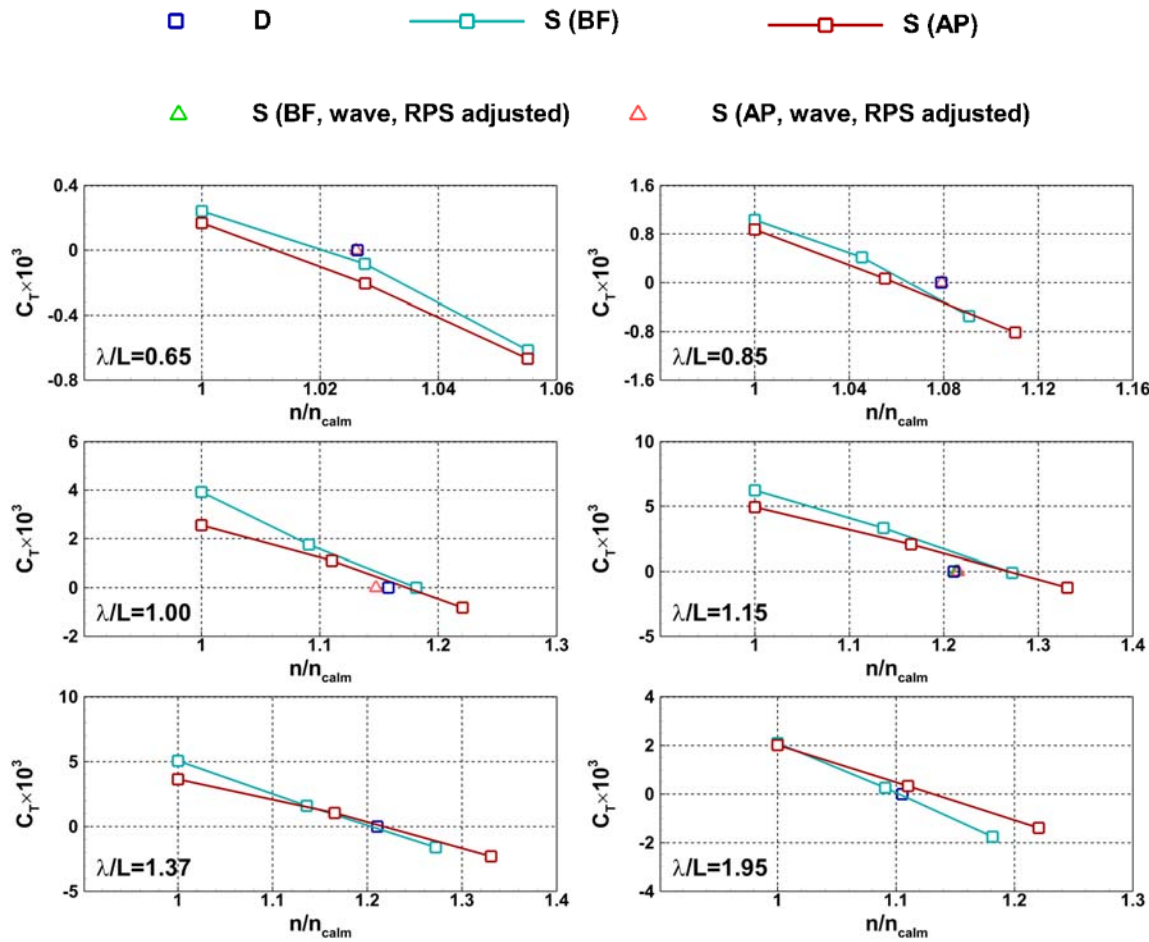


Figure 9-1. Validation results for SP tests in head waves

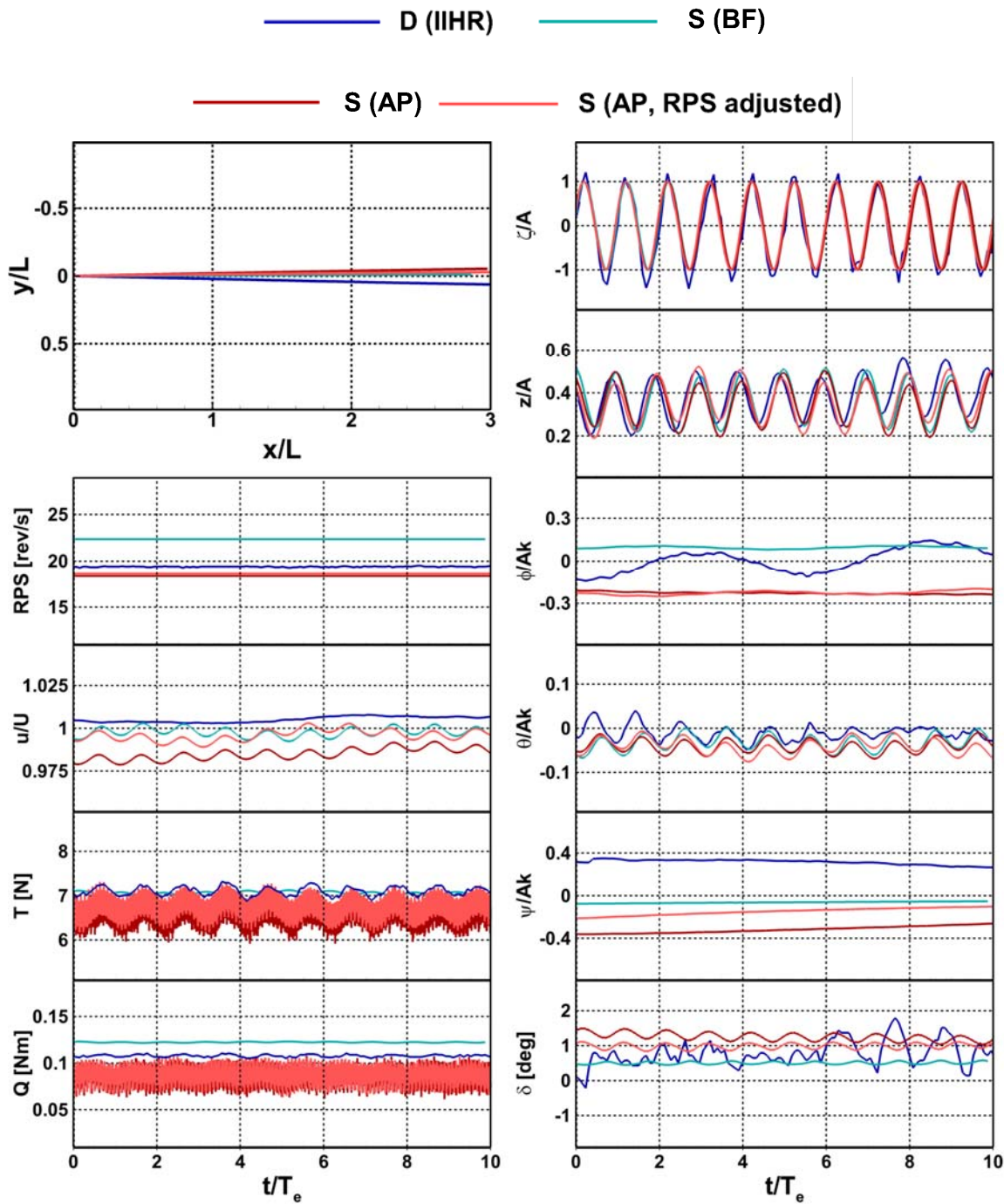


Figure 9-2. Time-histories from the CK test in head wave ( $\lambda/L=0.65$ )

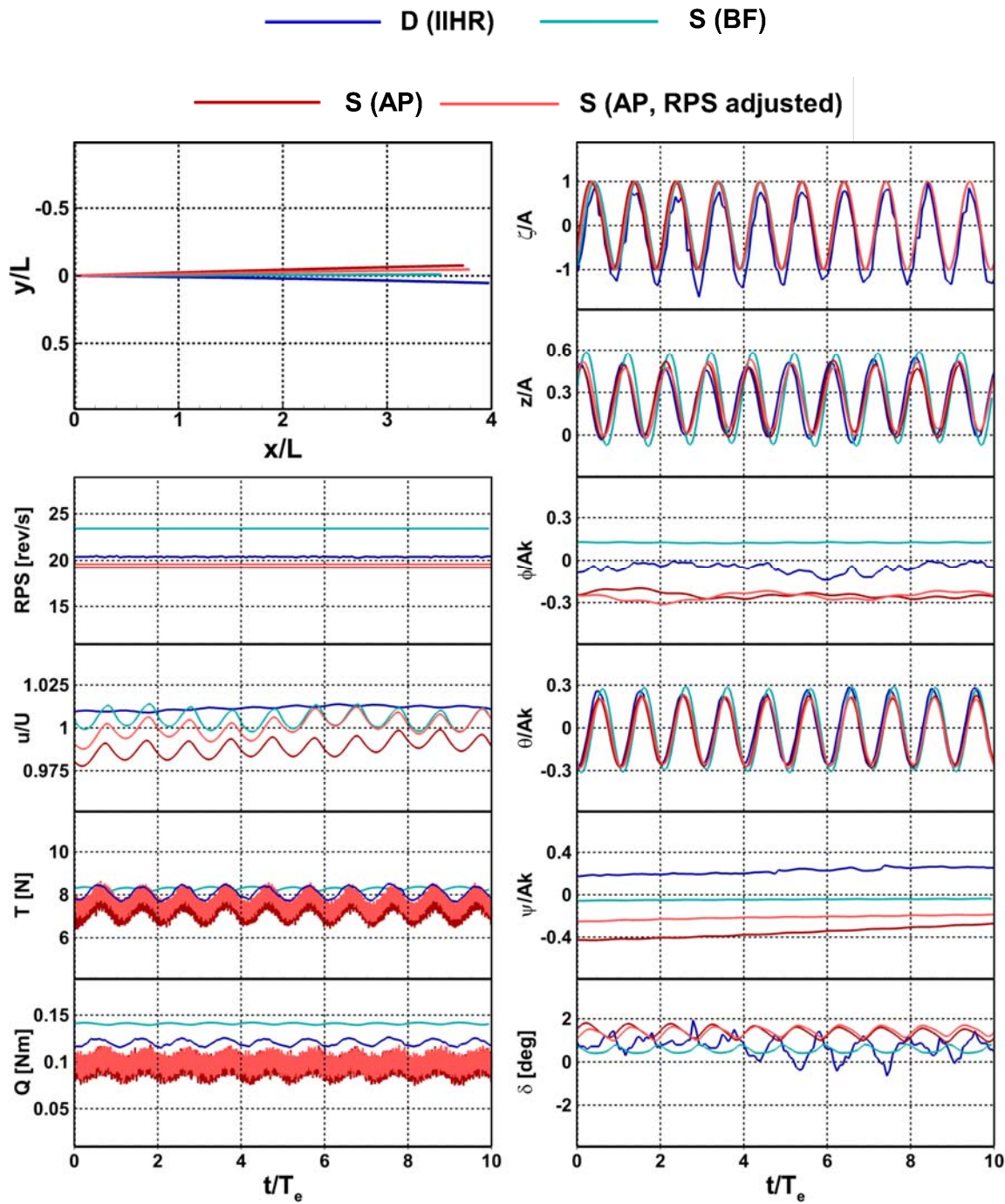


Figure 9-3. Time-histories from the CK test in head wave ( $\lambda/L=0.85$ )

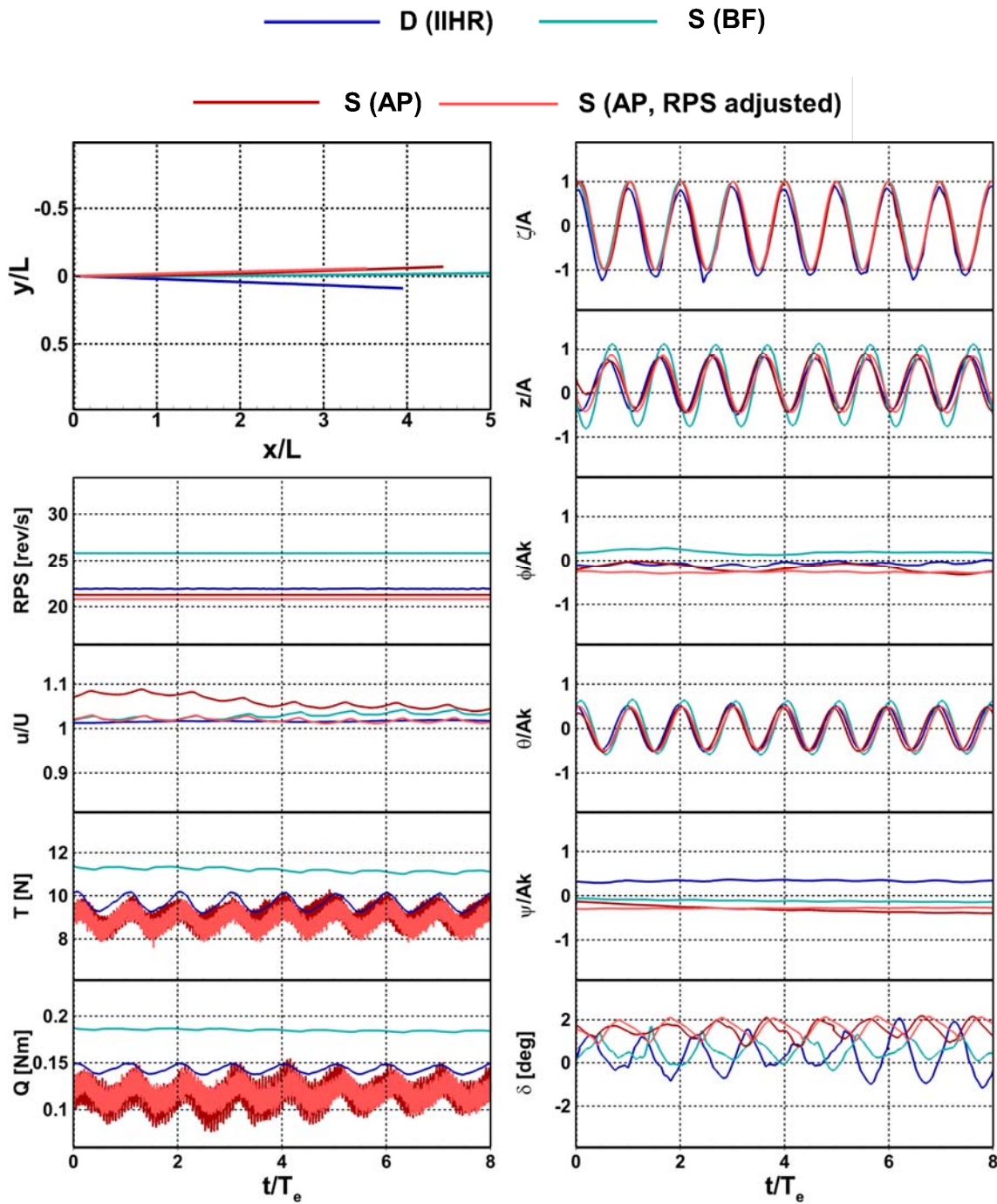


Figure 9-4. Time-histories from the CK test in head wave ( $\lambda/L=1.00$ )

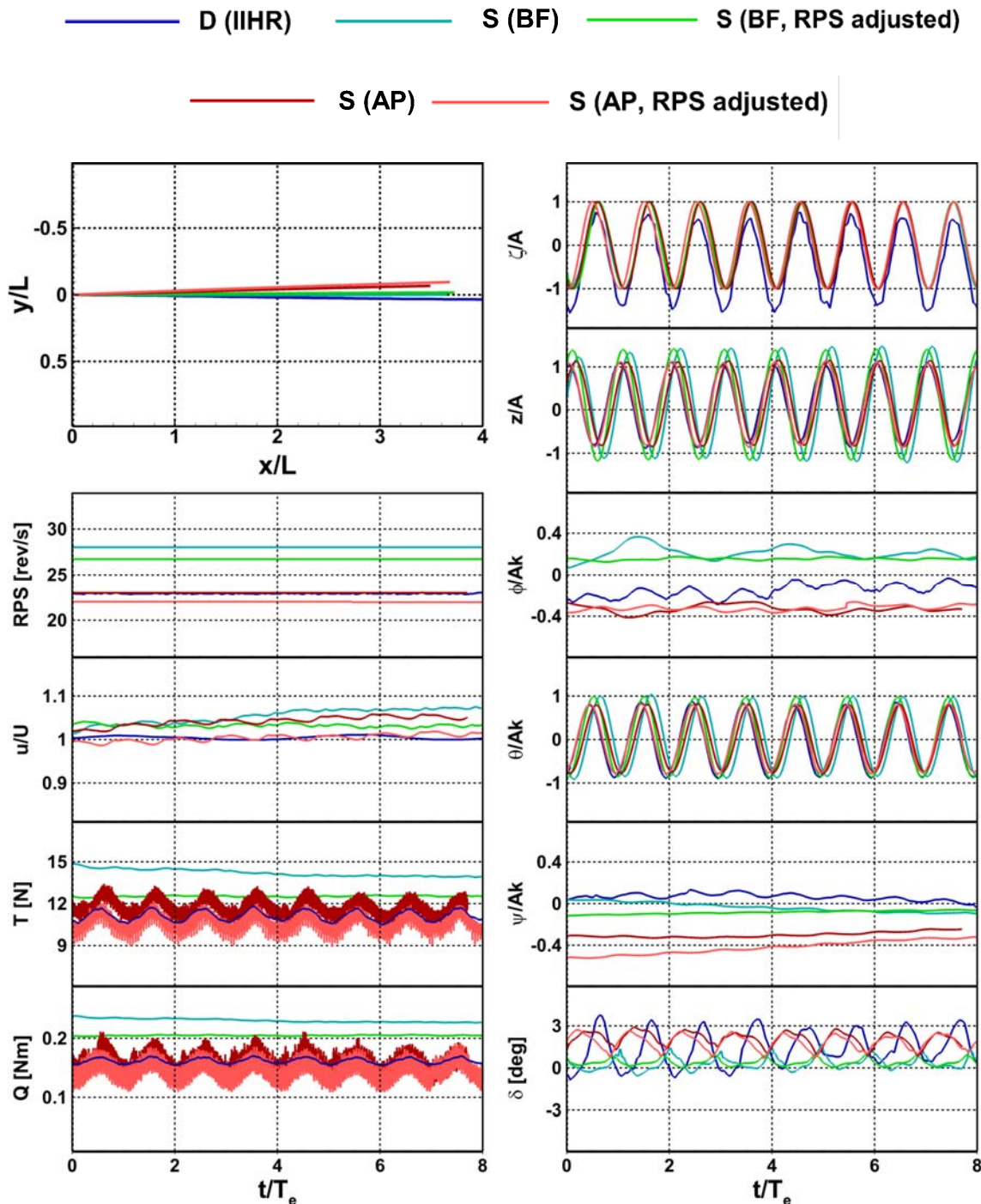


Figure 9-5. Time-histories from the CK test in head wave ( $\lambda/L=1.15$ )

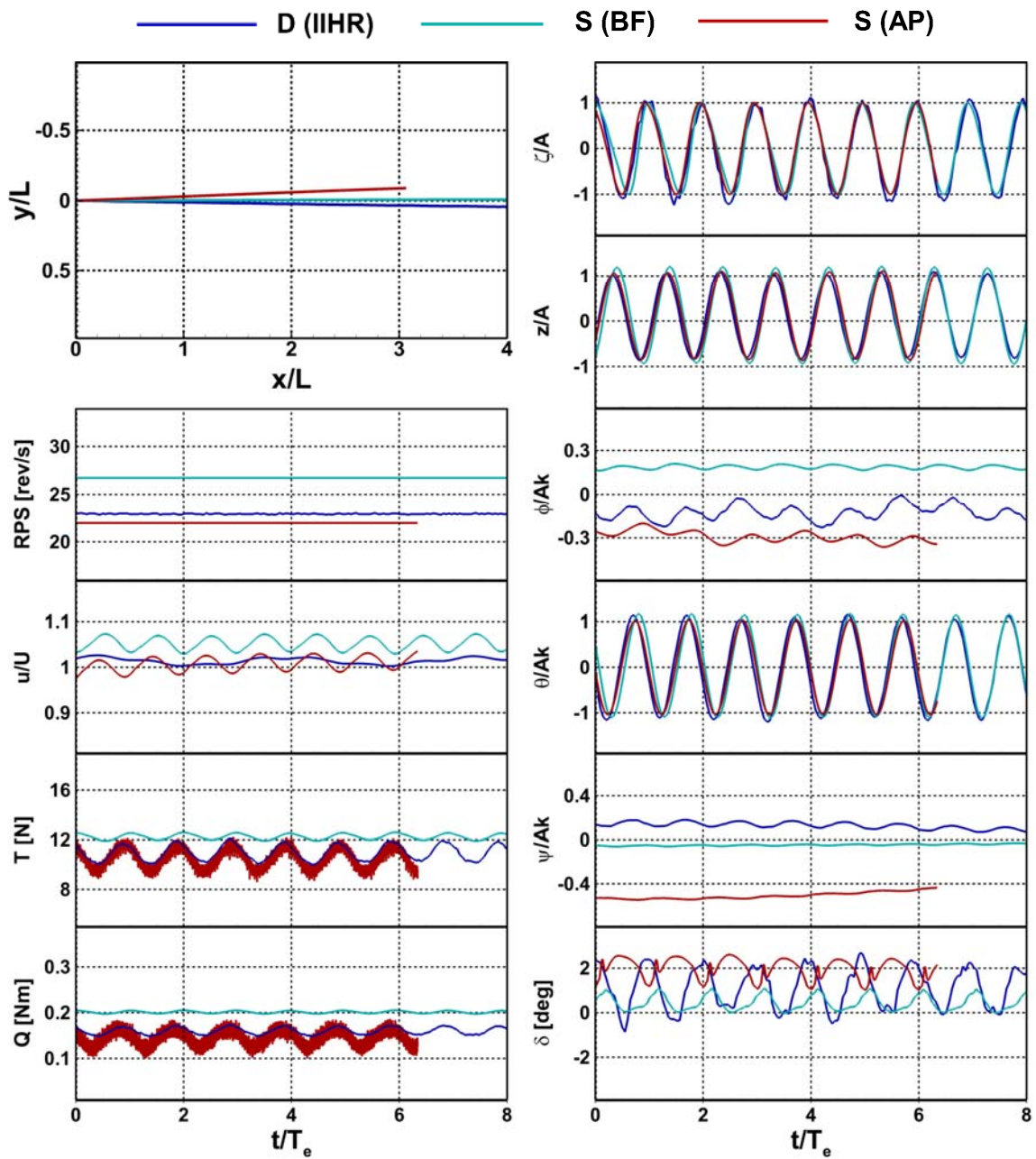


Figure 9-6. Time-histories from the CK test in head wave ( $\lambda/L=1.37$ )

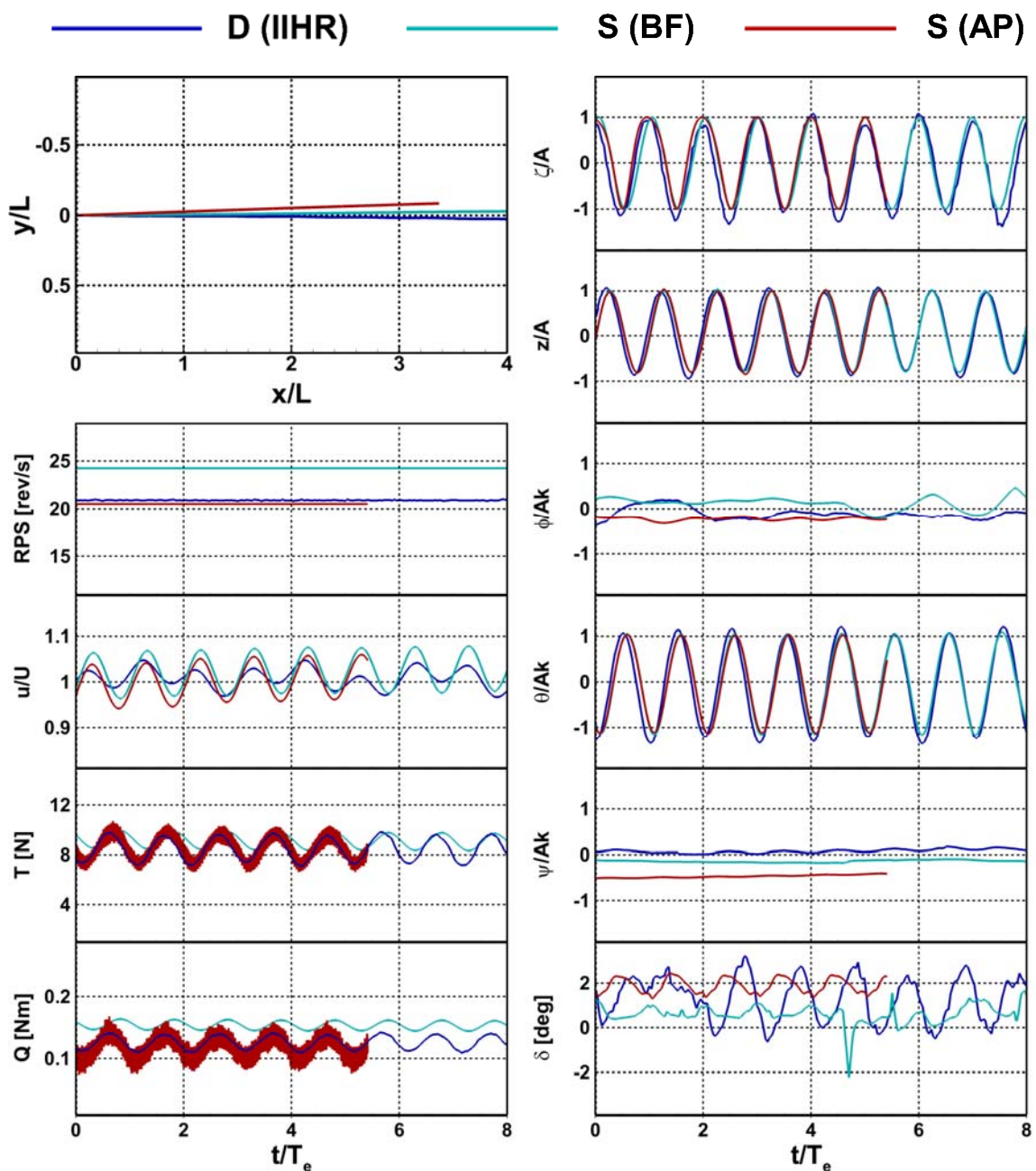


Figure 9-7. Time-histories from the CK test in head wave ( $\lambda/L=1.95$ )

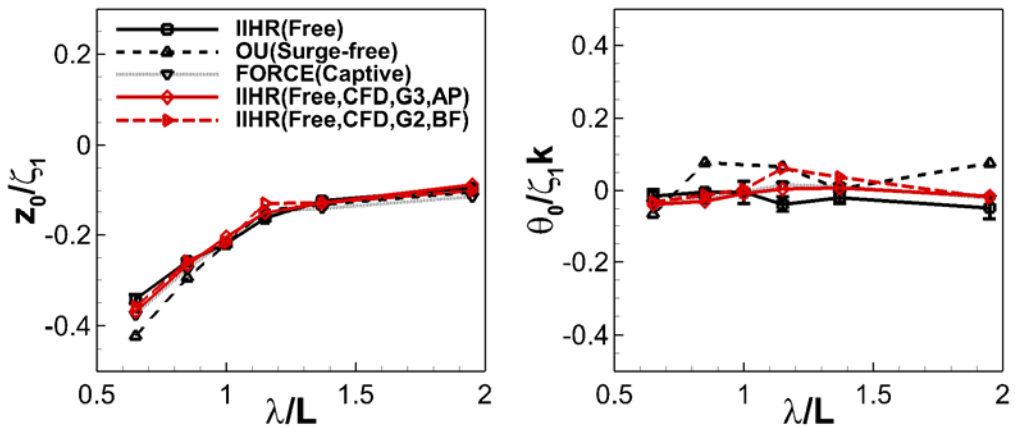


Figure 9-8. RAOs of 0th harm. amp. of heave/pitch in head waves

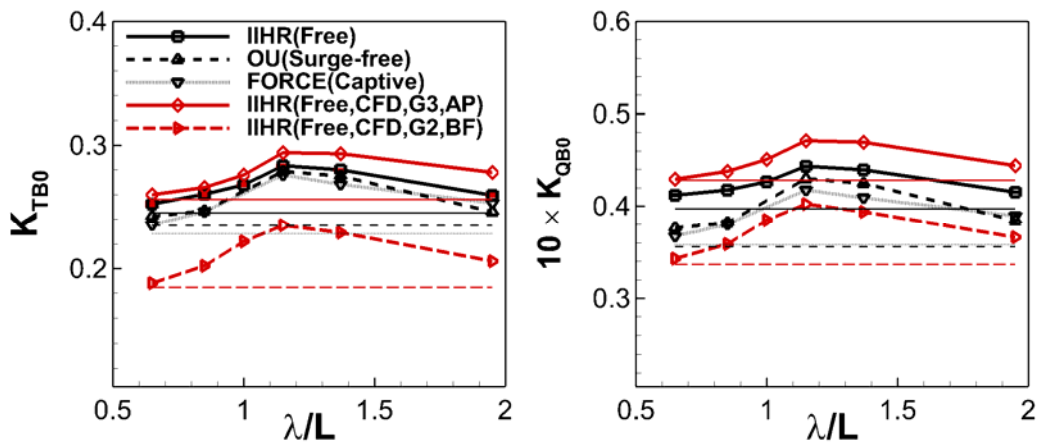


Figure 9-9. RAOs of 0th harm. amp. of thrust/torque coefficients in head waves

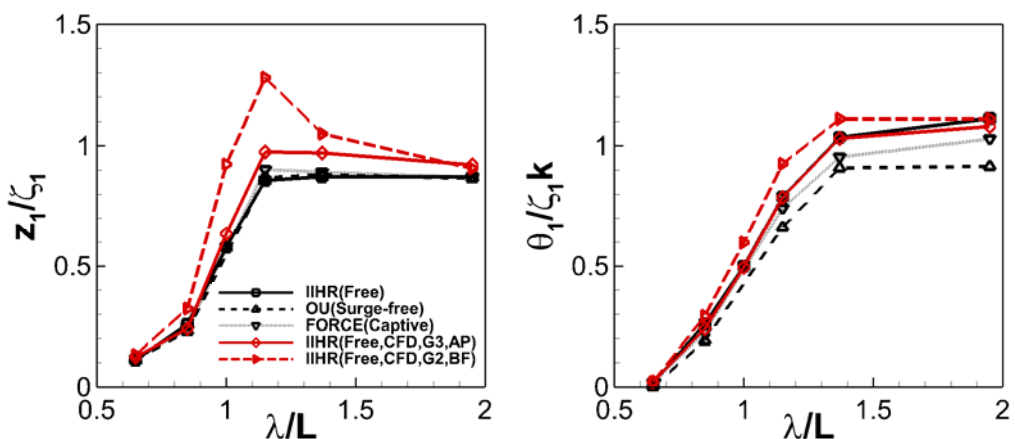


Figure 9-10. RAOs of 1st harm. amp. of heave/pitch in head waves

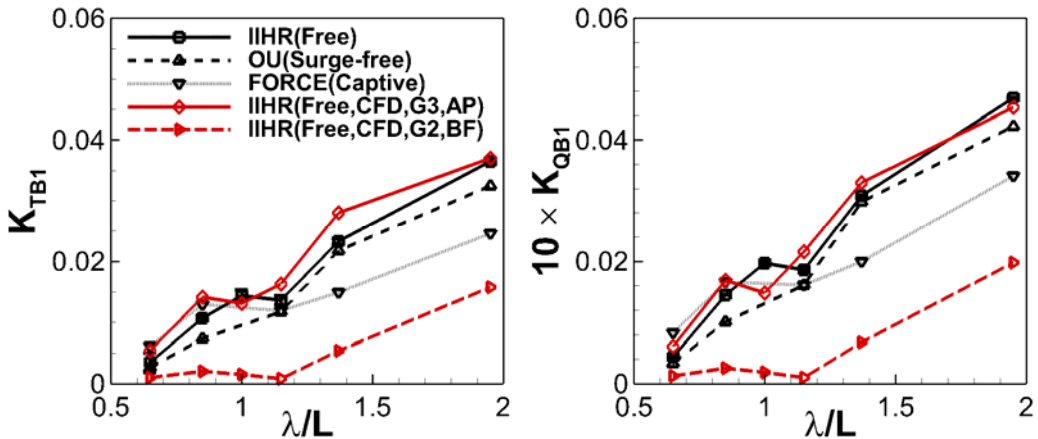


Figure 9-11. RAOs of 1st harm. amp. of thrust/torque coeff. in head waves

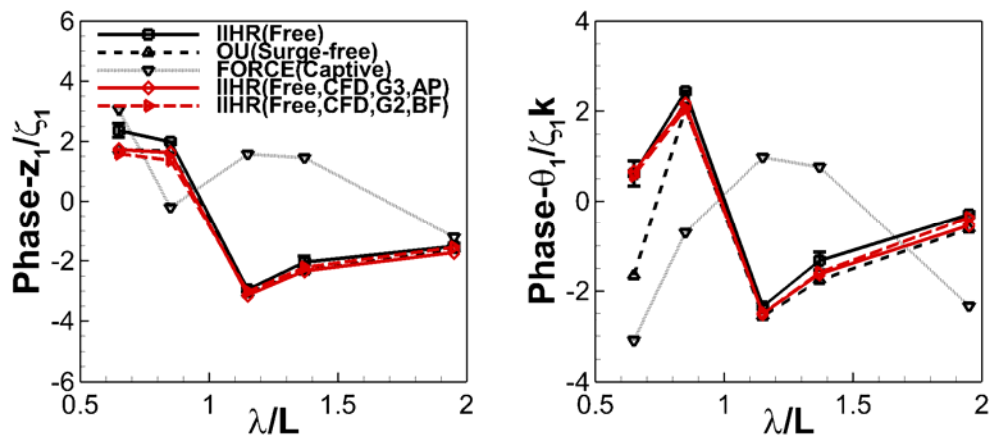


Figure 9-12. RAOs of 1st harm. phase of heave/pitch in head waves

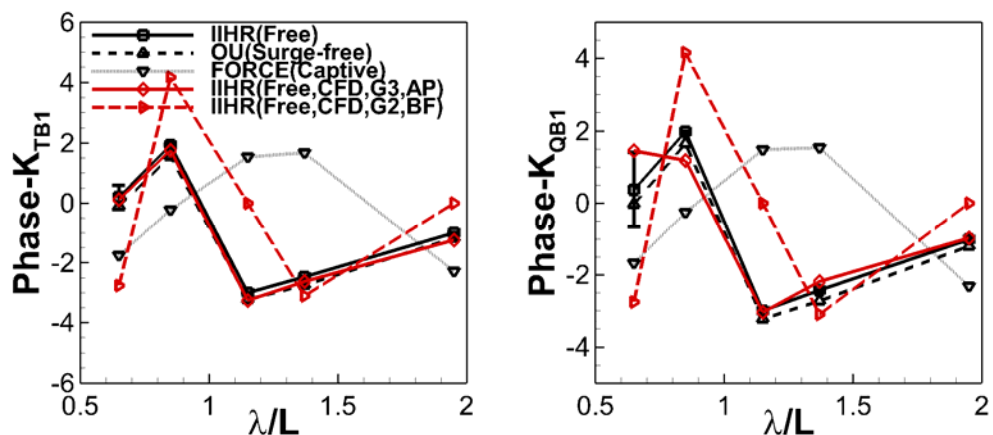


Figure 9-13. RAOs of 1st harm. phase of thrust/torque coeff. in head waves

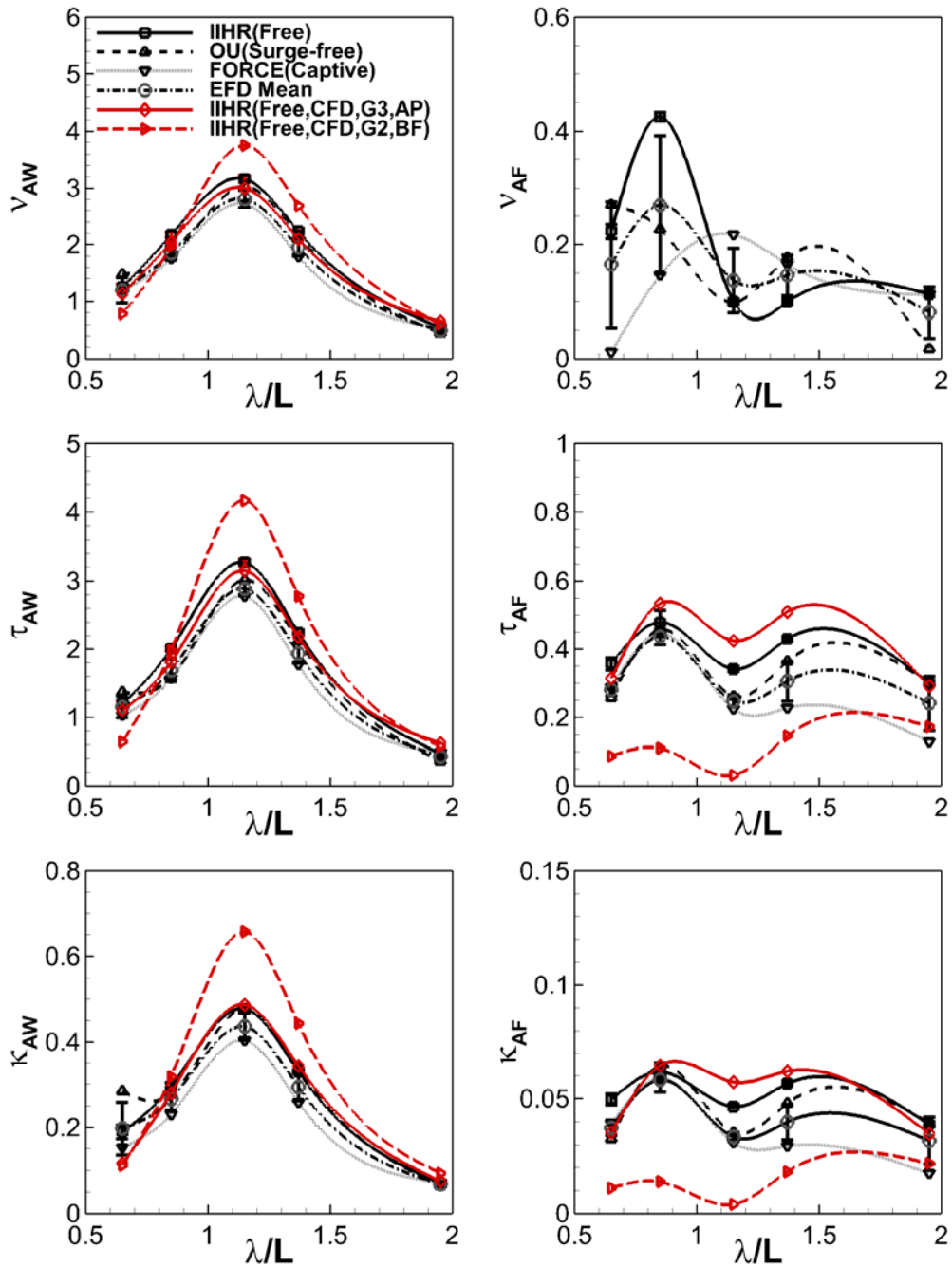


Figure 9-14. RAOs of added-powering var. in head waves

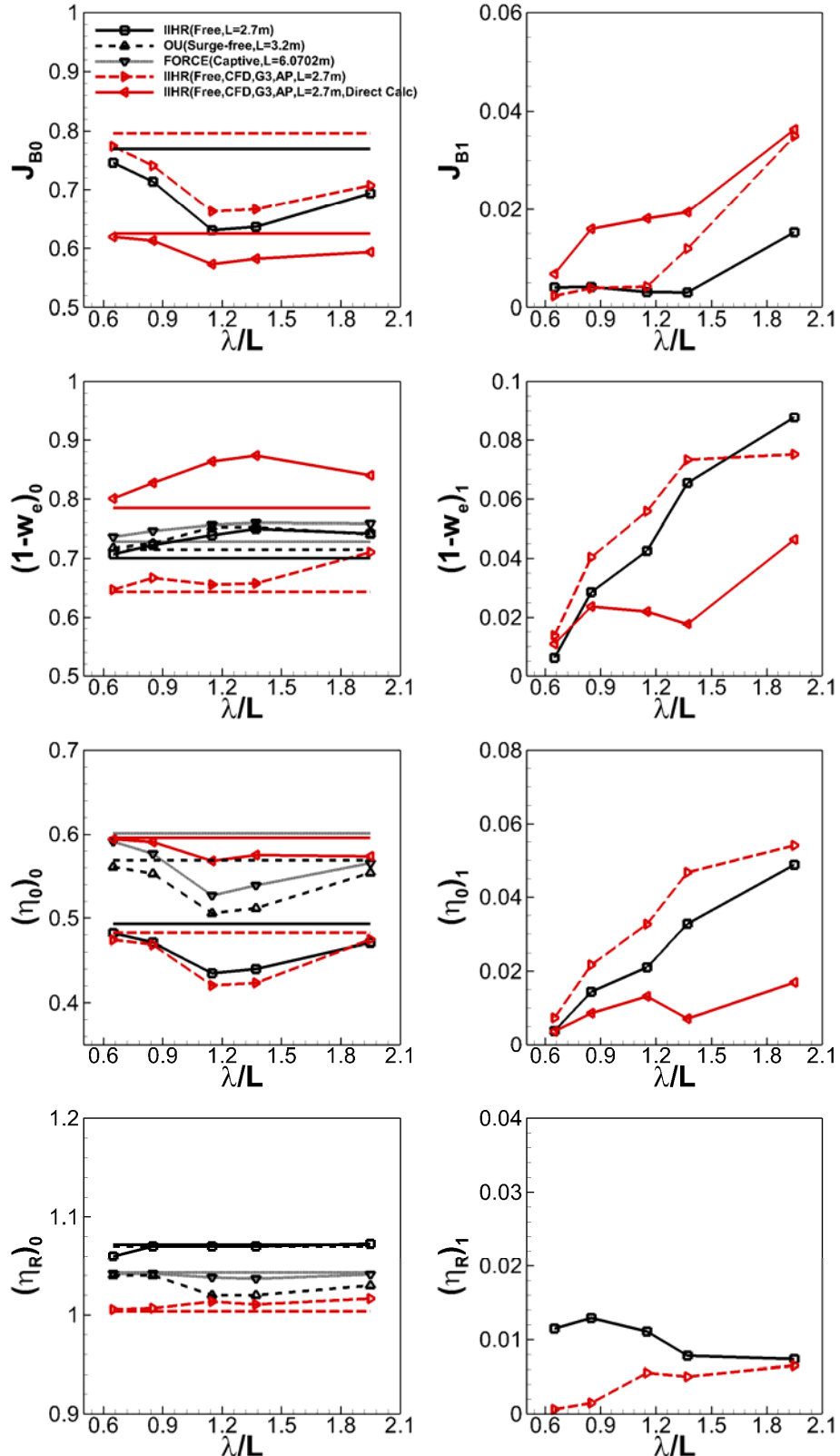


Figure 9-15. RAOs of 0th/1st harm. amp. of SP factors in head waves

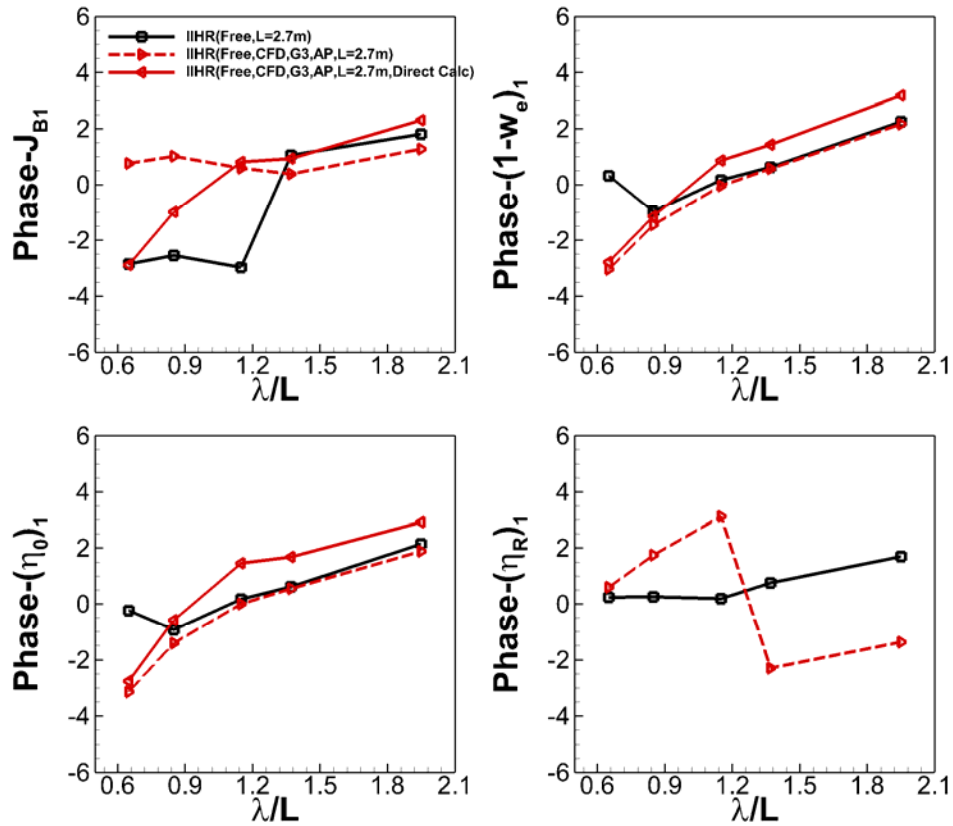


Figure 9-16. RAOs of 1st harm. phases of SP factors in head waves

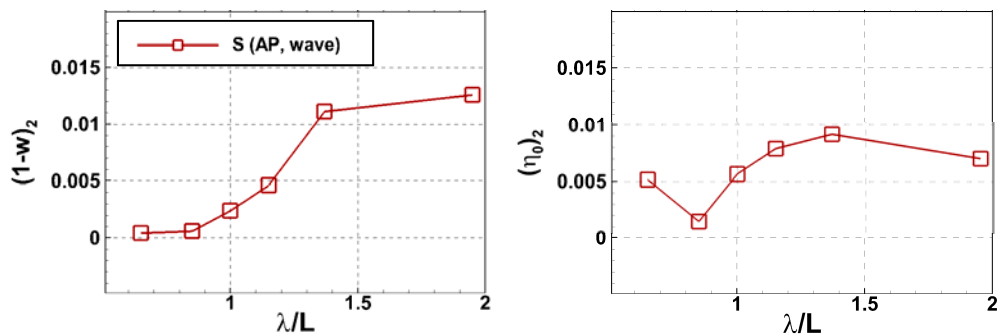


Figure 9-17. RAOs of 2nd harm. amp. of SP factors in head wave

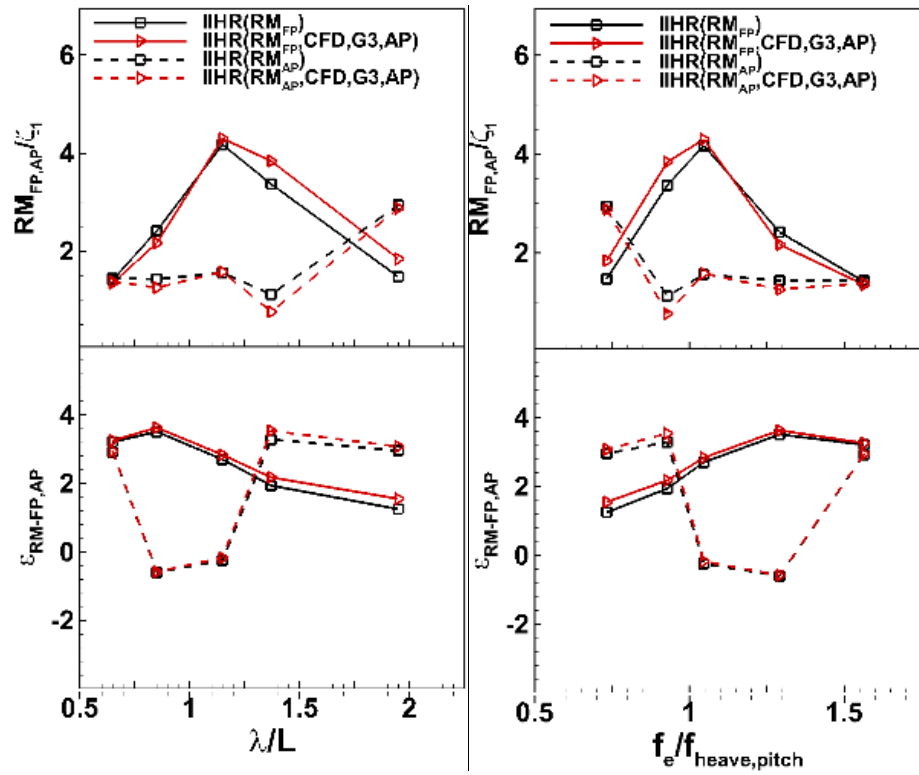


Figure 9-18. RAOs of amp. and phase of relative motions in head waves

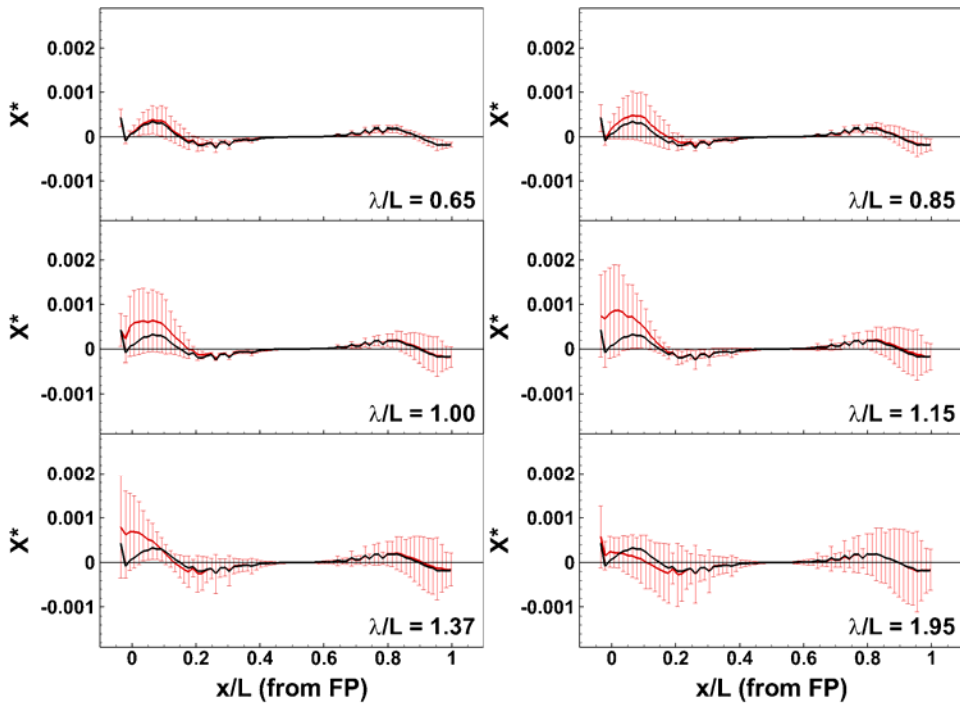


Figure 9-19. Longitudinal dist. of mean hydrodynamic x-forces on the hull in head waves (neg. to FP)

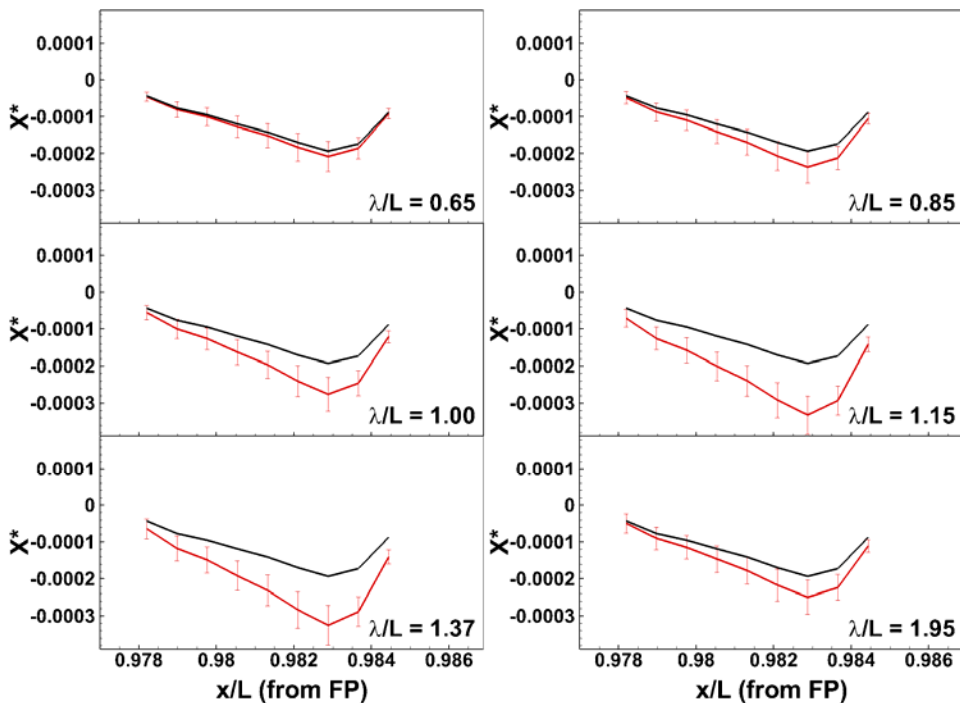


Figure 9-20. Longitudinal dist. of mean hydrodynamic x-forces on the propeller in head waves (neg. to FP)

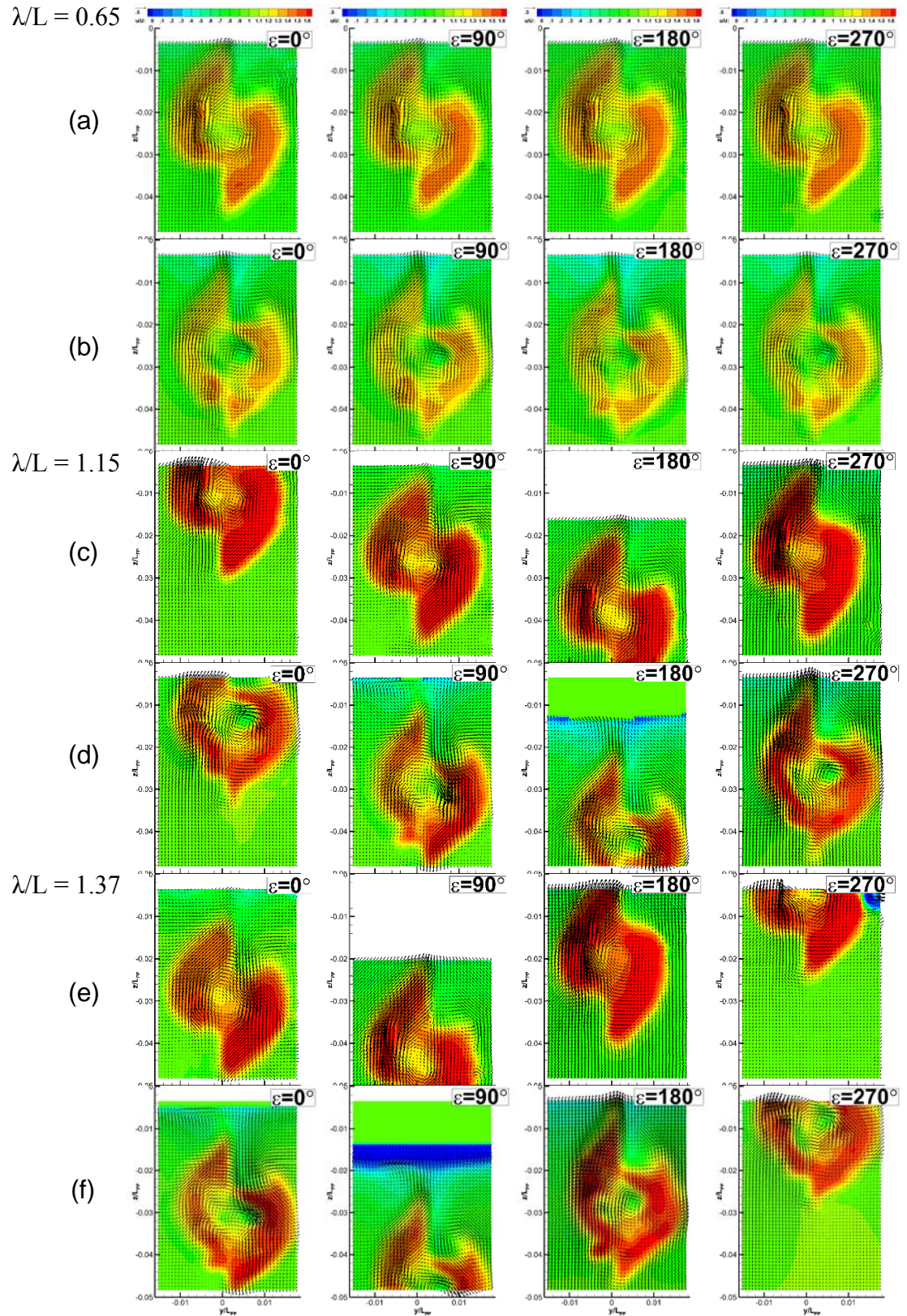


Figure 9-21. Validation of local flow in head wave: (a, c, e) OU PIV; (b, d, f) G3-AP

## 10. COURSE KEEPING IN REGULAR OBLIQUE WAVES

### 10.1. Self-propulsion Test

#### Methodology

The self-propulsion test in oblique waves is performed similar to the self-propulsion test in head waves. The 2DOF captive test is performed for BF model and 6DOF self-propulsion test is performed for AP model. During the 2DOF self-propulsion test using BF model, test case with bow-quartering wave showed solution convergence error and the test conditions is substituted for 6DOF test (Table 10-1). The reason for the error is not clear and not discovered in the current study. Due to this issue, 6DOF test is preferred when AP model is used. When the 6DOF self-propulsion test is performed, three propeller rotational speeds are pre-designed and used as the same as the 2DOF self-propulsion test. During this approach, speed loss/gain is checked at each propeller rotational speed since the ship is not constrained and the final propeller rotational speed is estimated by using the regression curve.

#### Validation

Table 10-1 shows the validation results. Similar to head waves and calm water self-propulsion tests, the averaged  $E\%D$  of the propeller rotational speed at self-propulsion point is - 13.9% for BF model (averaged over 2DOF conditions only) and 5.0% for AP model. The bow-quartering wave condition requires the highest propeller rotational speed among all oblique waves, however, the value is still less than the one used for the head waves. Propeller rotational speeds obtained from the 2DOF self-propulsion tests is not adjusted but could still predict the  $Fn_0$  close enough to the target value unlike head wave cases.

## 10.2. Course-keeping

### 10.2.1. Time-history

Time-histories from the oblique wave course-keeping test cases are shown in Figures 10-1 to 10-4. Four different heading angles ( $\chi = 45^\circ, 90^\circ, 135^\circ$  and  $180^\circ$ ) are tested at the  $\lambda/L = 1.0$  condition. The validation variables include roll angle, yaw angle and rudder angle as well as heave, pitch angle and thrust/torque coefficients that are validated in head wave course-keeping tests.

#### Motions

In the oblique wave test cases, the agreements of the roll, yaw and rudder angles are close between the experiment and CFD due to experiencing sufficient side forces. Roll of IIHR does not reach quasi-steady state during the beam and stern-quartering wave conditions due to experiencing the low frequency wave in a limited size of a wave basin. Unlike the head wave case, IIHR data now shows fluctuations of the ship speed.

#### Thrust and torque

The thrust and torque of IIHR is not in fully quasi-steady state at beam and stern-quartering waves similar to the roll angle.

### 10.2.2. Validation of the Zeroth Harmonic Amplitude

Figures 10-5 to 10-8 show the RAOs of the zeroth harmonic amplitudes in the oblique wave condition. Table 10-2 shows the  $E\%D$  for all variables.

#### Motions

The RAOs of zeroth harmonic amplitudes of heave and pitch angles in the oblique waves are predicted less accurately compared to the head wave cases: the average  $E\%D$  for heave and pitch are  $>26\%$  and  $>52\%$ . Also, the trend does not exist for both variables. More cycles seem

required for both CFD and experiment to reach a better conclusion. The zeroth harmonic amplitude of roll is predicted accurately when AP model is used. BF model also follows the same trend, but the value is constantly biased from IIHR. Averaged  $E\%D$  for roll is 23.8% for AP model and 80.5% for BF model. The prediction for the zeroth harmonic amplitude of the yaw angle is qualitatively satisfactory for both AP and BF models, however, the magnitude is small and there is no clear trend for both CFD and experiment. The averaged  $E\%D$  is 214.1% for BF model and 672.4% for AP model. BF model could predict the large zeroth harmonic amplitude of rudder angle at stern-quartering wave that is close to IIHR than the AP model which demonstrates the need of high resolution of the grid near the rudder for a better prediction of the rudder angle. The averaged  $E\%D$  for the zeroth harmonic amplitude of rudder angle is 46.1% for BF model and 86.5% for AP model.

### **Thrust and torque**

The RAOs of the zeroth harmonic amplitudes of the thrust and torque show peaks at the bow-quartering wave condition and decrease near to the calm water SP values as the wave heading angle increases, which is the same trend as the propeller rotational speed. The BF model shows large gaps in every wave heading and does not show peaks at the bow-quartering wave, however, the trend is similar to the AP model and IIHR. AP model shows good agreement for the zeroth harmonic amplitudes of thrust and torque coefficients by having similar prediction accuracies shown in head waves. The averaged  $E\%D$  for the RAO of zeroth harmonic amplitude of thrust coefficient is 24.9% and 3.3% for BF and AP models. For the RAO of zeroth harmonic amplitude of torque, the  $E\%D$  is 16.1% for BF model and 5.6% for AP model, respectively. The trends of thrust and torque coefficients are the same during the oblique wave conditions. RAOs at stern-quartering wave is higher than ones from beam and following waves.

### **10.2.3. Validation of the First Harmonic Amplitude**

Figures 10-9 to 10-12 show the RAOs of first harmonic amplitudes in the oblique waves.

Table 10-3 shows  $E\%D$ . As seen from the time-history, the predictions for the RAOs of the first harmonic amplitudes of rudder angle, yaw angle and roll angle show improvements from the head wave.

#### **Motions**

The first harmonic amplitude of the heave increases significantly from the head wave condition at bow-quartering and beam wave, and then decreases for the larger heading angle conditions. The BF model over-predicts the first harmonic amplitude of heave at the bow-quartering wave as well as head wave due to active interaction between the propeller and the bare-hull during the excitement. AP model predicts the peak at bow-quartering wave unlike IIHR course-keeping test, however, the overall performance is much improved from the BF model. The  $E\%D$  for the first harmonic amplitude of heave is 43.6% and 17.5% for BF and AP model. The first harmonic amplitude of pitch increases at bow-quartering wave condition, however, the value drops to minimum at beam wave and excites again at stern-quartering wave unlike the first harmonic amplitude of heave. Same as the heave, the BF model shows difference at bow-quartering wave and head wave for pitch. The  $E\%D$  for the first harmonic amplitude of pitch is 17.8% and 10.9% for BF and AP models. The first harmonic amplitude of roll angle and yaw angle have the same trend and become maximum at the stern-quartering wave. Both AP and BF models could predict the trend, however, under-predict both values at stern-quartering waves. The short amount of IIHR data might have contributed for the source of the error. The  $E\%D$  for the first harmonic amplitude of roll and yaw exceeds 56% and 29% for both models. The agreement for the first harmonic amplitude of rudder angle perfectly fits the data at all heading angles and only

shows 3.2% and 3.5%  $E\%D$  for BF and AP model. The trend of the first harmonic amplitude of rudder angle is close to trends of roll and yaw.

### **Thrust and torque**

The BF model fails to predict the first harmonic amplitude of thrust and torque during the excitement (head and bow-quartering wave) and also beam waves. When IIHR and AP model results are checked, the first harmonic amplitude of thrust and torque coefficients both show large values at bow-quartering, stern-quartering and following wave conditions while the values are much smaller for head waves and beam waves. The averaged  $E\%D$  for the first harmonic amplitude of thrust and torque are >50% for BF model and 14.1%/12.4% for the AP model.

#### **10.2.4. Validation of First Harmonic Phase**

Figure 10-7 and Table 10-4 shows the validation results for the first harmonic phase. The overall agreement is satisfactory when using the AP model.

### **Motions**

The agreement of the first harmonic phase for heave and pitch angles are satisfactory for both BF and AP models. The first harmonic phase of pitch angle does not show a shift until beam waves and show shift by 180° at stern-quartering wave. The AP model predicts the first harmonic phase of roll angle fairly good, however, it significantly under-predicts at the beam wave condition. The reason is unclear but a sufficient amount of experimental data for the convergence of the roll angle is required. The BF model under-predicts at both beam and following waves. The agreement for the first harmonic phase of yaw and rudder angle is close for the AP model except for head and following waves where the side force is not significant. The same trend is shown for the BF model.

The averaged  $E\%2\pi$  for heave, pitch, roll, yaw and rudder angle are 5.8%, 5.8%, 14.0%, 3.9% and 4.9% for BF model and 4.7%, 7.6%, 18.4%, 6.6% and 5.3% for the AP model.

### **Thrust and torque**

The first harmonic phases for the thrust and torque are well predicted for the AP model. The BF model under-predicts by a little less than 180° for both thrust and torque at beam and stern-quartering waves. Unlike the heading wave condition, the BF model shows good agreement for the first harmonic phase of thrust and torque at the bow-quartering wave condition. The averaged  $E\%2\pi$  for both thrust and torque are 15.8% and 16.3% for the BF model and 5.6% and 10.7% for the AP model.

#### **10.2.5. Added Powering Variables**

##### **Added thrust, added torque and added propeller rotational speed**

The BF model showed less accuracy in the head wave conditions than the AP model for added thrust, added torque and added propeller rotational speed, however, the model could predict close to the IIHR in the oblique wave conditions. AP model is consistently showing great accuracy in both head and oblique wave conditions. Like the head wave cases, the added thrust, added torque and added propeller rotational speed curves are close to the added-resistance curves found in the oblique wave condition. The  $E\%D$  for added thrust, torque and propeller rotational speed are 17.3%, 16.7% and 4.0% for BF model and 28.4%, 36.8% and 37.2% for the AP model.

##### **Fluctuation of thrust and torque**

The trends for the fluctuation of thrust and torque are showing good agreement between the AP model and IIHR, however, the BF model under-predicts the fluctuation by a huge

difference. The  $E\%D$  for both thrust and torque fluctuations are 66.5% and 67.3% for BF model and 9.6% and 9.7% for AP model.

### **10.2.6. Self-Propulsion Factors**

#### **Effective wake fraction**

The zeroth harmonic amplitude of the  $1 - \omega_e$  decreases at the bow-quartering wave condition by a large amount even though the decrease of thrust, torque and propeller rotational speed is insignificant. The  $1 - \omega_e$  might have been affected by some other source. The direct calculation method is not used for the oblique wave in this study, however, more detailed information seems required to check the magnitude and distribution of the effective wake. The averaged  $E\%D$  for the  $1 - \omega_e$  is 10.5%.

#### **Propeller efficiency**

The propeller efficiency is the lowest at bow-quartering wave and highest at following wave. The heading angle 180° case shows less propeller efficiency than the propeller efficiency in calm water by a small amount. The averaged  $E\%D$  for propeller efficiency is 2.1%.

#### **Relative rotative efficiency**

Like the head wave case, the relative rotative efficiency is different between the experiment and CFD by 5.4% of  $E\%D$  in average.

### **10.2.7. Relative Motions**

The relative motion predicted by G3-AP agrees well with the experiment data for most of the heading angles as shown in Figure 10-8. The difference of the relative motion amplitude between the forward and aft perpendiculars is the largest at the bow-quartering wave condition. Same as the head wave cases, the phase difference of the relative motions of the forward and aft

perpendiculars is about  $180^\circ$  for the AP model. IIHR shows bigger difference due to the smaller relative motion at the aft perpendicular.

#### **10.2.8. Location of the Added-resistance**

In Figure 10-20, the longitudinal distributions of the mean and standard deviation of hydrodynamic resistances on the bare-hull are compared with the calm water self-propulsion test result. The standard deviation of calm water self-propulsion test is almost none. The bow-quartering wave case shows similar trend as head wave cases: mean hydrodynamic resistance is higher at bow region. Beam wave and following wave conditions do not show much difference from the calm water self-propulsion test for the mean hydrodynamic resistance, however, the standard deviation of the hydrodynamic resistance indicates that ship is still experiencing more pressure deviations on the hull during the course-keeping condition. Stern-quartering wave condition shows less deviated mean hydrodynamic resistance compared to self-propulsion test in calm water of which the reason is not clear. In Figure 10-21, the mean and standard deviation of hydrodynamic resistance on the propeller is shown. The values of bow-quartering, beam and following wave are larger or almost similar to values of calm water self-propulsion test. However, the value at stern-quartering wave condition is less than calm water self-propulsion test.

Table 10-1. Validation of propeller rotational speed for SP tests in oblique waves

Var.	$\chi [^\circ]$	D	S		(D-S)%D			
		IIHR	BF, G2		AP, G3	BF, G2		
			2DOF	6DOF	6DOF	2DOF	6DOF	
$n_{calm}$ [RPS]		19.0	22.03		18.14	-16.0		4.6
$n_{wave}$ [RPS]	45	21.40	24.49		20.81	-14.4		2.7
	90	19.90	22.43		18.85	-12.7		5.3
	135	19.88	22.90		18.60	-15.2		6.5
	180	19.42	22.07		18.35	-13.7		5.5
	Ave.					<b>-13.9</b>		<b>5.0</b>
$n_{wave}$ $/n_{calm}$	45	1.126	1.112		1.147	1.28		-1.9
	90	1.047	1.018		1.039	2.8		0.8
	135	1.046	1.039		1.025	0.7		2.0
	180	1.022	1.002		1.012	2.0		1.0
	Ave.					<b>1.8</b>		<b>1.4</b>

Table 10-2. Validation of 0th harm. amp. for CK tests in oblique waves

Case	$\chi [^\circ]$	$z_0/\zeta_1$	$\phi_0/\zeta_1 k$	$\theta_0/\zeta_1 k$	$\psi_0/\zeta_1 k$	$\delta_0$ [deg]	$K_{TB,0}$	$K_{QB,0}$
D	45	-0.174	-0.477	-0.0515	-0.039	2.170	0.275	0.0437
	90	-0.128	-0.267	-0.0576	0.021	2.120	0.256	0.0414
	135	-0.177	-0.332	-0.0197	-0.375	-0.873	0.261	0.0421
	180	-0.241	-0.196	-0.0552	-0.147	1.130	0.249	0.0404
S (BF)	45	-0.160	-0.215	0.0059	-0.053	1.252	0.215	0.0376
	90	-0.226	0.138	-0.0418	-0.082	0.966	0.186	0.0340
	135	-0.217	-0.216	-0.0353	0.083	-1.237	0.194	0.0350
	180	-0.238	0.168	-0.0310	-0.025	0.610	0.187	0.0341
S (AP)	45	-0.218	-0.595	-0.0154	-0.242	0.982	0.286	0.0464
	90	-0.205	-0.319	-0.0468	-0.287	1.230	0.262	0.0434
	135	-0.204	-0.422	-0.0370	-0.182	0.547	0.268	0.0441
	180	-0.233	-0.286	-0.0380	-0.285	1.141	0.260	0.0431
$E\%D$ (BF)	45	7.8	55.0	111.5	-34.3	42.3	21.8	14.0
	90	-77.0	151.6	27.3	485.9	54.5	27.3	17.9
	135	-22.5	34.8	-79.5	122.1	-41.7	25.8	16.9
	180	1.1		44.0			25.0	15.6
	Ave.	<b>27.1</b>	<b>80.5</b>	<b>65.6</b>	<b>214.1</b>	<b>46.1</b>	<b>24.9</b>	<b>16.1</b>
$E\%D$ (AP)	45	-25.8	-24.7	70.1	-515.0	54.8	-4.1	-6.2
	90	-60.4	-19.6	18.7	1450.8	42.0	-2.5	-4.8
	135	-15.3	-27.1	-88.2	51.4	162.7	-2.6	-4.7
	180	3.2		31.2			-4.3	-6.7
	Ave.	<b>26.2</b>	<b>23.8</b>	<b>52.0</b>	<b>672.4</b>	<b>86.5</b>	<b>3.3</b>	<b>5.6</b>

Table 10-3. Validation of 1st harm. amp. for CK tests in oblique waves

Case	$\chi [^\circ]$	$z_1/\zeta_1$	$\phi_1/\zeta_1 k$	$\theta_1/\zeta_1 k$	$\psi_1/\zeta_1 k$	$\delta_1$ [deg]	$K_{TB,1}$	$K_{QB,1}$
D	45	0.999	0.155	0.673	0.118	3.870	0.0204	0.0028
	90	1.090	0.387	0.055	0.015	1.350	0.0088	0.0011
	135	0.339	2.028	0.446	0.880	10.500	0.0209	0.0028
	180	0.111	0.260	0.176	0.013	0.426	0.0227	0.0028
S (BF)	45	1.370	0.103	0.796	0.146	3.961	0.0025	0.0003
	90	1.170	0.052	0.053	0.023	1.268	0.0011	0.0001
	135	0.415	0.633	0.418	0.617	10.640	0.0196	0.0025
	180	0.231	0.285	0.254	0.008	0.148	0.0185	0.0023
S (AP)	45	1.165	0.134	0.663	0.143	3.925	0.0242	0.0030
	90	1.074	0.043	0.062	0.019	1.266	0.0097	0.0012
	135	0.384	0.682	0.370	0.582	10.796	0.0188	0.0024
	180	0.154	0.389	0.197	0.071	0.815	0.0265	0.0034
$E\%D$ (BF)	45	-37.1	33.3	-18.3	-23.5	-2.3	88.0	88.7
	90	-7.4	86.5	2.8	-59.5	6.0	87.8	88.6
	135	-22.5	68.8	6.2	29.8	-1.3	6.0	9.6
	180	-107.5		-43.9			18.5	17.7
	Ave.	<b>43.6</b>	<b>62.9</b>	<b>17.8</b>	<b>37.6</b>	<b>3.2</b>	<b>50.1</b>	<b>51.1</b>
$E\%D$ (AP)	45	-16.6	13.6	1.5	-20.6	-1.4	-18.8	-7.9
	90	1.4	89.0	-13.4	-33.9	6.2	-10.9	-7.3
	135	-13.3	66.3	17.0	33.9	-2.8	9.9	13.2
	180	-38.6		-11.8			-17.0	-21.0
	Ave.	<b>17.5</b>	<b>56.3</b>	<b>10.9</b>	<b>29.5</b>	<b>3.5</b>	<b>14.1</b>	<b>12.4</b>

Table 10-4. Validation of 1st harm. phases for CK tests in oblique waves

Case	$\chi [^\circ]$	$\varepsilon_{z1}$	$\varepsilon_{\phi1}$	$\varepsilon_{\theta1}$	$\varepsilon_{\psi1}$	$\varepsilon_{\delta1}$	$\varepsilon_{TB,1}$	$\varepsilon_{QB,1}$
D	45	-3.13	3.14	-2.28	-3.13	-3.07	2.67	2.67
	90	-1.09	-0.62	-3.14	2.75	-1.65	-0.52	-0.57
	135	1.60	2.96	0.62	-1.11	-1.17	-2.71	-2.76
	180	1.92	0.45	2.34	-1.20	0.18	-0.19	-0.20
S (BF)	45	-3.17	2.31	-2.44	-3.04	-2.61	2.62	2.62
	90	-1.19	1.01	-2.43	3.06	-1.63	1.71	1.71
	135	1.61	3.15	0.38	-1.45	-0.73	-1.40	-1.40
	180	3.22	3.62	1.98	-4.69	-3.57	0.19	0.19
S (AP)	45	-3.49	2.47	-2.66	-3.13	-2.64	2.45	2.96
	90	-1.18	1.93	-2.42	1.87	-1.77	-0.22	0.34
	135	1.43	3.21	0.27	-1.47	-0.71	-3.26	-3.86
	180	2.49	0.18	1.87	-2.86	-1.40	-0.54	-0.59
$E\%D$ (BF)	45	0.7	13.2	2.6	-1.4	-7.3	0.8	0.9
	90	1.6	-25.9	-11.2	-4.9	-0.3	-35.5	-36.3
	135	-0.1	-3.0	3.8	5.4	-7.0	-20.8	-21.7
	180	-20.7	-50.5	5.8	55.6		-6.1	-6.1
	Ave.	<b>5.8</b>	<b>14.0</b>	<b>5.8</b>	<b>3.9</b>	<b>4.9</b>	<b>15.8</b>	<b>16.3</b>
$E\%D$ (AP)	45	5.7	10.7	6.1	0.0	-6.8	3.5	-4.5
	90	1.4	-40.5	-11.4	14.1	1.9	-4.7	-14.5
	135	2.7	-3.9	5.6	5.7	-7.3	8.8	17.4
	180	-9.1		7.5			5.5	6.2
	Ave.	<b>4.7</b>	<b>18.4</b>	<b>7.6</b>	<b>6.6</b>	<b>5.3</b>	<b>5.6</b>	<b>10.7</b>

Table 10-5. Validation of added-powering var. for CK tests in oblique waves

Case	$\chi [^\circ]$	$v_{AW}$	$\tau_{AW}$	$\kappa_{AW}$	$\tau_{AF}$	$\kappa_{AF}$
D	45	2.616	2.708	0.402	0.664	0.090
	90	1.055	0.958	0.144	0.247	0.030
	135	1.036	1.103	0.162	0.587	0.077
	180	0.542	0.433	0.060	0.608	0.076
S (BF)	45	2.610	2.770	0.416	0.055	0.007
	90	1.110	0.744	0.064	0.019	0.002
	135	1.090	0.918	0.153	0.371	0.047
	180	0.514	0.313	0.059	0.334	0.042
S (AP)	45	2.840	2.860	0.480	0.747	0.096
	90	0.754	0.678	0.129	0.246	0.030
	135	0.484	0.638	0.068	0.464	0.058
	180	0.226	0.274	0.025	0.636	0.082
$E\%D$ (BF)	45	0.2	-2.3	-3.6	91.7	92.7
	90	-5.2	22.3	55.4	92.4	92.6
	135	-5.2	16.7	5.9	36.9	39.3
	180	5.2	27.7	2.0	45.1	44.6
	Ave.	<b>4.0</b>	<b>17.3</b>	<b>16.7</b>	<b>66.5</b>	<b>67.3</b>
$E\%D$ (AP)	45	-8.5	-5.6	-19.6	-12.5	-6.1
	90	28.6	29.2	10.8	0.5	0.0
	135	53.3	42.1	58.1	20.9	24.6
	180	58.3	36.7	58.8	-4.7	-8.1
	Ave.	<b>37.2</b>	<b>28.4</b>	<b>36.8</b>	<b>9.6</b>	<b>9.7</b>

Table 10-6. Validation of SP factors for CK tests in oblique waves

Case	$\chi$ [°]	Thrust Identification		
		$(1 - w_e)_0$	$(\eta_0)_0$	$(\eta_R)_0$
D	45	0.716	0.448	1.060
	90	0.717	0.477	1.060
	135	0.701	0.469	1.060
	180	0.716	0.486	1.070
	Ave	<b>0.713</b>	<b>0.470</b>	<b>1.063</b>
S (AP)	45	0.634	0.431	1.007
	90	0.642	0.472	1.005
	135	0.634	0.463	1.004
	180	0.642	0.475	1.003
	Ave	<b>0.638</b>	<b>0.460</b>	<b>1.005</b>
$E\%D$ (AP)	45	11.4	3.7	5.0
	90	10.4	1.1	5.2
	135	9.6	1.3	5.2
	180	10.4	2.3	6.2
	Ave	<b>10.5</b>	<b>2.1</b>	<b>5.4</b>

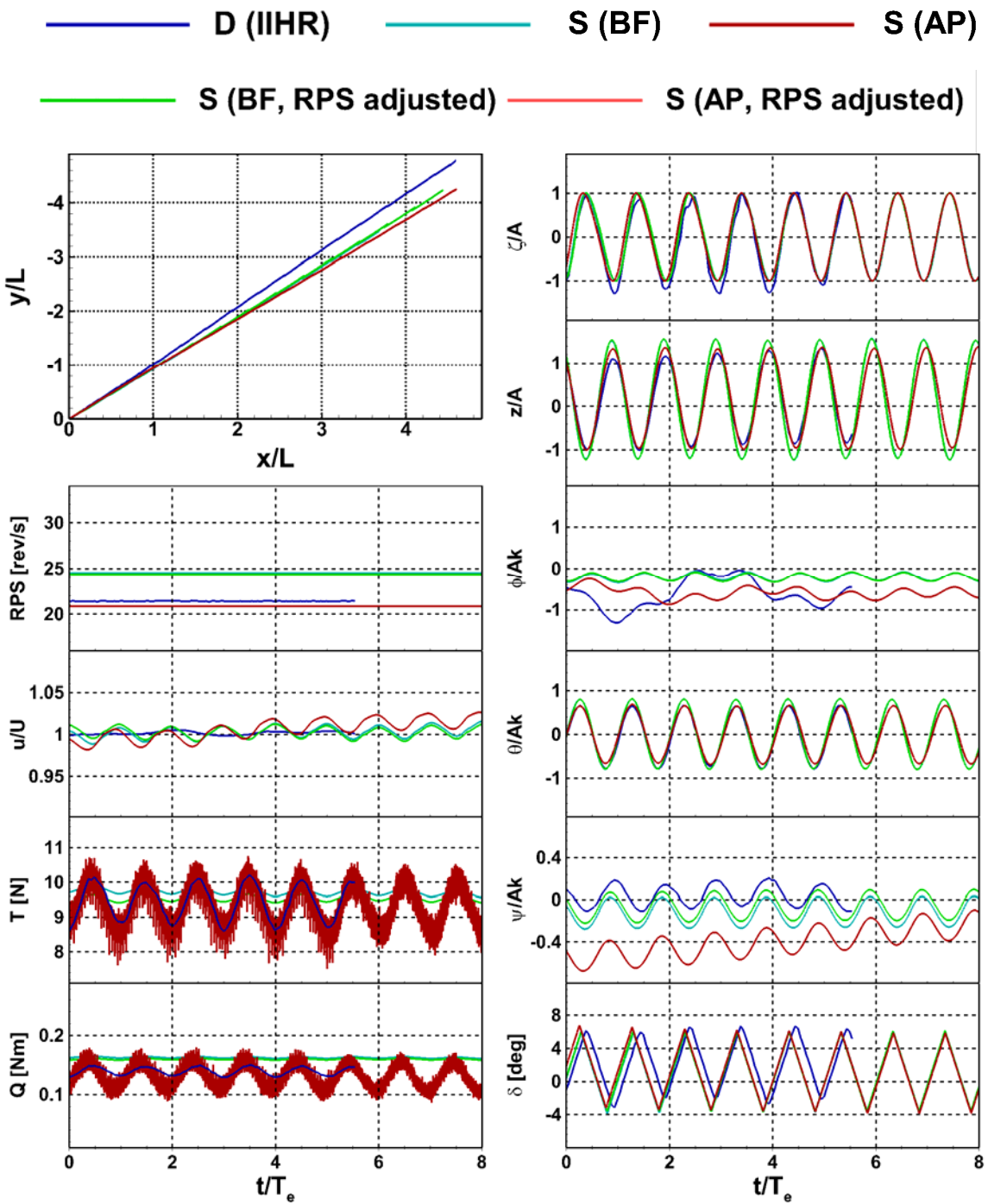


Figure 10-1. Time-histories from the CK test in oblique wave ( $\chi = 45^\circ$ )

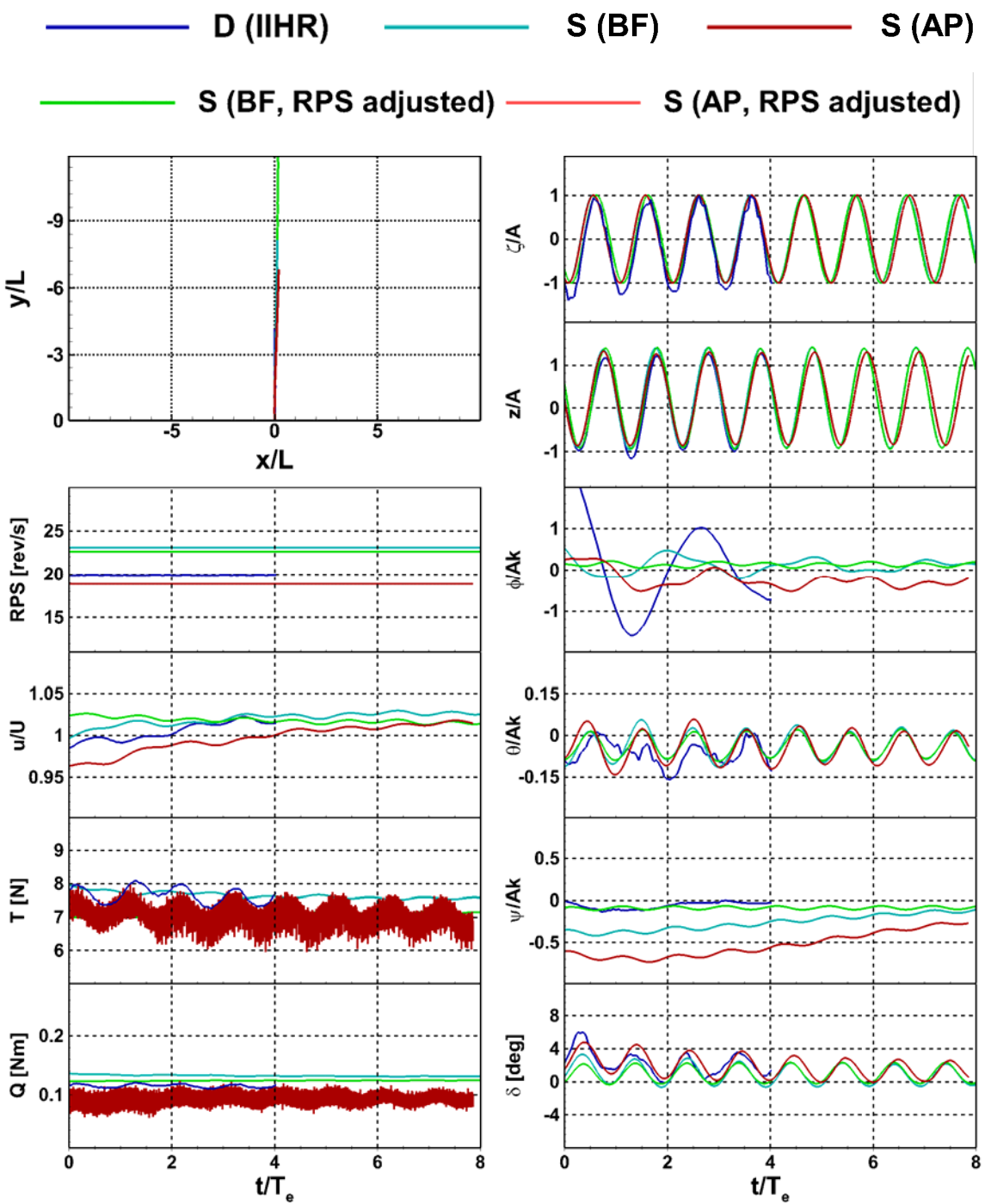


Figure 10-2. Time-histories from the CK test in oblique wave ( $\chi = 90^\circ$ )

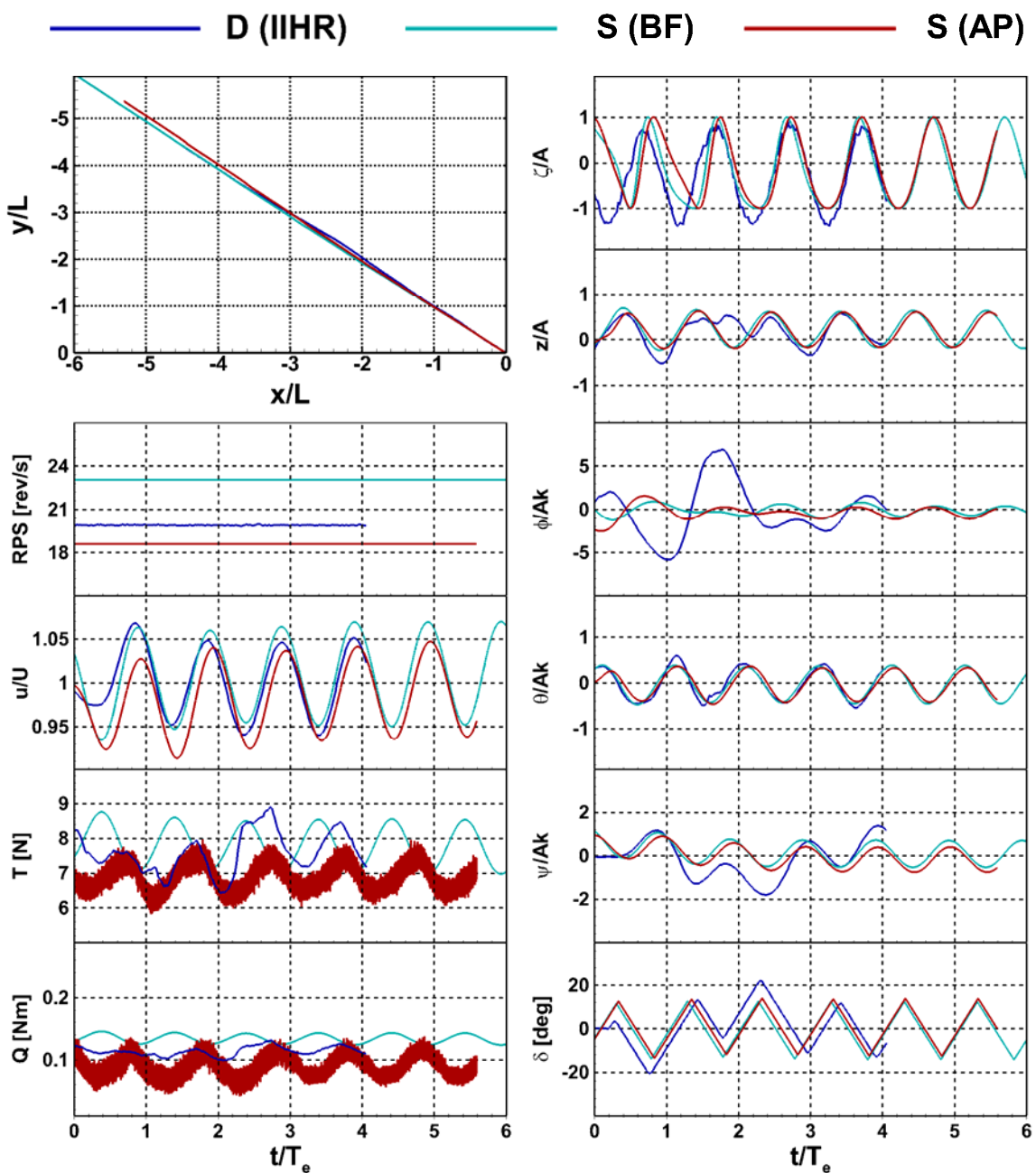


Figure 10-3. Time-histories from the CK test in oblique wave ( $\chi = 135^\circ$ )

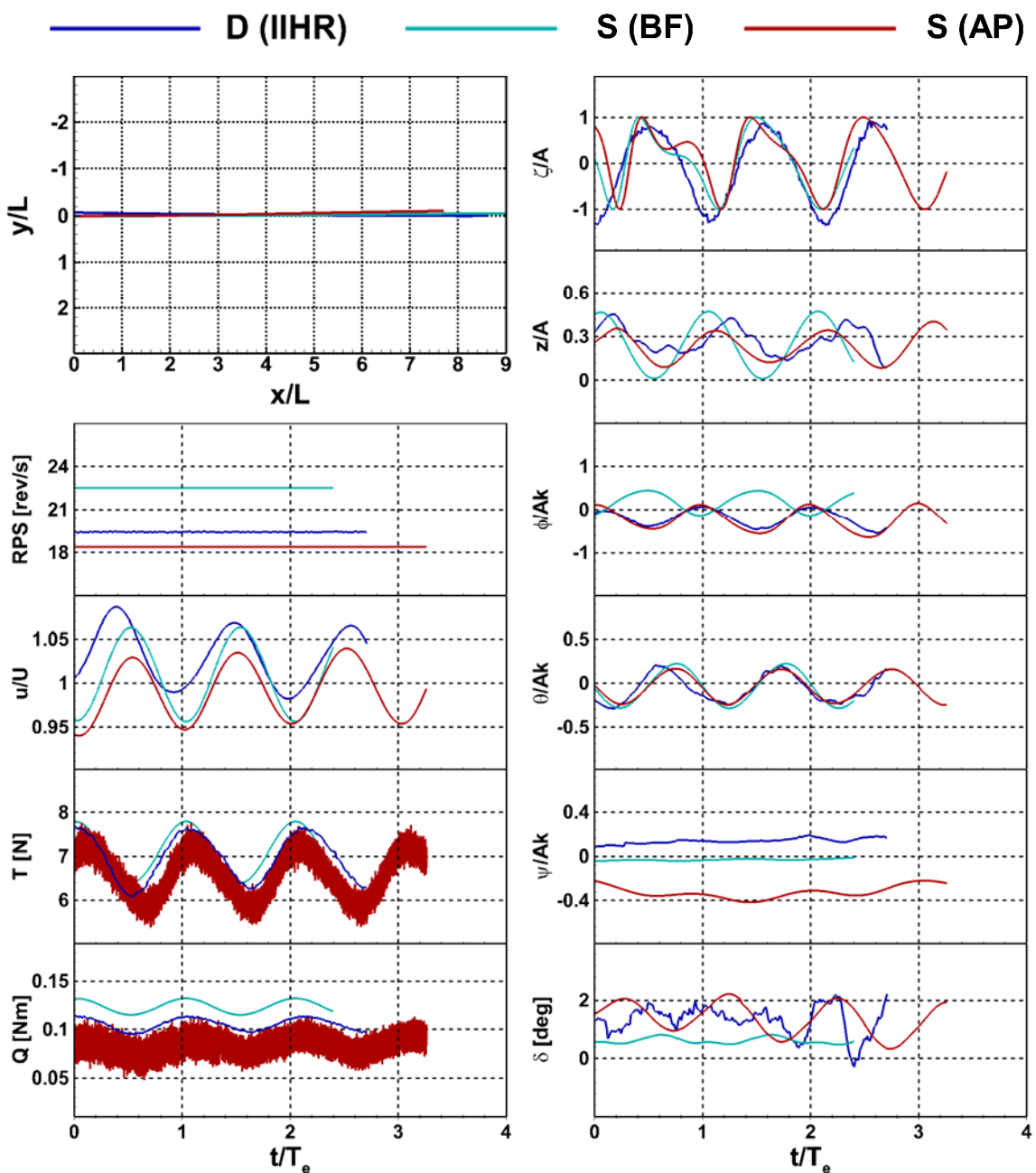


Figure 10-4. Time-histories from the CK test in oblique wave ( $\chi = 180^\circ$ )

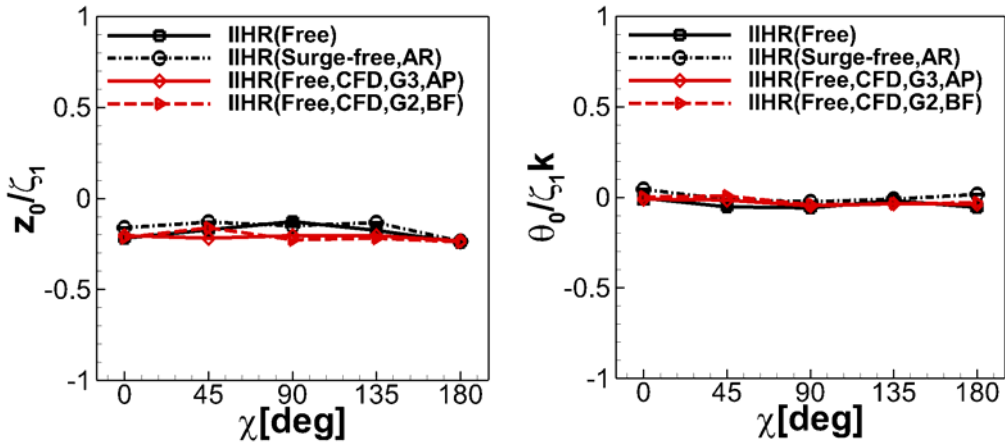


Figure 10-5. RAOs of 0th harm. amp. of heave/pitch in oblique waves

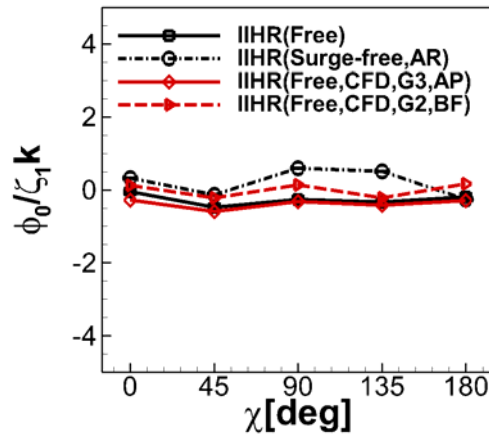


Figure 10-6. RAOs of 0th harm. amp. of roll in oblique waves

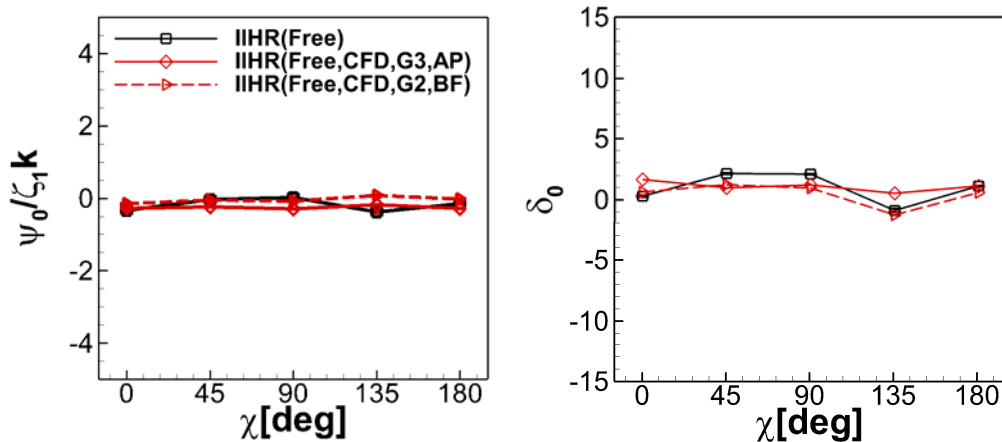


Figure 10-7. RAOs of 0th harm. amp. of yaw/rudder angle in oblique waves

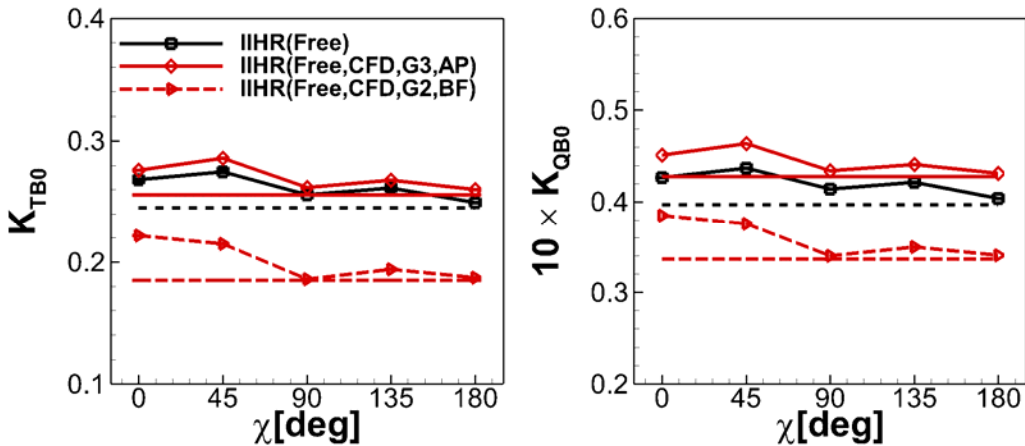


Figure 10-8. RAOs of 0th harm. amp. of thrust/torque coeff. in oblique waves

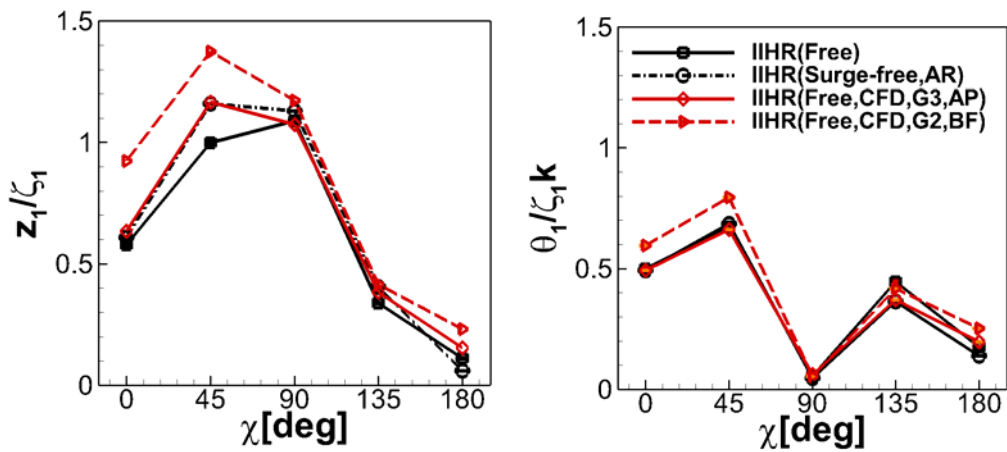


Figure 10-9. RAOs of 1st harm. amp. of heave/pitch in oblique waves

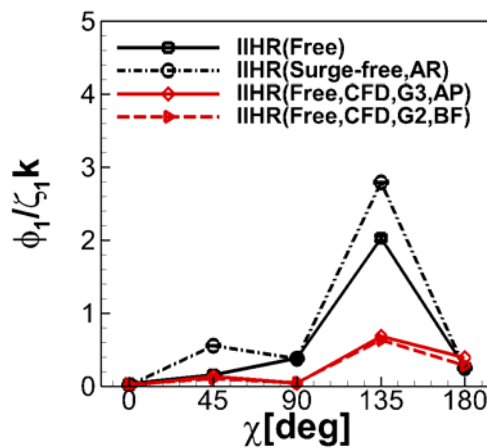


Figure 10-10. RAOs of 1st harm. amp. of roll in oblique waves

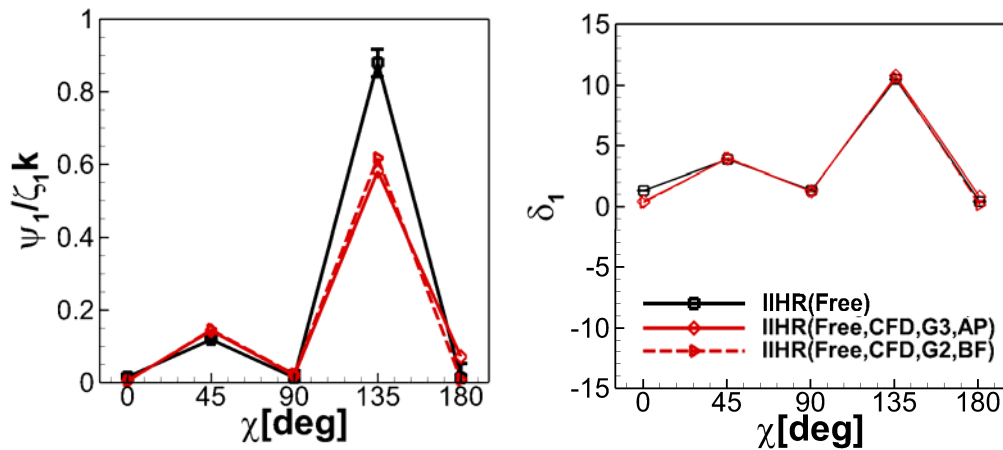


Figure 10-11. RAOs of 1st harm. amp. of yaw/rudder angle in oblique waves

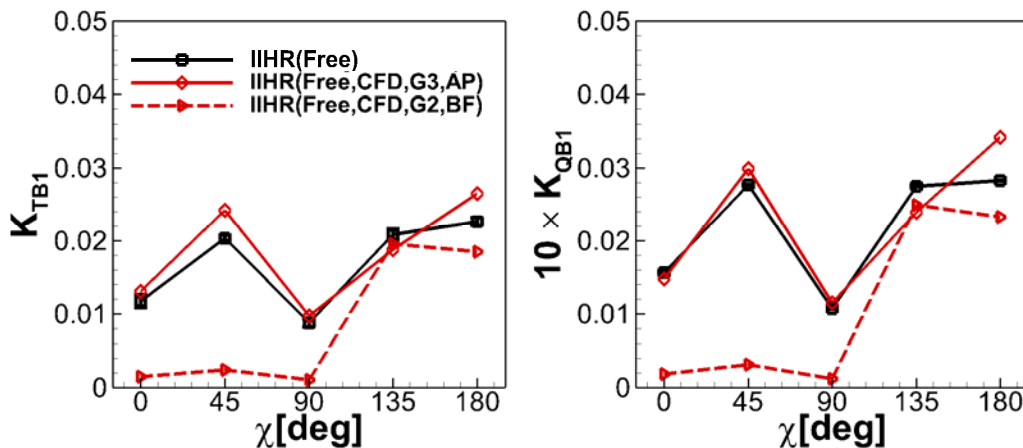


Figure 10-12. RAOs of 1st harm. amp. of thrust/torque coeff. in oblique waves

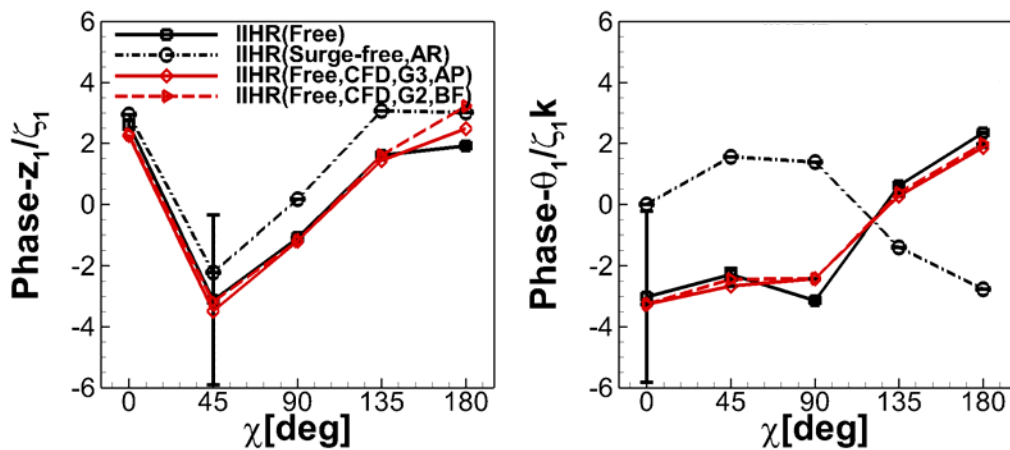


Figure 10-13. RAOs of 1st harm. phase of heave/pitch in oblique waves

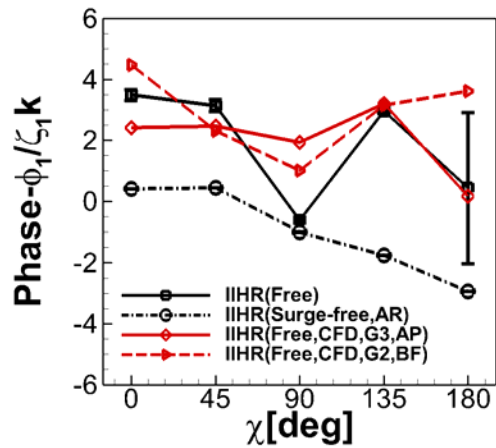


Figure 10-14. RAOs of 1st harm. phase of roll in oblique waves

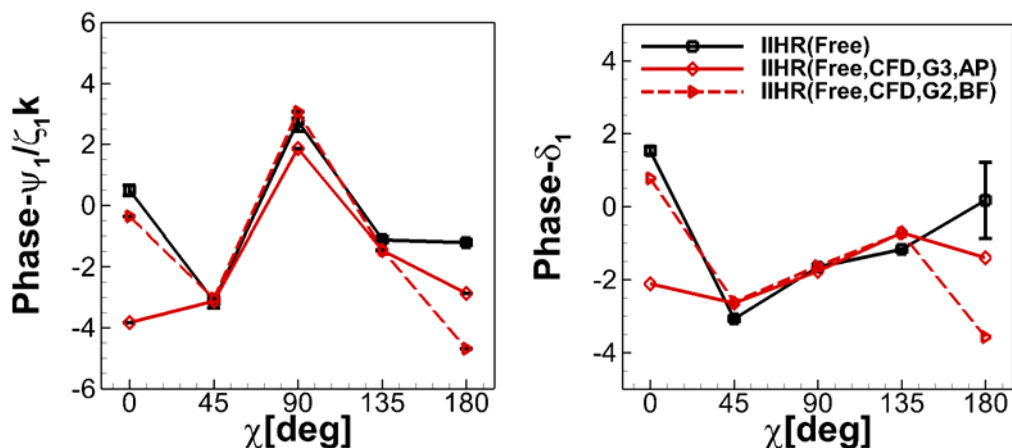


Figure 10-15. RAOs of 1st harm. phase of yaw/rudder angle in oblique waves

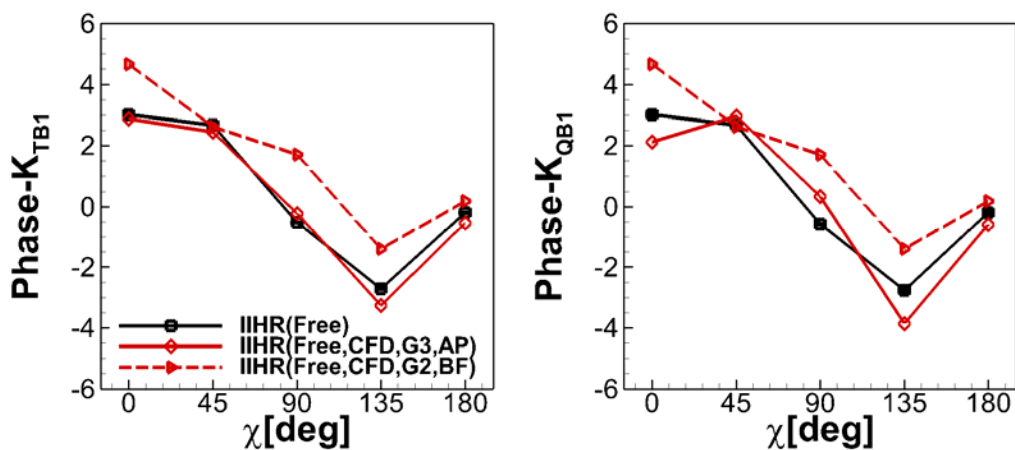


Figure 10-16. RAOs of 1st harm. phase of thrust/torque coeff. in oblique waves

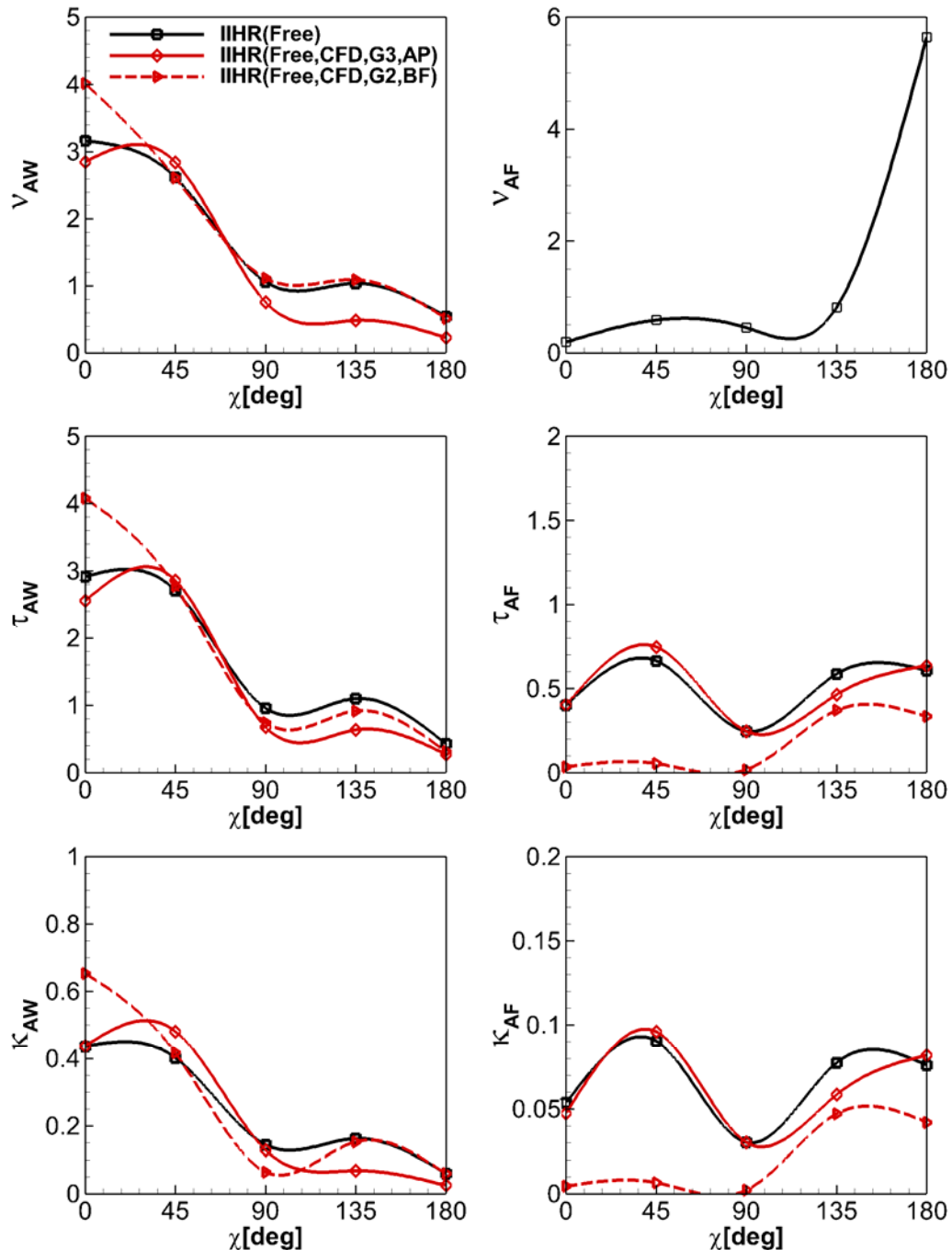


Figure 10-17. RAOs of added-powering var. in oblique waves

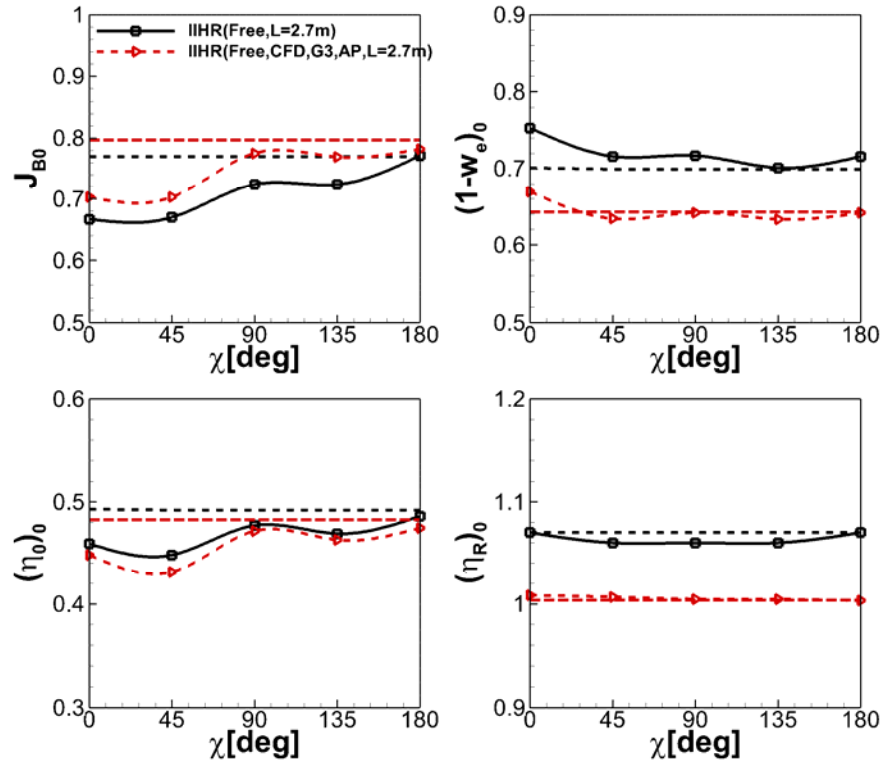


Figure 10-18. RAOs of 0th harm. amp. of SP factors in oblique waves

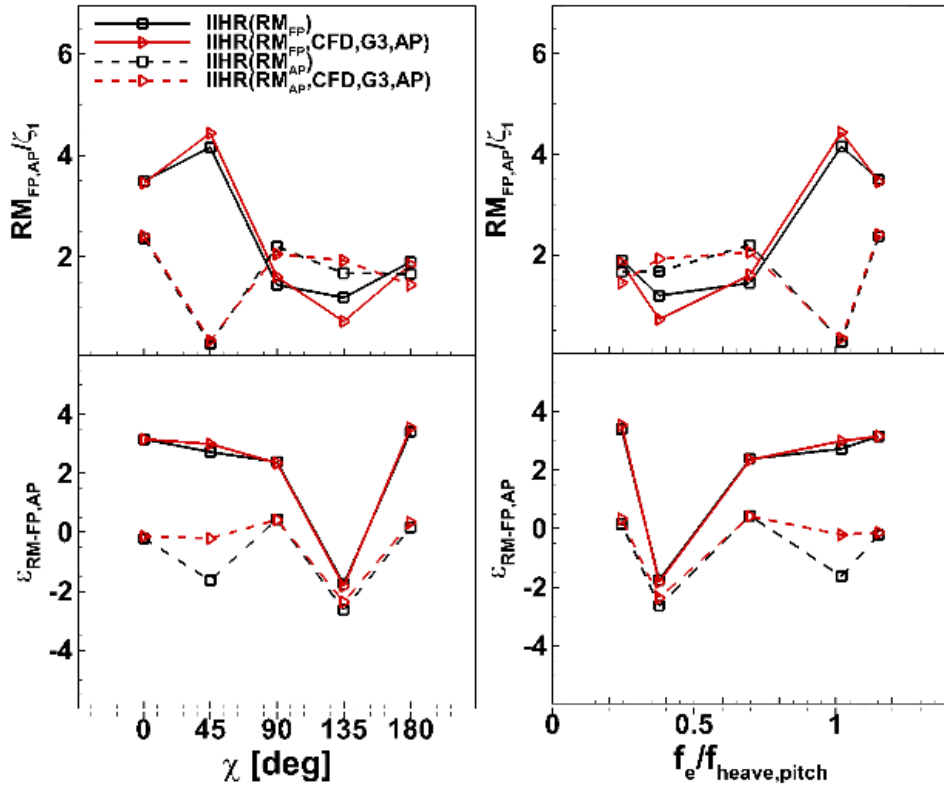


Figure 10-19. RAOs of amp. and phase of relative motions in oblique waves

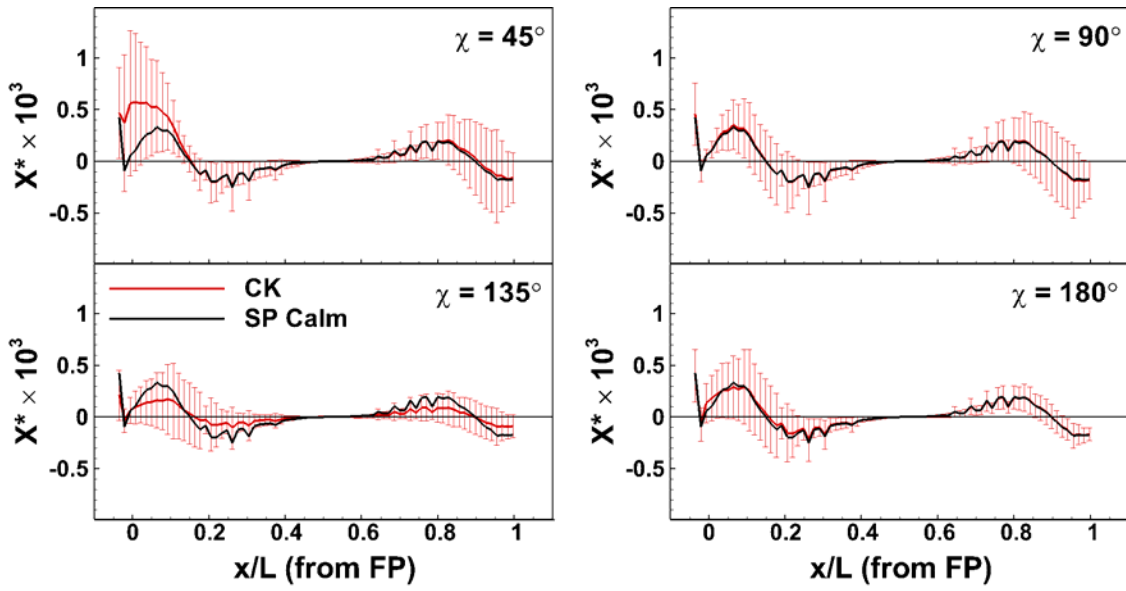


Figure 10-20. Longitudinal dist. of mean hydrodynamic x-forces on the hull in oblique waves (neg. to FP)

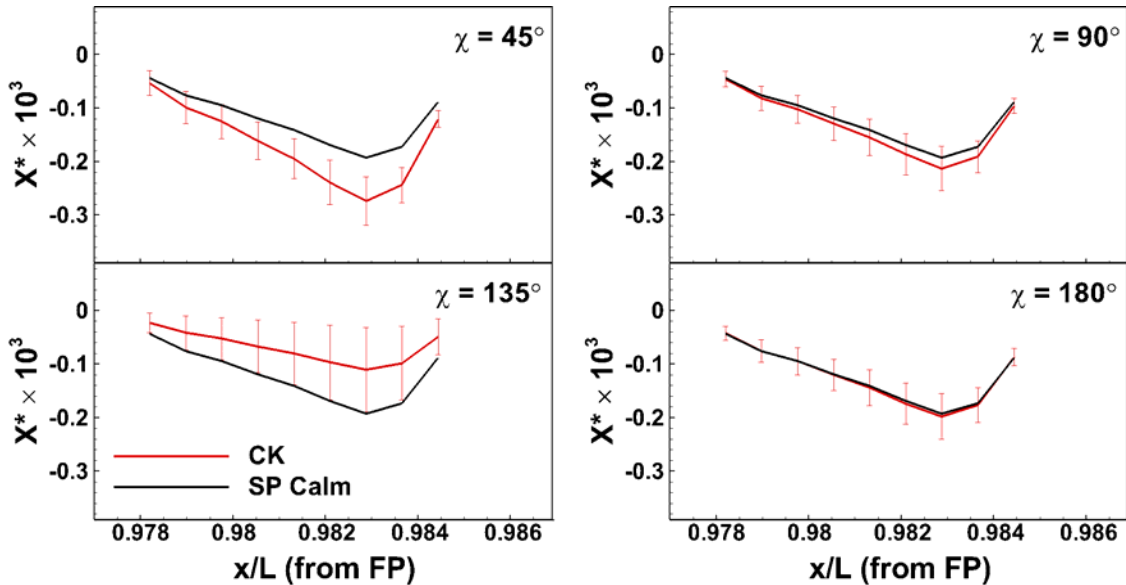


Figure 10-21. Longitudinal dist. of mean hydrodynamic x-forces on the propeller in oblique waves (neg. to FP)

## 11. CONCLUSIONS

### Case 1

For the POT, the AP model is used without the shaft, and the  $E\%D$  for the thrust, torque and propeller efficiency were consistent over advance coefficient range with reasonable errors for POT characteristics. The difference of surface pressure distribution is small between grid triplets. Still, the error between the grid triplets showed oscillations at many advance coefficient conditions. Plotting Q-criteria indicates that the difference in magnitude of the vortex core in the propeller wake significantly changes upon the current grid resolution.

### Case 2

By simulating free heave and pitch decay tests with CFD, the natural frequency of the ship could be obtained and validated with small  $E\%Empirical$  against empirical solutions. For the free roll decay, the roll radius of gyration is adjusted twice and the simulation could predict the roll damped period and the damping coefficients reasonably.

### Case 3

Grid triplets are assessed for resistance test before the calm water self-propulsion test. The grid convergence could not be achieved due to large  $U_I\%S_1$ , however, the  $E\%D$  for sinkage, trim and resistance components seemed reasonable and the scattering was small between the grid triplets. The nominal wake distribution is verified and the percentage difference of the  $1 - \omega$  between G1 and G3 is 1.3%.

### Case 4

For the calm water self-propulsion tests, the BF model is very cost effective compared to the AP model. However, the prediction accuracy for the propeller performance characteristics is

unsatisfactory due to the limit of its modelling: the propeller rotational speed of the BF model is significantly high. Meanwhile, the AP model showed good agreement for all the validation variables. By using the effective wake fraction directly calculated from the flow field of the AP model, the advance coefficient calculation of the BF model was adjusted and showed improvements for thrust and propeller revolution prediction. The study on propeller-hull-rudder interaction could be achieved by changing the grid system. The thrust that a single blade produces behind the ship was lower when the blade was located at the portside than the starboard due to the interaction with the non-axisymmetric effective wake. This propeller wake affected the angle of attack on the rudder surface and produced negative side force that made the ship go to portside. The study on the neutral rudder angle using the AP model shows that the force and moments acting on the rudder for  $\delta = 0$  and PID controlled  $\delta$  conditions show differences for the side force and the yaw moment of the rudder. The PID controlled rudder reduced the side force and the yaw moment by reducing the angle of attack of the moving rudder to almost zero. Local flow comparison with OU PIV confirms that the current AP model can predict the propeller wake (after passing the rudder) reasonably and shows the importance of refining the grid near the propeller and the rudder.

## Case 5

For the maneuvering computations, the accuracy of predicting the maneuvering case seemed more dependent on the rudder force than the propeller side force. The sensitivity test shows that the small difference of maximum rudder angle affects the zigzag  $+10^\circ/10^\circ$  significantly. Still, more verification and local flow/force measurement for the rudder seems required to bring more concrete conclusion.

## Case 6

Self-propulsion test in waves was performed to find the propeller rotational speed that puts the ship at target mean  $Fn$  and the  $E\%D$  of propeller rotational speed at each wave condition was close to  $E\%D$  from the calm water self-propulsion test. For the head wave course-keeping computation, both AP and BF models were used and the AP model showed satisfactory prediction results for most of the validation variables while the BF model often over-predicted the heave and pitch near the resonance conditions. The added thrust, added torque and added propeller revolution are in good agreement with the experiment data and the trends resembled the added-resistance curve. The axisymmetric BF model is found to be efficient way to predict the motion responses in waves. However, the lack of modelling the propeller inflow velocity induced a huge error on propeller performance characteristics as also found from the calm water self-propulsion test. The BF model also fails to predict the right phase for the thrust and torque near the resonance condition, which might have induced incorrect pressure field near the stern. The thrust identification method seemed inaccurate for calculating the effective wake fraction when the effective wake is far from the uniform flow. The RAO of the zeroth harmonic amplitude of the effective wake follows the trend of the zeroth harmonic amplitude of the thrust and the propeller rotational speed. The propeller efficiency becomes the lowest at the resonance condition. The first harmonic amplitude of the propeller efficiency gradually increases with the increment of the wavelength and reaches up to 1.8% for the longest wave. The difference of the relative motion from the forward perpendicular and the aft perpendicular becomes the largest at the resonance condition and the phase difference is 180 degree at the same condition. The location of the added-resistance found by comparing the mean longitudinal distribution of the resistance between the course-keeping in waves and the calm water self-propulsion tests, and it was mostly coming from the bow region.

Comparing the local flow with OU PIV shows that the phase difference between the OU PIV and CFD is small.

### Case 7

The self-propulsion test in the oblique waves shows similar  $E\%D$  for the propeller rotational speed. In the oblique wave course-keeping computation, the agreement of the rudder angle, yaw angle and roll angle become very close due to the larger side force that the ship experiences. The AP model shows the same prediction accuracy for all the validation variables except the zeroth harmonic amplitudes, which may require more wave periods/cycles to be accurately validated. The BF model often fails to predict heave, thrust, torque, propeller rotational speed and the thrust fluctuation. The model well predicts the added thrust, added torque and added propeller rotational speed, however, the fluctuations of thrust and torque is significantly underpredicted. The RAOs of added thrust, added torque and added propeller rotational speed resemble the added-resistance curve. The fluctuation of the thrust is the largest at the bow-quartering wave. The relative motion difference between the forward and aft perpendiculars is the largest at the bow-quartering wave condition. The propeller efficiency is the lowest at the bow-quartering wave and highest at following wave. Unlike the head wave condition, the effective wake fraction does not seem to be directly affected by the propeller rotational speed or the thrust in the oblique wave.

## 12. FUTURE WORKS

### **Propulsion modelling**

The current axisymmetric BF model can be improved by utilizing the effective wake fraction obtained from the calm water SP test. Still, due to its innate limit of being non-interactive with the flow field, the accurate effective wake fraction is unobtainable from the BF model itself, unfortunately, but still the model might be applicable for practical tests such as the parametric study once the way of predicting the wake fraction is improved.

### **Maneuvering**

The factor/mechanism that determines the ship's trajectory is unclear. Also, the accurate prediction/validation on the rudder force is required to have better conclusions.

### **Verification**

For the POT and the self-propulsion tests, even though the  $E\%D$  was small and un-scattered, a clear solution convergence has not been shown yet and the coarser grid generation will be needed in the future.

### **Maneuvering in regular wave**

Maneuvering in regular wave using CFD is not validated and requires more interests and effort.

### **Thrust fluctuation**

The study on propeller inflow velocity and the propeller thrust fluctuation is required to consider the ship speed, ship motion and the wave orbital motions.

## REFERENCES

- Carrica, P.M., Wilson, R., Noack, R., Stern, F., "Ship motions using single-phase level set with dynamic overset grids", Computers and Fluids 36, 2007, pp.1415-1433
- Carrica, P.M., Fu, H. and Stern, F., "Computations of self-propulsion free to sink and trim and of motions in head waves of the KRISO container ship (KCS) model", Applied ocean research, 33, 2011, pp.309-320
- Kim, M., Hizir, O., Turan, O. and Incecik, A., "Numerical studies on added-resistance and motions of KVLCC2 in head seas for various ship speeds", Ocean Engineering, 140, 2017, pp.466-476
- Larsson, L., Stern, F., Visonneau, M., "Numerical Ship Hydrodynamics: An Assessment of the Gothenburg 2010 Workshop", Springer, 2014.
- Otzen, J., Esquivel, P., Simonsen, C., Stern, F., "CFD and EFD Prediction of Added Powering of KCS in Regular Head Waves", 32<sup>nd</sup> Symposium on Naval Hydrodynamics, 5-10 Aug. 2018. Hamburg, Germany.
- Paterson, E., Wilson, R., Stern, F., "General-purpose Parallel Unsteady RANS Ship Hydrodynamics Code: CFDShip-IOWA", IIHR Technical Report No. 432, Nov. 2003.
- Sadat-Hosseini, H., Kim, D., Lee, S., Rhee, S., Carrica, P., Stern, F., Rhee, K., "CFD and EFD Study of Damaged Ship Stability in Regular Waves", 11th International Conference on the Stability of Ships and Ocean Vehicles, 23-28 Sep. 2012. Athene, Greece.
- Sadat-Hosseini, H., Carrica, P., Kim, H., Toda, Y., and Stern, F., "CFD V&V of added resistance of KVLCC2 with fixed and free surge conditions for short and long head waves", Ocean Engineering, Vol. 59, 2013, pp. 240-273.
- Sadat-Hosseini, H., Toxopeus, S., Kim, D., Castiglione, T., Sanada, Y., Stocker, M., Simonsen, C., Otzen, J.F., Toda, Y. and Stern, F., "Experiments and Computations for KCS Added Resistance for Variable Heading", 5th World Maritime Technology Conference, Nov. 3-7, 2015, Rhode Island, USA.
- Sanada, Y., Ito, S., Toda, Y. and Stern, F., "Added Powering Measurements of KRISO Container Ship Maneuvering in Regular Variable Heading Waves", 30th ATTC, Oct. 2017, Bethesda, MD, US.
- Sanada, Y., Kim, D., Sadat-Hosseini, H., Toda, Y., Simonsen, C., Stern, F., "Experiment and Numerical Simulation for KCS Added Powering in Regular Waves with Variable Heading", 32<sup>nd</sup> Symposium on Naval Hydrodynamics, 5-10 Aug. 2018. Hamburg, Germany.
- Seo, S., Park, S. and Koo, B., "Effect of wave periods on added resistance and motions of a ship in head sea simulations", Ocean Engineering 137, 2017, pp.309-327
- Simonsen, C., Otzen, J. and Stern, F., "EFD and CFD for KCS heaving and pitching in regular head waves", Journal of Marine Science and Technology, Vol. 18, Issue 4, Dec. 2013, pp. 435-459.

- Simonsen, C., Otzen, J.F., Nielsen, C. and Stern, F., "CFD prediction of added resistance of the KCS in regular head and oblique waves", 30th Symposium on Naval Hydrodynamics, 2-7 Nov. 2014, Hobart, Tasmania, Australia.
- Stern, F., Wilson, R., Coleman, H. and Paterson, E., "Comprehensive approach to verification and validation of CFD simulations", Journal of Fluids Engineering 123 (4), 2011, pp.793-802
- Stern, F. and Toxopeus. S., "Chapter 8 – CONCLUSIONS AND FUTURE RESEARCH", STO Technical Report NATO STO-TR-AVT-216 Task Group Evaluation of Prediction Methods for Ship Maneuvering and Control, 2018.
- Sigmund, S. and Moctar, O., "Numerical and experimental investigation of added resistance of different ship types in short and long waves", Ocean Engineering 147, 2018, pp.51-67
- Shen, Z., Carrica, P.M., Wan, D., "Ship motions of KCS in head waves with rotating propeller using overset grid method", Proceedings of the ASME 2014 33rd International Conference on Cean, Offshore and Arctic Engineering, June 8-13, 2014, San Francisco, CA, US.
- Tokyo 2015 A Workshop on CFD in Ship Hydrodynamics website <http://www.t2015.nmri.go.jp/>
- Wang, J., Zou, L. and Wan, D., "CFD Simulations of Free Running Ship Under Course Keeping Control", Ocean Engineering 141, 2017, pp.450-464
- Wu, P., Okawa, H., Kim, H., Akamatsu, K., Sadat-Hosseini, H., Stern, F. and Toda, Y., "Added Resistance and Nominal Wake in Waves of KVLCC2 Model Ship in Ballast Condition", 30th Symposium on Naval Hydrodynamics, 2-7 Nov. 2014. Hobart, Tasmania, Australia.
- Wu, P., Sadat-Hosseini, H., Stern, F. and Toda, Y., "Nominal wake fluctuation due to waves", 日本船舶海洋工学会論文集, 24, 2016, pp.13-19
- Wu, P., Hossain, M., Kawakami, N., Tamaki, K., Kyaw, H., Matsumoto, A., Toda, T., "EFD and CFD Study of Forces, Ship Motions and Flow Field for KRISO Container Ship Model in Waves", 32<sup>nd</sup> Symposium on Naval Hydrodynamics, 5-10 Aug. 2018. Hamburg, Germany.
- Xing, T. and Stern, F., "Factors of safety for Richardson extrapolation", Journal of Fluids Engineering, Vol. 132, No.6, 2010.